


Summer 2010

# Simulation Studies of Pulsed Voltage Effects on Cells

Jiahui Song  
*Old Dominion University*

Follow this and additional works at: [https://digitalcommons.odu.edu/ece\\_etds](https://digitalcommons.odu.edu/ece_etds)

 Part of the [Bioelectrical and Neuroengineering Commons](#), and the [Electrical and Computer Engineering Commons](#)

---

## Recommended Citation

Song, Jiahui. "Simulation Studies of Pulsed Voltage Effects on Cells" (2010). Doctor of Philosophy (PhD), dissertation, Electrical/Computer Engineering, Old Dominion University, DOI: 10.25777/x81z-qe88  
[https://digitalcommons.odu.edu/ece\\_etds/130](https://digitalcommons.odu.edu/ece_etds/130)

This Dissertation is brought to you for free and open access by the Electrical & Computer Engineering at ODU Digital Commons. It has been accepted for inclusion in Electrical & Computer Engineering Theses & Dissertations by an authorized administrator of ODU Digital Commons. For more information, please contact [digitalcommons@odu.edu](mailto:digitalcommons@odu.edu).

# Simulation Studies of Pulsed Voltage Effects on Cells

by

Jiahui Song

B. S. Southeast University, Nanjing, China  
M. S. Southeast University, Nanjing, China

A Dissertation Submitted to the Faculty of  
Old Dominion University in Partial Fulfillment  
of the Requirement for the Degree of

DOCTOR OF PHILOSOPHY  
ELECTRICAL AND COMPUTER ENGINEERING  
OLD DOMINION UNIVERSITY  
August 2010

Approved by:

---

Ravindra P. Joshi (Director)

---

Linda L. Vahala (Member)

Jürgen H. Kolb (Member)

---

Đức T. Nguyen (Member)

## ABSTRACT

### SIMULATION STUDIES OF PULSED VOLTAGE EFFECTS ON CELLS

Jiahui Song  
Old Dominion University, 2010  
Director: Dr. Ravindra P. Joshi

This dissertation research focuses on the new field of pulsed electric field interactions with biological cells. In particular, “Intracellular Electromanipulation” which has important biomedical applications, is probed. Among the various aspects studied, nanosecond, high-intensity pulse induced electroporation is one phenomena. It is simulated based on a coupled scheme involving the current continuity and Smoluchowski equations. A dynamic pore model can be achieved by including a dependence on the pore population density and a variable membrane tension. These changes make the pore formation energy  $E(r)$  self-adjusting and dynamic in response to pore formation. Additionally, molecular dynamics (MD) simulations are also discussed as a more accurate, though computationally intensive, alternative.

Besides inducing pores in cells, external voltages could also be used, in principle, to modulate action potential generation in nerves. The electric-field induced poration could block action potential propagation. This aspect has been studied by modifying the traditional cable model for nerves, by accounting for the increased membrane conductance and the altered membrane capacitance. This conduction block in nerves due to an electroporation related local short-circuit would be similar in concept to stopping the propagation of an air-pressure wave down a “leaky” pipe.

This study also focuses on threshold process in cellular apoptosis induced by nanosecond, high-intensity electric pulses. In particular, the pulse number dependent cell survival trends are quantified based on a biophysical model of the cellular apoptotic processes. Time-dependent evolution of the caspase concentrations and the various molecular species are simulated. The numerical evaluations provide qualitative predictions of pulse number cell survival, the relative assessment of extrinsic and intrinsic pathways, and rough predictions of the time duration over which irreversible activation at the molecular level could be initiated by the electric pulses. Time dependent kinetics of the caspases as well as the various molecular species within the apoptotic pathway, were simulated using the rate equation model originally proposed by Bagci et al.

Finally, an asymmetric electroporation model is presented. Electric pulsing pore energy and mechanical pore energy are studied. This has relevance to the flow of ions in and out of cells.

## ACKNOWLEDGMENTS

I would like to thank my advisor, Dr. R. P. Joshi, for his valuable academic guidance, encouragement, and patience throughout the course of this study. I could not have completed this project without his abundant help in every aspect. He set a great model for me in my future work. I would also like to thank my research committee members, Dr. Linda L. Vahala, Dr. Juergen F. Kolb and Dr. Duc T. Nguyen for their review and valuable comments.

Great thanks to the researchers at the Center for Bioelectronics for their great experimental work and inspiring discussions, which made it possible to finish this dissertation. I would also like to acknowledge the Electrical and Computer Engineering Department for their support all these years. I really enjoyed my time studying in this department.

Special thanks goes to my parents for their courage and support to pull me through difficulties. Special thanks also should go to my friends Dr. Qin Hu, Dr. Ashutosh Mishra, Dr. Viswanadham Sridhara, Dr. Jun Qian, and Dr. Guogang Zhao.

## TABLE OF CONTENTS

LIST OF FIGURES .....	vi
LIST OF TABLES.....	viii
<b>CHAPTER I INTRODUCTION</b>	<b>Page</b>
1.1 Overview .....	1
1.2 Scope of This Research .....	2
<b>CHAPTER II LITERATURE REVIEW AND BACKGROUND</b>	
2.1 Introduction of Nanosecond, High-Intensity Electric Pulse Based Bioelectric Effects.....	5
2.2 Some Experimental Results Reported in the Literature .....	15
2.3 Simulation Schemes for Predicting Bioelectric Effects .....	18
<b>CHAPTER III MODELING AND SIMULATION DETAILS</b>	
3.1 An Improved Pore Area Dependent Energy Model .....	26
3.2 High-Intensity Electric Pulse Induced Action Potential Block in Whole-Animal Nerves.....	30
3.3 Threshold Porecess in Cellular Apoptosis Induced by Nanosecond, High-Intensity Electric Pulses .....	36
3.4 An Asymmetric Electroporation Model .....	47
<b>CHAPTER IV SIMULATION RESULTS AND DISCUSSION</b>	
4.1 Simulation Results and Discussion of Pore Area Dependent Energy Model....	52
4.2 Molecular Dynamics Simulation Results Including Temperature Effects .....	58
4.3 Simulation Results of High-Intensity Electric Pulse Induced Action Potential Block.....	61
4.4 Simulation Results of Pulsed-Number Dependent Cellular Apoptosis and the Threshold Effect.....	63
4.5 Simulation Results of the Asymmetric Electroporation Model.....	74
<b>CHAPTER V CONCLUSIONS AND FUTURE RESEARCH</b>	
5.1 Research Summary .....	80
5.2 Future Work.....	82
<b>REFERENCES .....</b>	<b>85</b>

## LIST OF FIGURES

Figure	Page
1. MD sanpshots of the electroporation process in a DPPC membrane .....	7
2. Jurkat and HL-60 cells exposed to pulsed fields .....	15
3. Data showing caspase activity in Jurkat cells.....	16
4. Images of HL-60 cells before and after applying a 10 ns, 60 kV/cm pulse. ....	17
5. A Jurkat cell stained with Bodipy Brefeldin A 558/568 before and after a pulse.....	18
6. The pore formation energy $E(r)$ of hydrophilic pores.. ....	24
7. Schematic of one quarter of the model used to represent a cell .....	28
8. Schematic of the cable model used to represent a nerve fiber.....	33
9. Sketch of pores created on the nerve membrane by the external voltage.....	34
10. Mitochondria-dependent apoptotic pathways.....	43
11. Structured information model of CD95-induced apoptosis .....	46
12. Dielectric body $M$ in a dielectric/conductive fluid $\Omega$ .....	48
13. A symmetric toroidal pore. ....	48
14. Toroidal geometry of pore model inside surface.....	49
15. An asymmetric pore model geometry .....	50
16. A planar lipid bilayer with a pore in the center. ....	50
17. Simulation results of the pore distribution function $n(r)$ . ....	53
18. Simulation results of the fraction of total pore area to membrane surface.....	54
19. Simulation results in reponse to an external pulse .....	56
20. MD results showing nano-pore formation at membrane. ....	59
21. MD results showing nano-pore formation at membrane at different temperatures.....	60
22. Required electric field versus pulse width to generate minimum $G_{sh}$ .....	63

23. Single cell simulation results for the time-dependent C3 concentration .....	65
24. Time dependent changes in C3 concentration following a low level injection of C8 in a single cell .....	66
25. Single cell simulation results for the temporal evolution of the C8 and blocked DISC state concentrations .....	67
26. Predicted cell survival versus pulse number with 1000 cells .....	68
27. Cell survival versus pulse number predicted for two different values of <i>cytochrome c</i> release.....	70
28. C3 versus time from single cell simulations under various conditions of C8 activation and <i>cytochrome c</i> release. ....	71
29. Electrostatic pore energy versus pore radius for different shapes of electropores. ....	75
30. Mechanical pore energy versus pore radius. ....	76
31. Total pore energy versus pore radius.....	77
32. Total pore energy surface .....	78
33. Simulation results for pore closure time. ....	79



**LIST OF TABLES**

Table	Page
1. Parameters used for the theoretical model.....	23
2. Parameters used in our simulations. ....	44
3. Maximum conductance $G_{sh}$ computed at 100 mV.....	63

# CHAPTER I

## INTRODUCTION

### 1.1 Overview

In order to predict or explain a complicated biological process, it is important to first construct mathematical models that can be used to yield analytical solutions. Through numerical simulation, mathematical model results can be used to test scenarios that might not be easily attained in a laboratory experiment, or to predict parameters or phenomena, and also to explain experimental data. Also, simulation models are usually not as costly as experimental work, and they take much less time. Hence, constructing mathematical models is a very useful tool for predicting, testing and quantitative understanding.

Ultra-short, high-intensive pulse electroporation has been a very recent development in bioelectrics. Advantages of using short electric pulses include: (i) negligible thermal heating; (ii) large electric fields and peak powers, with a lower energy input; (iii) the possibility to select the desired time scales through pulse width manipulation; and (iv) the ability to penetrate the outer (plasma) membrane and create large trans-membrane potentials across sub-cellular organelles.

The application of high-intensity, pulsed electric fields has led to the following significant observations:

- (i) Multiple electric shocks have been observed to do more irreversible damage than a single pulse.
- (ii) Irreversible cell damage occurs at the intracellular organelles [1].

(iii) Calcium release has been observed from the intracellular endoplasmic reticulum in response to external voltage pulses [1, 2].

(iv) Cell apoptosis has been observed [1, 3] for cells subjected to short electrical pulses.

(v) Apoptotic behavior has been observed to depend on the pulse duration.

(vi) The electroporation driven by ultra-short, high-intensive pulses can also be used in the temporary blockage of action potential propagation in whole-animal nerves.

(vii) Such pulsing can be a method to kill unhealthy (i.e., tumor) cells [4, 5]. This would have great benefits in the treatment of diseases such as cancer.

(viii) The electrical pulsing can also open pores in cell membranes. This can lead to electrically modulated changes in transport through membranes and into cells. For example, drugs or genes could be forced into targeted cells by first opening them through electrical pulsing.

## 1.2 Scope of This Research

Application of an electric field can cause poration at cell membranes. This includes the outer plasma membrane, as well as the membranes of intracellular organelles. In order to analyze and predict such electroporation effects, it becomes necessary to first evaluate the electric fields and the transmembrane voltages. This information can then be used to assess changes in the pore formation energy that finally yields the pore distributions and their radii based on the Smolchowski equation. The dynamic pore model can be achieved by including a dynamic aspect and a dependence on the pore population density into pore formation energy equation. These changes make the pore formation energy  $E(r)$  self-adjusting in response to pore formation without causing uncontrolled growth and expansion.

Besides inducing pores in cells, external voltages could also be used in principle to modulate action potential generation in nerves. Numerical evaluations of membrane pores and their dynamic evolution in response to an applied high-intensity, short-duration (nanosecond) electric pulse were carried out to obtain values of an additional time-dependent membrane conductance  $G_{sh}$  which accounts for the poration induced by the high-intensity short-duration electric pulsing. The role of the electrical pulsing is to let the neural fiber inhibit the propagation of an electrical signal. This could have an application in electrically controlled “pain management.”

Apoptosis plays a central role in the development of all multicellular organisms and in maintaining their homeostatic balance [6-8]. There are multiple apoptotic pathways; among them are the so-called extrinsic pathway instigated at the cellular plasma membrane and the intrinsic, mitochondrial-initiated process. The role and extent of electric field modifications of the apoptotic pathways are unclear. A simple model-based rate equation treatment of the various cellular bio-chemical processes has been used to predict the pulse number dependent cell survival trends. Possible consequences of the applied field are conjectured and discussed in this dissertation research.

Finally, almost all previous analysis of electric field effects on cells have been based on the concept of cylindrical pores. However, it is conceivable that the pore shape is not cylindrical, that they can dynamically change over time, or perhaps even display some shape asymmetry. An asymmetric pore shape would be indicative of differences in current flow directionality and asymmetric current-voltage (I-V) relationships. Pore formation energy and both electrical and mechanical contributions to the pore energy that

governs poration are discussed in this work. This forms the basis of a model-based argument for the existence of asymmetric electropores.

Chapter 2 of this dissertation provides a literature review of the research on electroporation and reported contributions in the general field of bioelectrics. Descriptions of an improved pore area dependent energy model and some molecular dynamics (MD) simulation work are given in Chapter 3. High-intensity electric pulse induced action potential block in whole-animal nerves based on a model, and the threshold process in cellular apoptosis induced by nanosecond, high-intensity electric pulses are described in detail in this chapter. Discussions and the mathematical details of possible asymmetric electroporation are also included. Details of the various simulation results obtained and related problem discussions are given and explained in Chapter 4. A summary and conclusion of the present research is given in Chapter 5. This last chapter also includes comments on possible future work.

## CHAPTER II

### LITERATURE REVIEW AND BACKGROUND

#### 2.1 Introduction of Nanosecond, High-Intensity Electric Pulse Based Bioelectric Effects

Endogenous electric fields (EFs) have been used in biology for hundreds of years and have been shown to have significant effects on many facets of cellular biology. Some of these effects are generated by low EFs and DC currents. For example, low EFs have been used to affect development [11], promote regeneration [12], arrest cell proliferation, generate action potentials [13], as well as promote cell shape changes, motility, locomotion and cell migration [14], which are all important for embryonic development and wound healing. These observations re-inforce the idea that EFs are generated *in vivo* and cells respond to them as a means of carrying out functions important for life. This is also a decidedly crucial factor for the healing of wounds as fibroblasts follow EFs to close a wound.

The use of intense EFs has provided biological advantages for fusing cells to produce monoclonal antibodies [15], delivering drugs and genes to cells and tissues for analysis of gene expression, for therapeutic application in cancer treatment [16-18], and for eliminating cancer cells as a means of cancer therapy [19-20, 31, 114]. Another use of electric fields is in porating cellular membranes – a process commonly referred to as electroporation – for purposes of introducing molecules and drugs into cells. Traditionally, electric pulse durations in the microsecond range and field intensities of about 1-10 kV/cm were used for electroporation [21]. A practical application was the injection of drugs (i.e., electrochemotherapy) or to facilitate gene transfer through the

outer plasma membranes [22-23]. The use of electric pulses with very high fields (~100kV/cm or higher) and pulse durations in the nanosecond range [24-25] in electroporation has been a recent development. As a non-thermal tool (heating less than 1°C [39, 45]), such high-intensity, nanosecond, pulsed electric fields (nsPEFs) have been shown to be capable of affecting both the plasma membrane and reaching the interior cellular organelles [26, 61, 95]. Biological applications include non-thermal destruction of micro-organisms [27-28], killing of tumor cells [29], temporary blockage of action potential propagation in nerves [43, 50], and disruption of voltage-gated channels [30]. The nsPEFs can create high-density nanometer-sized pores in cell plasma membranes as well as membranes covering the various inner-organelles [51-53] if the pulses are judiciously selected.

### **2.1.1 Electroporation of Cell Membranes**

Membranes are largely composed of amphiphilic lipids, which normally assemble into bilayer structures. This highly insulating configuration produces a large energy barrier to transmembrane ionic transport. Thus, the membranes of living cells have the capacity for selective absorption. However, the integrity of membranes can be destroyed when a strong external electric field is present and aqueous pores start to be formed in the membrane (Figure 1). These will lead to an increase in transmembrane conductivity and diffusive permeability. These effects will also alter the electrical potential across the membrane. This process is collectively called electroporation. These electrical induced pores are commonly called “electropores.” Their presence allows molecules, ions, and water to pass from one side of the membrane to the other without limiting selectivity. After the external electrical pulse is ceased, the pores close automatically in minutes or

may never close leading to irreversibility and potential cell death. These effects are critically dependent on the duration and magnitude of the applied pulse. The reversible process of electroporation can be used to inject large molecules, such as DNA, or some suitable drugs, which would otherwise not go into the cell due to the selectivity of the membrane and the small size of the embedded ionic channels. The irreversible process can be used to destroy cells such as tumor cells in a localized manner.

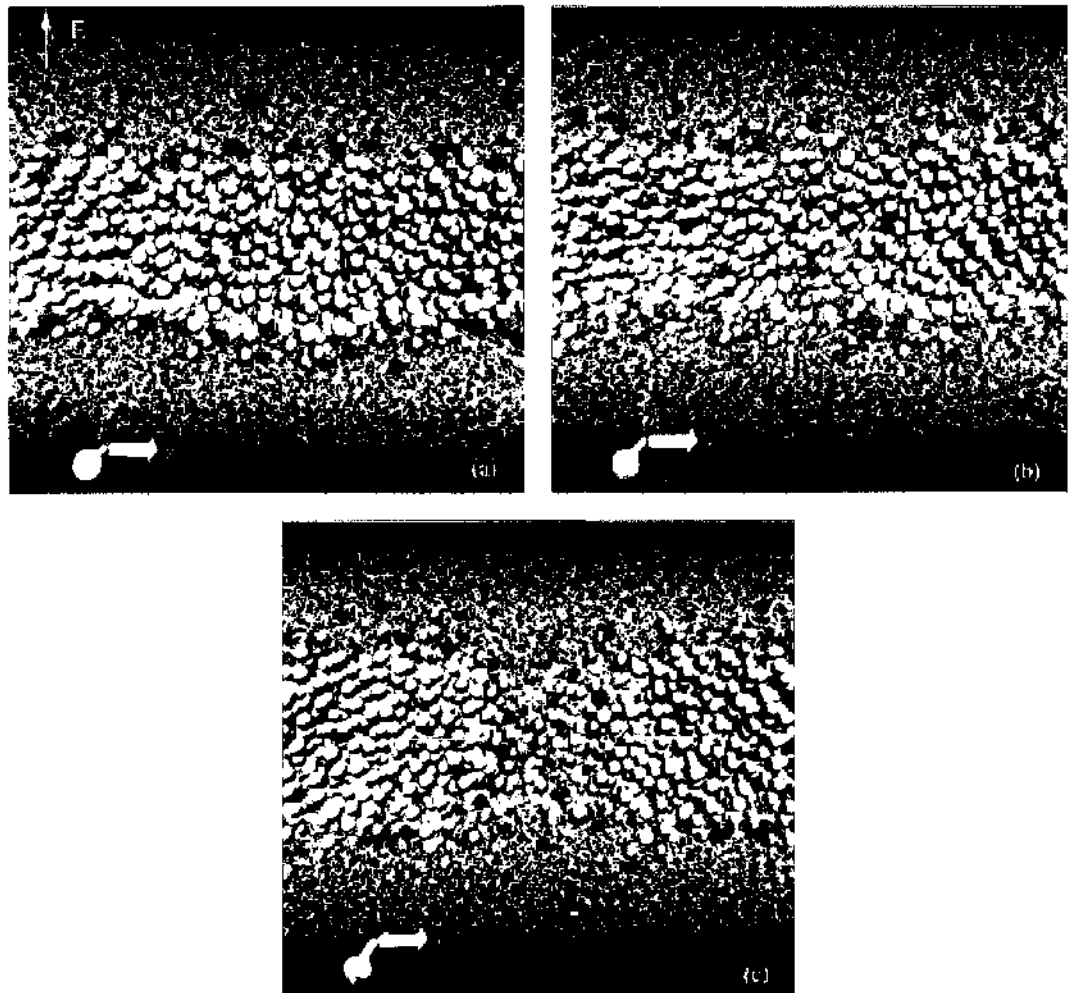


**Figure 1.** MD snapshots of the electroporation process in a DPPC membrane when applied E field is 0.01 V/nm with a 10 ns duration, a 1.5 ns rise time, and 1.5 ns fall time. (a) Initial configuration at  $t = 0$  ns; (b) structural rearrangement begins at the membrane bottom at about  $t = 4.8$  ns; (c) a pore predicted to form at  $t = 5.3$  ns. The positively polarized choline groups are colored blue, and the negatively polarized phosphatidyl group brown, the glycerol green, the tails cyan. The oxygens in water molecules are red and hydrogens are white [67].



### 2.1.2 Application of Electric Fields to Drug Delivery and Gene Transfer

*Ex vivo* applications of electroporation have involved blood cells, treated outside the body, with reintroduction to provide therapy [9]. White cells are larger than red blood cells and can be electroporated to load drugs into white cells in the presence of red cells [9]. Platelet cells can also be loaded [10]. Manipulation of the oxygen binding capability of red cells [31] and electroinsertion of appropriate proteins into the red cell membrane [32] are both under sufficiently electroporation conditions.

*In vivo* applications include the local delivery of potent but relatively membrane impermeable anticancer drugs into solid tumors [33-34]. Electrochemotherapy (ECT) has now reached clinical trials [35-36]. Experiments show that orders of magnitude more bleomycin is delivered into cell interiors than by passive permeation [37].

Gene therapy is of great interest by using a virus to introduce foreign DNA into cells [37]. A physical method such as local tissue electroporation is of interest because there are several problems for viral methods [80- 81, 92-94, 103-104]. DNA is first introduced into a tissue, and then electrical pulses are applied to electroporate the cells of a tissue within a treatment volume [37].

Both ECT and localized gene therapy are examples of drug delivery, in which a therapeutic agent is introduced into desired regions or cells within the human body [37]. Drug delivery is a significant research area [38], especially minimally invasive drug delivery such as transdermal drug delivery [37]. Because controlled delivery through the skin can be located outside the body and is unobtrusive, the technology is potentially valuable [37].

### **2.1.3 Nanosecond, High-Intensity Electric Pulses Induced Cellular Apoptosis**

More recently it has been shown that nanosecond, high-intensity electric pulses can also cause shrinkage and even complete elimination of melanoma tumors [40]. Applications include bacterial decontamination and tumor treatment.

A general goal of electromanipulation is to evoke controlled cellular responses from the applied electric pulses. While reversible and temporary changes are often desired (e.g., for drug or gene delivery), irreversible effects or apoptotic cell killing can also be important objectives in certain other situations. The latter include bio-decontamination, targeted elimination of tumor cells, or growth factor activation. However, for precise control in achieving the desired outcomes, one needs to better understand the boundaries of these two regimes, the critical parameters that guide the system towards one outcome or the other, and the underlying biophysical mechanisms and processes.

A threshold effect is always observed, with cell survival being the eventual outcome if either the field intensities or number of pulses (or both) are not sufficiently high [39, 41]. One of the most complete cell viability studies under nanosecond electric pulsing was reported by Pakhomov et al. [39, 42]. In one study [42], the viability of human lymphoma cells (U937 and Jurkat cells) to multiple 10 ns pulses was studied using Trypan Blue uptake as the indicator for cell death in over 200 samples. Trypan Blue was added 24 hours after pulsing to ensure that cell recovery, which occurs on a much faster timescale, was not an issue. Results obtained at various electric field intensities versus the number of pulses revealed an initial horizontal plateau, followed by a near-exponential fall off beyond a characteristic threshold. Furthermore, the “shoulder” for each cell type (Jurkat and U937) had a different value. In the other reported study [39],

the 24-hour U937 cell survival was tracked in response to repetitive 50kV/cm and 150 kV/cm pulses of 10-ns duration at 2 and 1 Hertz, respectively. A pulse number threshold was observed with almost no effect on cell killing until about 1000 pulses for the 50 kV/cm case.

#### **2.1.4 Nerve Stimulation Through Electrical Pulsing**

Action Potential (AP) block in nerves has been explored for over a decade now. It is well known that the application of electrical voltages, including DC and high frequency AC can reversibly block the conduction of action potentials across nerves. Though other methods of achieving nerve conduction blockage such as pressure application, temperature lowering, and chemical and pharmacological means exist, none can be as fast acting, localized, and yet reversible as electrical stimulation [43-46]. Cessation of biological electrical signaling pathways can have a variety of applications in neurophysiology, clinical research, neuromuscular simulation therapy, muscular and sensory incapacitation. For example, pudendal nerve conduction block during micturition can reduce urethral pressure or help relieve chronic pain from a site of peripheral nerve injury [43, 47-48]. The blocking ability is progressive from larger to smaller nerve fibers, and has been used in muscle activation and fatigue reduction. The concept of arresting AP propagation on command through external electrical stimulation could open up the possibility of temporary incapacitation with applications to crowd control.

The generation and propagation of an action potential in a nerve fiber is triggered by perturbations in trans-membrane potential that activate ionic flows through voltage-gated sodium and potassium channels. As first proposed by Hodgkin-Huxley [49] and Huxley-Frankenhaeuser [36], a trans-membrane potential greater than a threshold initiates

depolarization. By disrupting the trans-membrane potentials at localized nerve points downstream (relative to the initial point of stimulation), it becomes possible to arrest action potential propagation. A simple-minded approach is through the application of an external dc bias near a nerve. For a propagation action potential (initiated, for example, by a depolarizing voltage), the application of a positive bias on the outer region of the nerve would prevent the local potential from reaching the requisite negative value [50]. This would effectively impede AP propagation and hence block nerve conduction. However, the prolonged DC bias can itself inject localized currents and charge the axonal membranes, thereby launching its own AP. Also, sharp rise times for the DC biasing would lead to large capacitive charging and have the same undesirable effect of self-launching an AP. Hence, the rise and fall times of any applied DC bias need to be sufficiently large. Furthermore, long durations or repetitive DC biasing can potentially cause tissue damage due to internal heating. For effective suppression of this deleterious effect, the net energy needs to be sufficiently small. Finally, for DC pulses it is practically difficult to achieve reliable conduction blockages for all possible propagating APs since the timing and sequence of propagating action potentials are not known a priori.

Though the application of high frequency blocking signals alleviates some of the problems with DC biasing, including reducing heat generation and making it more difficult to self-launch action potentials, potential difficulties remain. The frequency of operation now begins to play an important role in the blocking effectiveness. A frequency bandwidth for AP extinction exists, and stimulation that is either too fast or too slow cannot provide a conduction block. A very low frequency bias signal will not have sufficient time to disrupt an approaching action potential, while a very fast oscillatory

signal will effectively present a net zero average perturbation [50, 114]. In addition, continuous AC signals can contribute to heating.

High intensity, short-duration electric pulses (HISDEPs) block nerve conduction by modulating the membrane conductivity through the electroporation process. Formation of a high pore density would increase the local membrane conductivity and effectively “short-out” the trans-membrane potential of a nerve in the vicinity of the pulsing electrode. The net effect would be a disruption in the requisite trans-membrane potential shift required to sustain AP propagation [18-20, 50]. The use of HISDEPs for conduction blockage appears to offer the following advantages [48].

(a) Negligible heating, due to the low energy content of each pulse. This would minimize any possible tissue damage and allow repetitive pulsing to achieve the desired effects for selected durations.

(b) Reversibility of such HISDEPs effects due to the resealing of membrane nano-pores created by the external voltage. Hence, a permanent effect would be avoided.

(c) Fast turn-on (~ tens of nanoseconds), and provision of spatially tailoring the effect.

(d) Unlike the DC or AC excitation, it would be more difficult to “self-launch” action potentials which require depolarization over micro-second time scales or longer. The porated regions of the membrane would effectively clamp the local trans-membrane potential to near-zero values. Also, the nanosecond pulse termination would produce a negative voltage change with time and, hence, a strong negative displacement current. This would cause the membrane potentials to fall sharply back to their resting potentials well before the microsecond time scales that are typically required for launching action potentials [50].

### 2.1.5 Electrical Stimulation Based Chemical Release and Cell Signaling

Calcium release has been observed from the endoplasmic reticulum (ER) in response to external voltage pulses [2, 54, 95], with many of the experiments being conducted in the absence of extracellular calcium. External voltage triggering of  $\text{Ca}^{2+}$  release could be a vital element in artificially inducing cell signaling. Since intracellular  $\text{Ca}^{2+}$  release leads to some uptake by the mitochondria, such voltage-triggered  $\text{Ca}^{2+}$  release could potentially have secondary effects on the mitochondria. Alterations in the mitochondrial membrane potential due to cationic entry is a possibility. Such transmembrane voltage changes are known to trigger opening of the permeability transition pore [55-56], leading to *cytochrome c* release and cellular apoptosis.

Calcium modulation is an important signaling process and could even contribute to cell apoptosis through ionic induced perturbations in transmembrane potential at the mitochondria. The present numerical study has been reported [94] to probe the time- and spatially dependent modulation of calcium dynamics through the application of external voltages. A two-step coupled model was used in that analysis. First, the distributed solution for cellular electric fields in response to an externally applied voltage was obtained. This was based on a distributed electrical circuit model coupled with the Smoluchowski equation [38] for membrane dynamics. This output was then combined with the continuum Li-Rinzel model [57] for calcium flow. The results were shown to be in agreement with the observed calcium dynamics in the absence of extracellular calcium. A modest increase (roughly doubling) of the cellular calcium was predicted that agreed with several reports [51]. No oscillations were predicted, again in keeping with experimental reports. A quantitative explanation for the lack of such oscillatory behavior,

based on the density dependent calcium fluxes, was provided. A net recovery period of about 5 minutes following an external  $E$  pulse was also obtained. This agreed with experimental data and sets the limit for a possible memory effect within cells. It is possible that at much higher electric fields (e.g., 150 kV/cm and higher as routinely achieved at the Center for Bioelectrics, ODU), the response might become more interesting. The mitochondria and PM would probably get porated, and high transmembrane fields might induce alterations in the IP3 channel functionality. The latter could be analyzed through coupled molecular-dynamics-generalized Born techniques and efforts in this regard. Other interesting situations include the application of periodic, repetitive external voltage wave forms with variable frequency and duty cycles for triggering constructive interference with the natural oscillatory cellular calcium phenomena.

## 2.2 Some Experimental Results Reported in the Literature

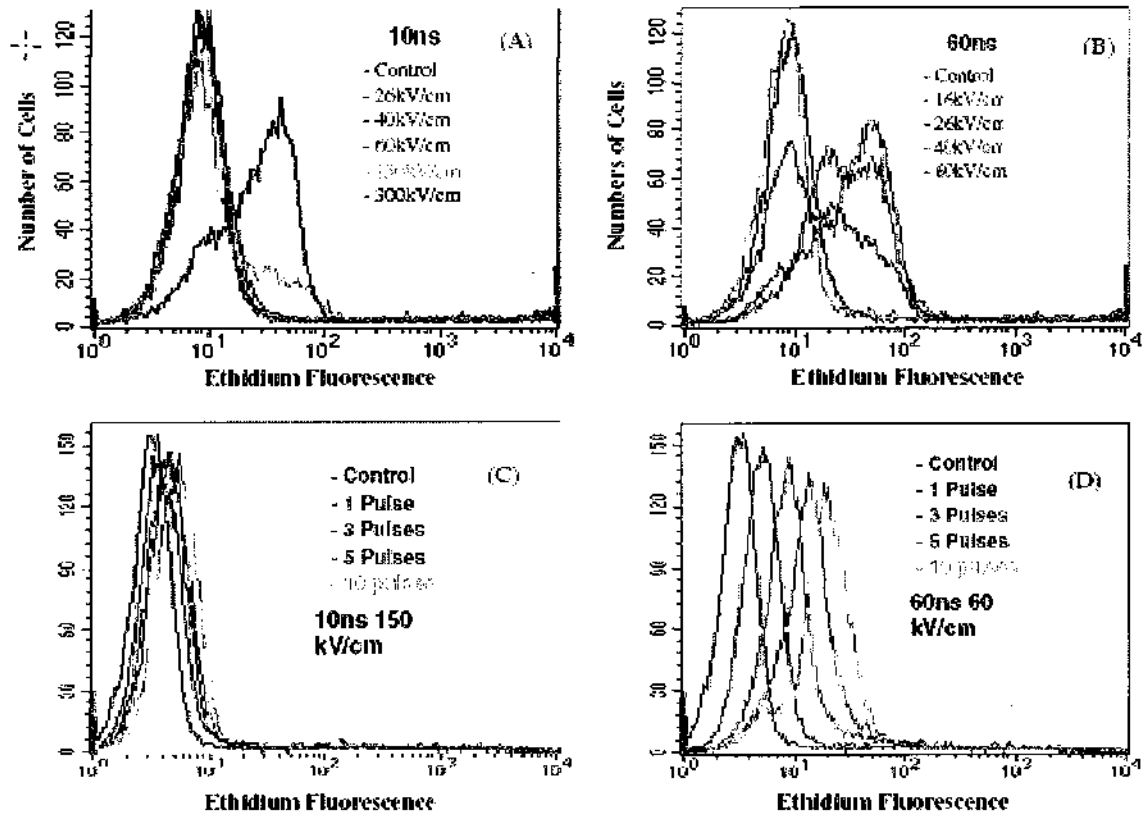


Figure 2. As the pulse number durations and/or the electric field intensities decrease, effects on the plasma membrane (PM) decrease. Jurkat cells (panels A and B) and HJ-60 cells (panels C and D) were maintained in log phase growth, washed and re-suspended in Hanks Balanced Salt Solution in the absence of calcium and magnesium. Cells ( $130 \mu\text{l}$ ,  $1 \times 10^6$  cells  $\text{ml}^{-1}$ ) were exposed in electroporation cuvettes to pulsed electric field conditions as indicated in the presence of ethidium homodimer-1 as a marker for plasma membrane integrity. Immediately after treatment with pulsed electric fields (5-10 min) 15000 cells were analyzed by flow cytometry and Cell Quest software [61].

Recently, concrete experimental data were presented showing that as the pulse duration decreases effects on the plasma membrane would decrease [61]. For example, Figure 2 shows Jurkat or HL-60 cells that were exposed to pulsed fields with durations of 10 or 60 ns and the number and amplitude of the pulses were varied [61]. The cells were treated with the pulses in the presence of ethidium homodimer-1, a fluorescent, and then analyzed by flow cytometry [61]. The level of fluorescence is a direct indicator of levels of effects on plasma membrane electroporation [61]. Figures 2(a) and 2(b) show for any



given electric field, effects on plasma membrane integrity were less for the shorter pulses [61]. Figures 2(c) and 2(d) show results from HL-60 cells. Pulse durations of 10 ns and 60 ns were used, with a similar total energy input. The effects on the plasma membrane were seen to be stronger with increasing pulse number for both 10 and 60 ns pulses, but the effects were stronger for the longer 60 ns pulse, as compared to the 10 ns duration [61].

Cell apoptosis has been observed for cells subjected to short electrical pulses. Figure 3 shows data on caspase activity in Jurkat cells subjected to a single pulse of variable duration but fixed total energy of 1.7 J/cc. Three pulse durations 10 ns, 60 ns and 300 ns were used. The main result is longer duration pulses are seen to produce stronger apoptotic behavior, with a clear monotonic trend [38].

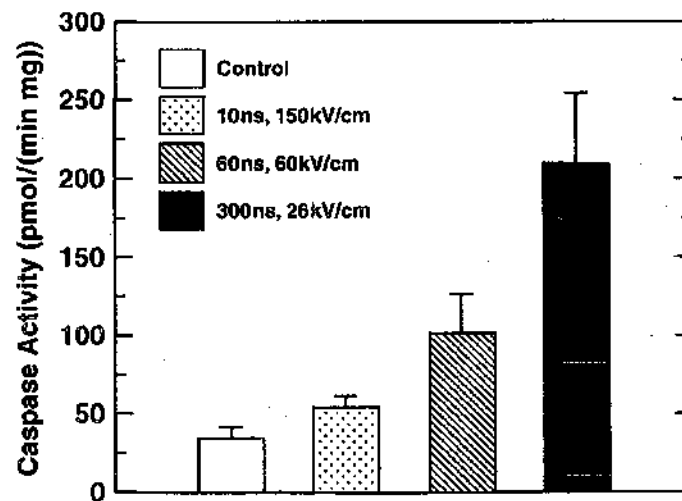


**Figure 3.** Data showing caspase activity in Jurkat cells subjected to a single pulse of variable duration, but fixed total energy of 1.7 J/cc. Longer duration pulses are seen to produce stronger apoptotic response [38].

The effect of short electrical pulses on the cell nucleus has been explored by using acridine orange (AO), a vital fluorescent dye [62]. A 10 ns, 65 kV/cm pulse was applied on HL-60 cells. Experiments show an exponential decrease in average fluorescence

intensity in the nucleus with a time constant of approximately 3 minutes [63]. Figure 4 shows the decrease in fluorescence in the nucleus correlates to an increase in fluorescence in the entire cytoplasm. These results show that nanosecond pulses cause an increase in the permeability of the nuclear membrane [63].

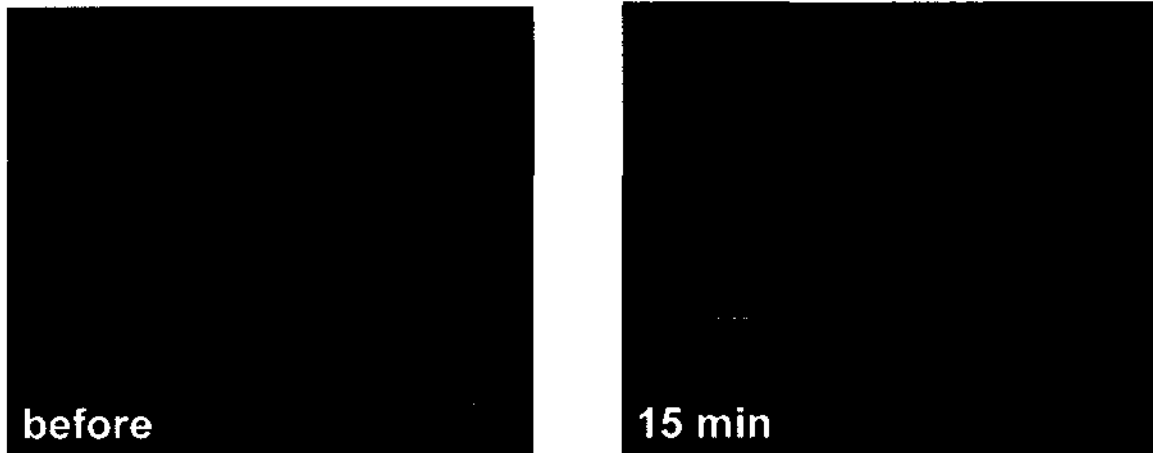


**Figure 4. Images of HL-60 cells before and 15 min after applying a 10 ns, 60 kV/cm pulse. The cells were stained with acridine orange (AO) a stain that indicates DNA damage [63].**

Experiments also show calcium is released from the intracellular endoplasmic reticulum in response to external voltage pulses [63]. After being exposed to a 60 ns, 100 kV/cm pulse, the release of calcium was observed within the first 18 ms and reaches a maximum in less than a second before it decreases in an exponential manner over 2-3 minutes (Figure 5) [63].

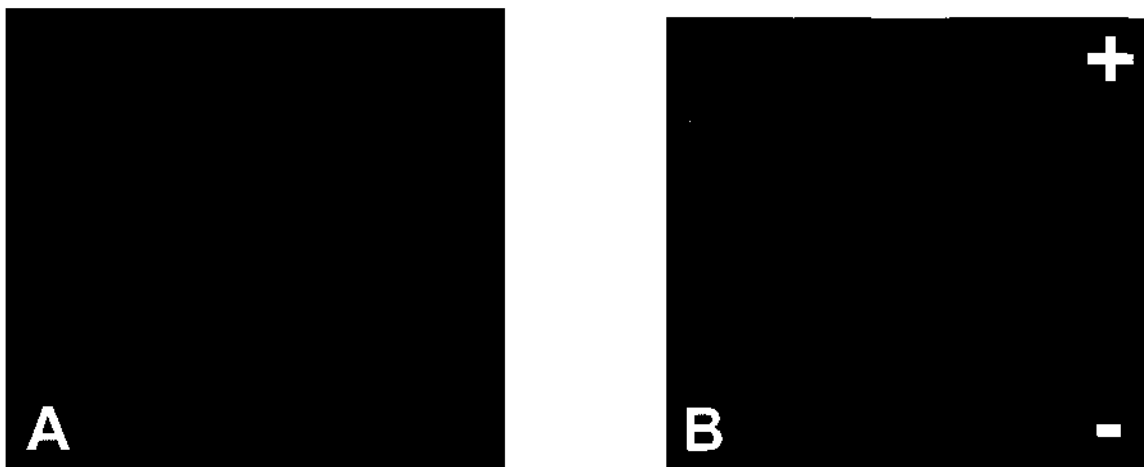


**Figure 5. (A)** A Jurkat cell stained with Bodipy Brefeldin A 558/568, a dye primarily taken up in the endoplasmic reticulum thus indicating the location of this organelle inside the cell. **(B)** Within 18 ms after the application of a 60 ns pulsed electric field of 100 kV/cm a Jurkat cell shows an increase in intracellular calcium, here indicated by the fluorescent marker Fluo-4 AM. The comparison of both images shows that calcium is first released from the area of the endoplasmic reticulum and subsequently increases over the entire cell volume as seen with increasing fluorescence intensity [63].

### 2.3 Simulation Schemes for Predicting Bioelectric Effects

There has been a general consensus that there must be a trade-off between the level of detail and efficiency in simulating bio-cellular responses in order to achieve long time and length-scale results. At the highest level of detail, there are the atomistic models [58-60]. Such atomistic [also referred to as Molecular Dynamics (MD)] simulations yield insights into the atomic structure and configurations of membranes and organelles; however, they are unable to simulate long time scales (e.g., over 50 ns) or large systems such as whole-cells. Alternatively, different levels of coarse graining were attempted in order to achieve longer time and length scales. These include molecular simulations using lattice and off-lattice models [58, 134]. These models do not take into consideration the atomistic details and are still not efficient enough to simulate large systems over long time periods (e.g., over 1 ms). At the next level of coarse graining are mesoscopic models such as the continuum and Lattice Boltzmann models [58, 135]. In summary, each of the

approaches mentioned above can be successful in shedding light on specific aspects of cellular responses at the various time-scales and level of details. However, if the aim is to simulate the full behavior of a large system including all the intricate details then an approach needs to be developed that takes into account both atomistic and continuum scales. Such simulation techniques are commonly referred to as “multi-scale” models [59, 136-141].

### **2.3.1 Molecular Dynamics**

Molecular dynamics (MD) is the most basic approach to understanding electric field-membrane interactions on a nanoscale. MD is a time-dependent, many-body, kinetic scheme that follows the trajectories of N-interaction bodies subject to chosen external fields. It is a microscopic approach that specifically treats every atom within the chosen simulation region [32]. It relies on the application of classical Newtonian mechanics for the dynamic movement of ions and neutral atoms, taking account of the many-body interactions within a realistic molecular representation of the bio-system [63]. The results of MD calculations shed light on the physics of such interactions, and provide information on critical electric fields for field-membrane interactions [63].

This method is superior to continuum approaches for the following reasons [63]: (i) it allows for the inclusion of collective, many-body interaction potentials at the nanoscale level; (ii) dynamic screening and dynamic variations in the internal force fields and potentials are automatically included; (iii) it avoids the “mean-field” approximations; (iv) it provides for a natural inclusion of noise and statistical fluctuations; (v) it facilitates self-consistent transport calculations without invoking arbitrary fitting parameters such as

the mobility; (vi) it easily facilitates the incorporation of arbitrary defects and non-uniformities, as well as complex geometries.

MD is essential in the present context of high-voltage, ultra-short pulses for the following reasons [63]: (a) the highly non-equilibrium situation precludes the use of “mean-field”, “quasi-equilibrium”, or “averaged-continuum” theories; (b) since bio-responses such as conformational changes, poration, etc. are all based on the movement of a small number of actual molecules, a nano-scale atomic-level treatment becomes critical to capture the realistic picture; (c) it also circumvents the need to introduce simulation parameters such as diffusion and rate constants that may not be well characterized or might have values that differ from their assumed equilibrium levels.

### 2.3.2 Smoluchowski-Based Continuum Theory and Rate Equation Analyses for Kinetics

In keeping with the literature, predictions of pore generation, growth and size-evolution could be based on continuum Smoluchowski theory, with the following governing equation for the pore density distribution function  $n(r, t)$ , with  $r$  being the pore radius [44]:

$$\frac{\partial n(r, t)}{\partial t} - \frac{D}{k_B T} \times \frac{\partial [n(r, t) \cdot \partial E(r) / \partial r]}{\partial r} - D \cdot \frac{\partial^2 n(r, t)}{\partial r^2} = S(r), \quad (2.3.1)$$

where  $S(r)$  is the source term,  $D$  is the pore diffusion constant,  $T$  the operating temperature, and  $k_B$  the Boltzmann constant. Generally, the formation of pores is assumed to be a two-step process. All pores are initially created as hydrophobic, at a rate

$S(r)$  per unit area of the membrane, during every time interval “dt.” The rate is given by [44]:

$$S(r) = \frac{v_c h}{k_B T} \cdot \frac{dE(r)}{dr} \cdot \exp[-E(r)/(k_B T)] \cdot dr, \quad (2.3.2)$$

where  $v_c$  is an attempt rate density,  $E(r)$  the energy for hydrophobic pores,  $T$  the operating temperature, and  $k_B$  the Boltzmann constant. If a hydrophobic pore is created with a radius  $r > r^*$  ( $=0.5\text{nm}$ ), it transforms into a hydrophilic pore. Then all hydrophilic pores survive as long as their radii remain larger than  $r^*$ . Destruction of a hydrophilic pore occurs only if it drifts or diffuses in  $r$ -space to a value below  $r^*$  [44].

It is thus clear from equations (2.3.1) and (2.3.2) that the energy  $E(r)$  is the most important entity that governs the pore formation, growth and decay. This energy  $E(r)$ , which is a function of the pore radius “ $r$ ,” determines the “drift flux” for pores in  $r$ -space and the formation rate. It depends on several factors such as the membrane tension, the applied voltage and associated stored electrostatic energy, and steric repulsion. The published and accepted models of  $E(r)$  for hydrophobic and hydrophilic pores, respectively, are [44, 112, 115-117, 119]:

$$E(r) = 2\pi \cdot h \cdot r \cdot \sigma(\infty) \cdot \frac{I_1(r/r_0)}{I_0(r/r_0)} - \pi \cdot a_p \cdot V^2 \cdot r^2, \quad (2.3.3a)$$

$$E(r) = 2\pi \cdot \gamma \cdot r - \int_0^r 2\pi \cdot \Gamma(r^*) \cdot r^* \cdot dr^* + (C/r)^4 - \pi \cdot a_p \cdot V^2 \cdot r^2. \quad (2.3.3b)$$

In the above,  $I_1$  and  $I_0$  are the modified Bessel functions of the zeroth and first order, respectively,  $h$  is the membrane thickness,  $\sigma(\infty)$  is a constant equal to  $5 \times 10^{-2} \text{Nm}^{-1}$ , while  $r_0$  is a characteristic length scale over which the properties of water change between the interface and the bulk, taken to equal  $1\text{nm}$  [44]. The  $(C/r)^4$  term in equation (2.3.3b)

accounts for steric repulsion between the lipid heads lining the pore, and contributes to an increase in energy with shrinking radius [44]. The typical value of C was chosen to be  $9.67 \times 10^{-15} \text{ J}^{0.25} \text{ m}$  [126]. The last term  $\pi \cdot a_p \cdot V^2 \cdot r^2$  in equation (2.3.3b) represents the capacitive contribution to the energy in the presence of a trans-membrane potential “V.” The coefficient  $a_p$  is a property of the membrane and its aqueous environment. In the simplest continuum approximation, it is expressed in terms of the membrane thickness “h” and the permittivities “ $\epsilon_w$ ” and “ $\epsilon_m$ ” of water and the membrane, respectively, as  $a_p = (\epsilon_w - \epsilon_m)/(2h)$  [44].  $\gamma$  represents the energy per unit length of the pore perimeter, while  $\Gamma$  is the energy per unit area of the intact membrane which is usually taken to be a constant parameter [126], yielding the following formation energy expression for hydrophilic pores [44]:

$$E(r) = 2\pi \cdot \gamma \cdot r - \pi \cdot \Gamma_0 \cdot r^2 + (C/r)^4 - \frac{\epsilon_w - \epsilon_m}{2h} \cdot \pi \cdot V^2 \cdot r^2. \quad (2.3.4)$$

Typical values for the various parameters are given in Table I [64]. The inadequacies of using a constant surface tension are elucidated by considering the predicted voltage-dependent behavior. Plots of  $E(r)$  based on equation (2.3.4) are given in Figure 6. For the zero voltage curve, a local minima occurs roughly at 0.8 nm (corresponding to the most likely pore size under steady-state equilibrium conditions), and a local maxima at about 18nm. Hence, all pores with radii less than 18 nm, would tend to drift towards smaller values in r-space. The monotonic increase in pore energy below 18 nm would force pores to shrink in size and approach the dynamically stable radius of 0.8 nm [44]. However, pores having radii greater than this threshold would drift uncontrollably towards larger

**Table I. Parameters used for the theoretical model [64].**

Parameter	Source	Value
$D \text{ (m}^2 \text{ s}^{-1}\text{)}$	Ref. [75]	$5 \times 10^{-14}$
$\gamma \text{ (J m}^{-1}\text{)}$	Ref. [75]	$1.8 \times 10^{-11}$
$\Gamma_0 \text{ (J m}^{-2}\text{)}$	Ref. [75]	$10^{-3}$
$C \text{ (J}^{1/4} \text{ m)}$	Ref. [76]	$9.67 \times 10^{-15}$
$K_w \text{ (F m}^{-1}\text{)}$	Ref. [75]	$80 \times 8.85 \times 10^{-12}$
$K_m \text{ (F m}^{-1}\text{)}$	Ref. [75]	$2 \times 8.85 \times 10^{-12}$
$h \text{ (m)}$	Ref. [76]	$5 \times 10^{-9}$
$a_p \text{ (F m}^{-2}\text{)}$	Ref. [76]	$6.9 \times 10^{-2}$
$v_c \text{ (m}^{-3} \text{ s}^{-1}\text{)}$	Ref. [77]	$2 \times 10^{38}$
$v_d \text{ (s}^{-1}\text{)}$	Ref. [76]	$10^{11}$
$r_0$	Ref. [76]	$1 \times 10^{-9}$

values and expand without bound. Irreversible breakdown and cell rupture would, therefore be the predicted result for pores exceeding the stability threshold radius of 18 nm [44]. At the higher voltage of 0.2 V, both the peak energy and radius of the local maxima shift. The radius for stability reduces to about 5.8 nm. However, for 0.4 V transmembrane potential, the maximum is virtually eliminated. This represents the minimum voltage that would lead to cellular breakdown under this model, provided the voltage was applied long enough to enable pores to grow beyond the 18 nm critical threshold [44]. At the higher voltages of 0.6 V and 0.8 V, the local maxima disappears, and the pores would be unstable due to irreversible, unbounded expansion.



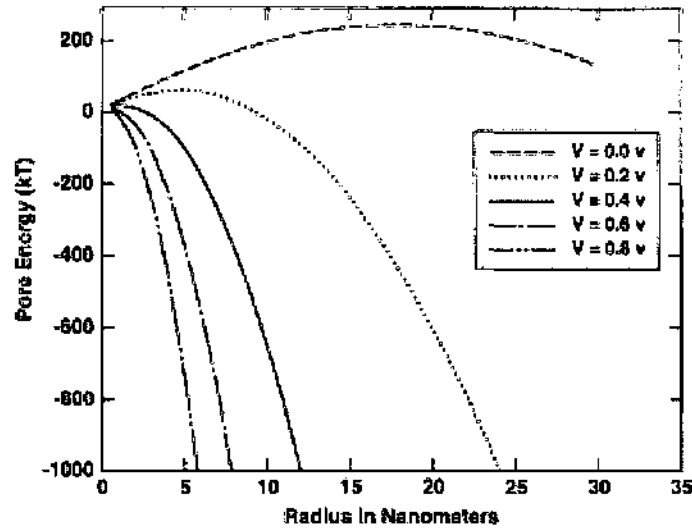


**Figure 6.** The Pore formation energy  $E(r)$  of hydrophilic pores for various membrane voltages [45].

The simple energy model is incorrect and unphysical for the following reasons [44]. (i) As evident from Figure 6, there is no barrier for  $V > 0.4$  V. However, from experimental data, much higher membrane voltages of about 1.0 V for long times are required [44] for irreversible breakdown and membrane rupture. (ii) The use of a constant surface tension becomes questionable as the mechanical properties of cells are expected to change by deformation and changes in membrane area caused by the Maxwell stress tensor associated with an externally applied voltage. Molecular dynamics simulations of lipid bilayers demonstrate variations in the tension with the membrane area [66]. Since tension is proportional to the membrane area, at least to first order, it follows that pore formation will lead to variations in  $\Gamma$  that are proportional to the square of the pore radius [54]. In order to account for this variability, a simple heuristic model was proposed [65] describing the tension as:  $\Gamma(r) = \Gamma_0[1 - r^2/r_\infty^2]$ , with  $r_\infty$  being a constant parameter. It follows that pore formation and growth will lead to reduction of the  $\Gamma$  parameter. The primary effect of such variations in  $\Gamma$  would be the creation of an additional local

minimum in the pore energy function  $E(r)$  which would force the pores to stabilize at some large radius instead of expanding without bound. However, it is important to note that the parameter  $r_{\infty}$  of the heuristic model [65] should not be taken as a constant; instead it should be a time and/or voltage dependent variable to include dynamic effects that would increase the cost of creating additional pores and work to stabilize the pore population. (iii) The formation energy  $E(r)$  in equation (2.3.4) is independent of the pore population and density. However, since the lipid bilayer is essentially elastic and incompressible, it follows that changes in the pore area at constant surfactant molecules, must cause changes in the interfacial free energy [44]. The increased interdigitation of the alkyl chains was invoked as the physical mechanism for changes in both the free energy and  $\Gamma$  [44]. Dependence of the collective pore area and possible pore-pore interaction effects on the parameters of equation (2.3.4) need to be taken into account [44]. The simple energy model is the independent pore model, and is inadequate as the pore population increases. (iv) The parameters in equation (2.3.4) are constant, and there is no dependence on the dynamical evolution of the pores. Not only should  $E(r)$  depend on the pore density “ $n$ ,” but also the magnitude and profile must vary with time in accordance to  $n(r, t)$  [44]. Such a mechanism would make  $E(r)$  self-adjusting in response to  $n(r, t)$ , and not cause uncontrolled pore growth and expansion. It is clear that decreases in surface tension due to pore formation would increase the cost of creating pores that halt further growth and stabilize the pore population.

## CHAPTER III

### MODELING AND SIMULATION DETAILS

#### 3.1 An Improved Pore Area Dependent Energy Model

Application of an electric field can cause poration at cell membranes. This includes the outer plasma membrane as well as the membranes of intracellular organelles. In order to analyze and predict such electroporation effects, it becomes necessary to first evaluate the electric fields and the transmembrane voltages. This information can then be used to assess changes in the pore formation energy that finally yields the pore distributions and their radii based on the Smolchowski equation. The details of evaluating the transmembrane voltage are given next, followed by details of a dynamic pore formation model.

##### 3.1.1 Distributed Circuit Calculations

An approach to calculate the trans-membrane potential is through a time-domain nodal analysis involving a distributed equivalent circuit representation of a cell and its membrane structures. The dynamic membrane electric field can then be obtained from the time-dependent trans-membrane voltage [45]. The entire cell can be broken up into finite segments, and each segment represented by a parallel RC combination to account for the current flow and charging effects [45].

The computational region is a sphere that includes the cell, its substructure, and the surrounding suspension medium. It is discretized in  $r$  and  $\theta$  directions as shown in Figure 7 [45]. For simplicity, only a quarter of the computational region is considered. The plasma membrane is taken as an integral unit, i.e., this subregion is not further discretized. For each element, the current continuity equation is of the form [45]:

$$\nabla \cdot \left( \mathbf{J} + \frac{\partial \mathbf{D}}{\partial t} \right) = 0, \quad (3.1.1)$$

where  $\mathbf{J}$  is the current density and  $\mathbf{D}$  the electric displacement vector. For interior nodes, Eq. (3.1.1) can be rewritten in the following form:

$$\sum_{k=1}^6 \left( \sigma \mathbf{E} + \varepsilon \frac{\partial \mathbf{E}}{\partial t} \right)_k \times A_k = \sum_{k=1}^6 I_k = 0, \quad (3.1.2)$$

where  $I_5$  and  $I_6$  are currents along the  $z$  direction,  $A_k$  the surface area,  $\mathbf{E}$  the electric field,  $\varepsilon$  the permittivity, and  $\sigma$  the conductivity. Considerations of geometric symmetry of the computation region leads to  $I_5 = I_6 = 0$  due to the equi-potentials. Consequently, one obtains the following equation discretized in space and time [45]:

$$\begin{aligned} & \sigma_1 \frac{V^t_{i-1,j} - V^t_{i,j}}{\Delta r} A_1 + \sigma_2 \frac{V^t_{i+1,j} - V^t_{i,j}}{\Delta r} A_2 + \sigma_3 \frac{V^t_{i,j-1} - V^t_{i,j}}{r\Delta\theta} A_3 + \sigma_4 \frac{V^t_{i,j+1} - V^t_{i,j}}{r\Delta\theta} A_4 \\ & + \frac{\varepsilon_1}{\Delta t} \left( \frac{V^{t+1}_{i-1,j} - V^{t+1}_{i,j}}{\Delta r} - \frac{V^t_{i-1,j} - V^t_{i,j}}{\Delta r} \right) A_1 + \frac{\varepsilon_2}{\Delta t} \left( \frac{V^{t+1}_{i+1,j} - V^{t+1}_{i,j}}{\Delta r} - \frac{V^t_{i+1,j} - V^t_{i,j}}{\Delta r} \right) A_2 \\ & + \frac{\varepsilon_3}{\Delta t} \left( \frac{V^{t+1}_{i,j-1} - V^{t+1}_{i,j}}{\Delta r} - \frac{V^t_{i,j-1} - V^t_{i,j}}{\Delta r} \right) A_3 + \frac{\varepsilon_4}{\Delta t} \left( \frac{V^{t+1}_{i,j+1} - V^{t+1}_{i,j}}{\Delta r} - \frac{V^t_{i,j+1} - V^t_{i,j}}{\Delta r} \right) A_4 \\ & = 0, \end{aligned} \quad (3.1.3)$$

In the above,  $V_{i,j}^t$  denotes the potential at node  $(i, j)$  at time  $t$  with  $i = 0, 1, \dots, n$  and  $j = 0, 1, \dots, m$ . The areas  $A_1$  through  $A_4$  are shown in Figure 7. Also,  $\sigma_1$  through  $\sigma_4$ , and  $\varepsilon_1$  through  $\varepsilon_4$  are conductivities and permittivities, respectively, at faces 1-4. Thus, if a node is within the same environmental medium, all the  $\sigma$  values will be the same. However, for nodes on a membrane,  $\sigma_1$  would be different from  $\sigma_2$ .

In order to reduce the computation load, special boundary conditions were applied, and only a quarter of the entire computational region was considered based on the inherent symmetry. Nodes with  $j = 0$  and  $j = m$  had to be treated carefully. Only  $I_1, I_2$  and

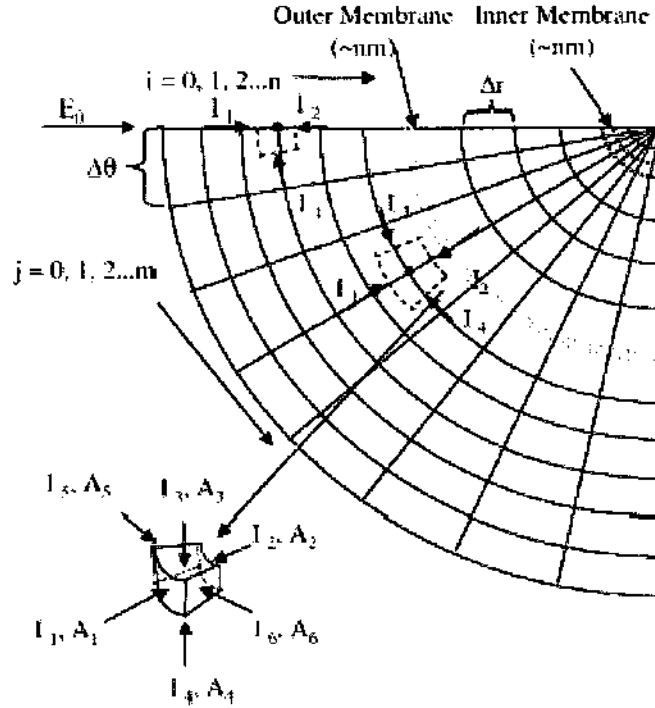


Figure 7. Schematic of one-quarter of the model used to represent a cell for the distributed electrical calculation. The dotted box shows a typical element with current flows [45].

$I_4$  are nonzero since the targeted element only has 5 faces as face 3 shrinks to a line. For  $j = 0$  and  $0 < i < n$ , (3.1.3) becomes [45]:

$$\begin{aligned}
 & \sigma_1 \frac{V^t_{i-1,j} - V^t_{i,j}}{\Delta r} \left(r + \frac{\Delta r}{2}\right)^2 [\cos \theta - \cos(\theta + \frac{\Delta \theta}{2})] + \sigma_2 \frac{V^t_{i+1,j} - V^t_{i,j}}{\Delta r} \left(r - \frac{\Delta r}{2}\right)^2 [\cos \theta - \cos(\theta + \frac{\Delta \theta}{2})] \\
 & + \sigma_4 \frac{V^t_{i,j+1} - V^t_{i,j}}{r \Delta \theta} (r \Delta r) \sin(\theta + \frac{\Delta \theta}{2}) + \frac{\varepsilon_1}{\Delta t} \left( \frac{V^{t+1}_{i-1,j} - V^{t+1}_{i,j}}{\Delta r} - \frac{V^t_{i-1,j} - V^t_{i,j}}{\Delta r} \right) \left(r + \frac{\Delta r}{2}\right)^2 [-1 - \cos(\theta + \frac{\Delta \theta}{2})] \\
 & + \frac{\varepsilon_2}{\Delta t} \left( \frac{V^{t+1}_{i+1,j} - V^{t+1}_{i,j}}{\Delta r} - \frac{V^t_{i+1,j} - V^t_{i,j}}{\Delta r} \right) \left(r - \frac{\Delta r}{2}\right)^2 [-1 - \cos(\theta + \frac{\Delta \theta}{2})] \\
 & + \frac{\varepsilon_4}{\Delta t} \left( \frac{V^{t+1}_{i,j+1} - V^{t+1}_{i,j}}{r \Delta \theta} - \frac{V^t_{i,j+1} - V^t_{i,j}}{r \Delta \theta} \right) \times r \Delta r \sin(\theta + \frac{\Delta \theta}{2}) = 0.
 \end{aligned} \tag{3.1.4}$$

In the above,  $\theta = \pi + j \times \Delta \theta = \pi$  and  $\Delta \theta$  is  $(\pi/2)/m$ . For an electric field applied along the  $r$  direction, potential at a node with  $i = n$  is zero. Nodes with index  $j = 0$  are equipotentials, so  $V_{i,m} = V_{n,j} = 0$ . Another boundary condition to be considered is for

nodes with  $i = 0$ . The potentials of such nodes are calculated as  $V_{0,j} = -E_0 R \cos\theta$ , for  $j=0,1,\dots,m$ , where  $E_0$  is the externally applied electrical field, and  $R$  is the radius of the computational region.

Combined with the boundary conditions discussed above, one gets  $N$  equations for the  $N$  unknown node voltages. These  $N$  equations can easily be solved through matrix inversion of the form  $Ax = B$ . Here,  $A$  is a sparse coefficient matrix. Potential on each node is updated at each time step based on the value of the externally applied field.

### 3.1.2 Dynamic Pore Model

The dynamic pore model can be achieved by including a dynamic aspect and a dependence on the pore population density into equation (2.3.4). These changes make the pore formation energy  $E(r)$  self-adjusting in response to pore formation, without causing uncontrolled growth and expansion. The energy equation (2.3.4) can be modified as follows:

$$E(r) = 2\pi \cdot \gamma \cdot r - \int_0^r 2\pi \cdot \Gamma_{eff}(r^*) \cdot r^* \cdot dr^* + (C/r)^4 - \pi \cdot \frac{\epsilon_w - \epsilon_m}{2h} \cdot V^2 \cdot r^2, \quad (3.1.5)$$

where  $\Gamma_{eff}$  is a variable membrane tension. It could be expressed in the presence of pore area  $A_p$  as [45]:

$$\Gamma_{eff}(A_p) = \Gamma_{eff}(A_p = 0) \cdot \frac{1 - [A_0 / (A - A_p)]^2}{1 - (A_0 / A)^2}, \quad (3.1.6)$$

where  $A$  is the total area of a lipid bilayer, and  $A_0$  is the equilibrium area at which the effective tension is zero. It follows that the effective tension can be positive, zero or even negative [64]. The zero level corresponds to a situation where the pore area  $A_p = A - A_0$ . For higher pore area (i.e., larger average pores), the  $\Gamma_{eff}$  value can be negative as the membrane is under compression [64].

## 3.2 High-Intensity Electric Pulse Induced Action Potential Block in Whole-Animal Nerves

Besides inducing pores in cells, external voltages could also be used in principle to modulate action potential generation in nerves. One possibility is to vary the membrane resistance through the induction of nanopores. Such changes would alter the “RC” charging time constants. As a result, the triggering or “firing rates” of neurons could be altered. This leads to the distinct possibility of modulating the muscle force produced by neuro-muscular action. Another possibility of electric-field induced poration in nerve membranes is the blockage of action potential propagation. This block due to a pore-related local short-circuit would be similar in concept to the stopping the propagation of an air-pressure wave down a “leaky” pipe. Details relating to these issues are discussed in the following section.

### 3.2.1 Cable model of nerve propagation

Treatment of AP propagation along nerves was analyzed by Cooley and Dodge [68] and later by McNeal [69] and Rattay [70] based on the distributed transmission line model. In a one-dimensional treatment, the entire nerve discretized spatially into nodes is shown in Figure 8, and the trans-membrane potential at any time for a given node “n” is expressed as [45]:

$$[V_{i-1}(t) - V_i(t)]/R_a - [V_i(t) - V_{i+1}(t)]/R_a + I_{inj}(t) - I_{ch}(t) = d[C_m(t)V_i(t)]/dt, \quad (3.2.1)$$

where  $V_i(t)$  is the net trans-membrane potential at node  $i$ ,  $R_a$  the effective axonal resistance, and  $C_m(t)$  the effective time-dependent membrane capacitance that incorporates dynamic pore formation.  $I_{inj}(t)$  and  $I_{ch}(t)$  represent the injected stimulus current that initiates a propagating action potential and membrane channel current,

respectively, at node  $i$  during time instant  $t$ . The channel current at any node “ $i$ ” consists of the usual sodium and potassium ionic currents through voltage-gated channels and a leakage contribution given as [49, 71]:

$$I_{ch}(t) = g_{Na}m_i^3(t)h_i(t)[V_i(t) - V_{Na}(t)] + g_Kn_i^4(t)[V_i(t) - V_K(t)] + g_L[V_i(t) - V_L(t)] + G_{sh} V_i(t), \quad (3.2.2)$$

where  $g_{Na}$  and  $g_K$  denote the sodium- and potassium-channel conductances, while  $V_{Na}(t)$  and  $V_K(t)$  represent the resting potentials. In order to account for the effects of electroporation, an additional time-dependent shunt conductance  $G_{sh}(t)$  needs to be included in Eq. (3.2.2) and placed as a parallel element in the circuit of Figure 8. The terms  $m_i(t)$  and  $h_i(t)$  denote the time-varying switching variables for the activation and deactivation of sodium channels across the membrane at the  $i^{\text{th}}$  discrete location, while  $n_i(t)$  represents the potassium channel activating switch.

Ionic transfer across the membrane is a stochastic process, and individual channels transfer between open and closed states randomly. These rates of transition are voltage dependent, leading to a net change in ionic transport upon electrical simulation [45]. The collective macroscopic behavior can be expressed in terms of a continuum time-dependent model for all channels. Such a global approach, first suggested by Hodgkin-Huxley [49] for unmyelinated nerves, has been used here and leads to the following dynamic equations for the switching functions  $m(t)$ ,  $h(t)$ , and  $n(t)$  [43]:

$$d[m_i(t)]/dt = \alpha_m(t)\{1-m_i(t)\} - \beta_m(t)m_i(t), \quad (3.2.3a)$$

$$d[n_i(t)]/dt = \alpha_n(t)\{1-n_i(t)\} - \beta_n(t)n_i(t), \quad (3.2.3b)$$

$$d[h_i(t)]/dt = \alpha_h(t)\{1-h_i(t)\} - \beta_h(t)h_i(t), \quad (3.2.3c)$$

where the voltage-dependent transition rates  $\alpha_{m,n,h}$  and  $\beta_{m,n,h}$  are give as [43]:



$$\alpha_m(t) = \phi(T)[2.5 - 0.1V_i(t)]/\{\exp[2.5-0.1V_i(t)]-1\}, \quad (3.2.4a)$$

$$\alpha_n(t) = \phi(T)0.1[1 - 0.1V_i(t)]/\{\exp[1-0.1V_i(t)]-1\}, \quad (3.2.4b)$$

$$\alpha_h(t) = \phi(T)0.07/\{\exp[-V_i(t)/20]\}, \quad (3.2.4c)$$

$$\beta_m(t) = \phi(T)4\{\exp[-V_i(t)/18]\}, \quad (3.2.4d)$$

$$\beta_n(t) = \phi(T)0.125\{\exp[-V_i(t)/80]\}, \quad (3.2.4e)$$

$$\beta_h(t) = \phi(T)/\{\exp[3-0.1V_i(t)]+1\}, \quad (3.2.4f)$$

and

$$\phi(T) = 3^{(T-6.3)/10}, \quad (3.2.4g)$$

where  $T$  is the temperature in degrees centigrade. Each node voltage  $V_i(t)$  is time dependent because of external voltage pulsing; hence, the transition rates also become dynamic. For numerical stability and accuracy, the implicit centered-difference scheme can be used for updating the functions  $m_i(t)$ ,  $n_i(t)$  and  $h_i(t)$  at each succeeding time step. This leads to the following discretized equation for  $m_i(t+\Delta t)$  after a time step  $\Delta t$ :

$$m_i(t + \Delta t) = m_i(t) + (\Delta t/2)\{\alpha_{m,i}(t)[1 - m_i(t)] + \alpha_{m,i}(t + \Delta t) - \beta_{m,i}(t) m_i(t)\}/\{1 + (\Delta t/2)[\alpha_{m,i}(t + \Delta t) + \beta_{m,i}(t + \Delta t)]\}. \quad (3.2.5)$$

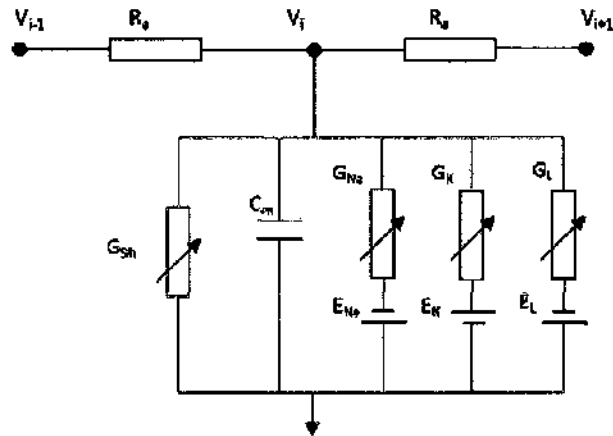


Figure 8. Schematic of the cable model used to represent a nerve fiber [43].

### 3.2.2 Membrane Electroporation Effects

The application of a high-intensity short-duration electric pulse (HISDEP) leads to nanopore formation on the cylindrical membrane surface as shown in Figure 9, so the traditional cable model needs to be modified to account for the increased membrane conductance ( $G_{sh}(t)$ ) and the altered membrane capacitance ( $C_m(t)$ ). These parameters are determined by the number of pores formed for a given voltage amplitude and pulse duration. The dynamics of pore creation and destruction have been well characterized by continuum approaches based on the Smoluchowski equation [70].

The same set of equations in 3.1 is used for an evaluation of the pore probability density distribution  $n(r, t)$  at each time step, in response to a given time-dependent transmembrane potential  $V(t)$ . The total number of pores,  $N(t)$  can be obtained from the density function  $n(r, t)$  as  $N(t) = \int_0^\infty n(r, t) dr$ . Then the average pore radius  $\langle r(t) \rangle$  at any time instant is  $[\int_0^\infty rn(r, t) dr] / [\int_0^\infty n(r, t) dr]$ . Pore creation also changes the membrane capacitance since water is able to enter the aqueous pathways in the membrane and alter

the local permittivity. The effective capacitance  $C_m(t)$  per unit longitudinal distance  $dz$  is given as [43]:

$$C_m(t) = \frac{\epsilon_w A_p + \epsilon_m A_{mem}}{h} = \frac{\epsilon_w}{h} (dz) \int_0^\pi (R_i + R_o) d\theta \int_0^\infty n(r, \theta, t) dr + \frac{\epsilon_m}{h} (\pi(R_i + R_o) dz - dz) \int_0^\pi (R_i + R_o) d\theta \int_0^\infty n(r, \theta, t) dr, \quad (3.2.6)$$

where  $A_p$  and  $A_{mem}$  are the pore area and membrane surface, respectively, while  $R_i$  and  $R_o$  are the inner and outer radii of the nerve fiber (membrane thickness  $h=R_o - R_i$ ).

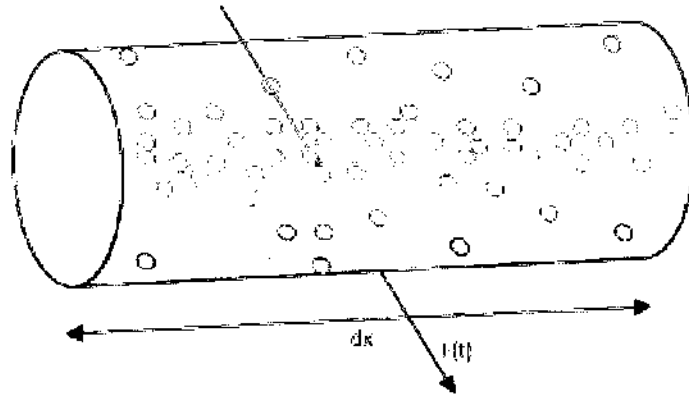


Figure 9. Sketch of pores created on the nerve membrane by the external voltage. A differential  $dx$  of the nerve fiber is shown, and the external field is normal to the longitudinal axis [43].

### 3.2.3 Pore-Facilitated Membrane Conductivity

Membrane conductivity is updated by pore formation and qualitatively depends on the number of pores, their effective radii, the energy barrier to flow produced by the ionic interactions between the pore and surrounding dielectric, and the spreading resistance[43].

The pore conductivity  $G_{pore}$  was taken to be [43]:

$$G_{pore}(t) = \frac{\pi R_o^2 H N(t) \{ \exp[U(t)] - 1 \}}{U(t) \int_0^h dx \exp[U(t) \times (1 - \frac{x}{h}) + \frac{W(x)}{k_B T}]}, \quad (3.2.7)$$

where  $U(t) = \{V(t) \cdot q\} / (k_B T)$ ,  $q$  the electronic charge,  $H$  the conductivity of the aqueous solution,  $V(t)$  the time-dependent trans-membrane potential,  $h$  the membrane thickness,  $N(t)$  the number of pores, and  $W(x)$  the energy barrier for an ion inside the pore. The  $W(x)$  profile has a trapezoidal shape with a linearly varying region of thickness  $d$  at the two ends of the pore and a constant value of  $W_0$  over the central pore region. Thus,  $W(x)$  can be represented mathematically [43]:

$$\begin{aligned} W(x) &= W_0 & d < x < (h-d), \\ W(x) &= W_0 x / d & 0 < x < d, \\ W(x) &= W_0 [(h-x) / d] & (h-d) < x < h. \end{aligned} \quad (3.2.8)$$

Typically,  $W_0$  is much larger than the thermal energy  $k_B T$ . The pore conductivity simplifies to [43]:

$$G_{pore}(t) = \frac{L_z \int_0^\pi d\theta \int_0^\infty [n(r, \theta, t) dr \cdot r^2 HD / h]}{[1 + P(t)] \times \exp\left[\frac{W_0}{k_B T} - \eta U(t)\right] - P(t)}, \quad (3.2.9)$$

where  $P(t) = [\eta U(t)] / [W_0 / (k_B T) - \eta U(t)]$ ,  $\eta = d/h$  is a measure of the relative size of the pore,  $D$  the diameter of the nerve fiber,  $L_z$  the internodal segment along the nerve, and  $n(r, \theta, t)$  is the pore density distribution function. Because the number of pores depends on the angular, the pore resistance needs to be evaluated across differential stripes of width  $Rd\theta$  and longitudinal length  $L_z$  across the nerve membrane [43]. Thus, the overall shunt conductivity  $G_{sh}$  is obtained by adding the spreading resistance at the pore entrance to the effective pore resistivity [43]:  $G_{sh} = [1/G_{pore} + R_{sp}]^{-1}$ , where the pore spreading resistance  $R_{sp} = \rho/2r$  and  $\rho$  is the resistivity of the aqueous medium.

### 3.3 Threshold Process in Cellular Apoptosis Induced by Nanosecond, High-Intensity Electric Pulses

Despite its importance and potential applications, the biophysical details and mechanisms of triggering cellular apoptotic pathways by external electrical stimuli have not been studied, nor well understood. What is already well known is that apoptosis plays a central role in the development of all multicellular organisms and in maintaining their homeostatic balance [6-8]. Also, there are multiple apoptotic pathways; among them are the so-called extrinsic pathway instigated at the cellular plasma membrane and the intrinsic, mitochondrial-initiated process. The former pathway can be triggered by extracellular death signals, deprivation of survival signals, genetic or toxicological damage [75], or as recently reported by external electrical pulsing [39, 41]. A common observation in response to these stimuli is the activation of caspases, a group of cysteine proteases that serve as the main effectors of apoptosis. For example, death receptors, such as CD95, enable the binding or clustering of molecules to form the death-inducing signalling complex (DISC) [72-73]. Molecules involved in DISC formation include oligomerized CD95, the adaptor molecule FADD, procaspase-8, procaspase-10, c-FLIP<sub>L</sub>, and c-FLIP<sub>S</sub>. Trimerization of death receptors upon cross-linking recruits pro-caspase-8, and subsequent proteolytic activation through several cleavage steps (based on proximity induced dimerization) leads to active caspase-8 (C8) production. In this overall process, the presence of c-FLIP is thought to block or interfere with procaspase-8 binding to DISC, and hence, mitigate apoptosis.

The mitochondria-dependent activation (intrinsic pathway) involves *cytochrome c* release from mitochondria induced by stress, irradiation, or inflammation [74, 79, 129-

132]. In the more recent electrical pulsing context [41, 74], it is postulated that the external voltage modulates the transmembrane mitochondrial potential. This could open the mitochondrial permeability transition pore [76, 79], leading to *cytochrome c* release with subsequent downstream apoptotic events. There is also a linkage between the plasma membrane initiated events and the mitochondrial processes since caspase-8 has been shown to cleave the Bcl-2 family member Bid, permitting its carboxy-terminal end to translocate to the outer mitochondrial membrane causing release of *cytochrome c* [77]. A mathematical model of this cascade leading to the activation of caspase-3 (C3) and the eventual DNA fragmentation and cell death was discussed by Bagci et al. [78]. Briefly, the mitochondrial apoptotic pathway is largely mediated through Bcl-2 family proteins, which include both proapoptotic members such as Bax and Bak that promote mitochondrial permeability, and anti-apoptotic members such as Bcl-2 and Bcl-xL that inhibit their effects or prevent the mitochondrial release of *cytochrome c* [77]. Another important component is the tumor suppressor protein p53, which simultaneously suppresses Bcl-2 and activates Bax. The *cytochrome c* leakage supports formation of an apoptosome complex by binding to apoptotic protease activating factor-1 (Apaf-1), which activates the caspase-9 molecules, and in turn caspase-3 [120]. Caspase-3 (C3) leads to DNA degradation or fragmentation [80], whereas the inhibitor of apoptosis (IAP) inhibits both caspase-3 and caspase-9 activities.

The role and extent of electric field modifications of the apoptotic pathways are unclear. Possible consequences of the applied field can be conjectured. These include the stimulation of CD95 and recruitment of procaspase-8 through conformational changes and enhanced dipole-interactions. Another possibility is that membrane poration leads to

molecular diffusion through the pore bottleneck, as has been observed in the case of Phosphatidylserine externalization [40, 67]. This should increase the proximity between molecules and enhance their interactions. Also, conceivably, c-FLIP repulsion may occur decreasing the competition and interference with procaspase-8 at the membrane binding sites. Furthermore, it is not clear whether the apoptotic effect on cells depends on the electric field magnitude at specific membrane sites. Assuming that molecular clustering and dimerization is a discrete, distributed event, the impact on any given cell would conceivably depend on its orientation with respect to the electric field. Thus, the response magnitude could vary leading to some cells with large procaspase-8 recruitment and subsequent cleavage based on the proximity effect, provided the local field at the discrete, initiating sites was large. In some other cells, however, sub-optimal orientation might lead to weak caspase-8 activation. Another relevant question in this context is the relative importance of the extrinsic process *vis-a-vis* the mitochondrial pathway. Last but not least is the origin of the threshold effect that has been observed with regards to cell survival and its exponential decrease with pulse number beyond the threshold.

Here we attempt to probe some of the above issues. In particular, the pulse number dependent cell survival trends are quantified based on a biophysical model of the cellular apoptotic processes. Time-dependent evolution of the caspase concentrations and the various molecular species are simulated. The numerical evaluations provide qualitative predictions of pulse number cell survival, the relative assessment of extrinsic and intrinsic pathways, and rough predictions of the time duration over which irreversible activation at the molecular level could be initiated by the electric pulses.

Time dependent kinetics of the caspases as well as the various molecular species within the apoptotic pathway were simulated using the rate equation model proposed by Bagci et al. [78]. A schematic of the pathways starting from the release of C8 was given in Figure 10 [78] resulting in the cleavage of Bid. This model contains a system of 31 coupled ordinary differential equations [78] for the temporal evolution of the various concentrations:

$$d[\text{Apaf-1}]/dt = -J_1 + J_{\text{Apaf-1}} \quad (3.3.1a)$$

$$d[\text{cyt c}\cdot\text{Apaf-1}]/dt = J_1 - 7J_{1b} \quad (3.3.1b)$$

$$d[\text{apop}]/dt = J_{1b} - J_2 + J_{4b} \quad (3.3.1c)$$

$$d[\text{apop}\cdot\text{pro9}]/dt = J_2 - J_3 \quad (3.3.1d)$$

$$d[\text{apop}\cdot(\text{pro9})_2]/dt = J_3 - J_3^f \quad (3.3.1e)$$

$$d[\text{apop}\cdot(\text{casp9})_2]/dt = J_3^f - J_4 - J_{5c} - J_{6b} + J_{6b}^f \quad (3.3.1f)$$

$$d[\text{apop}\cdot\text{casp9}]/dt = J_4 + J_{4b} - J_{5b} \quad (3.3.1g)$$

$$d[\text{casp9}]/dt = J_4 - J_{4b} - J_5 - J_6 + J_6^f + J_{\text{casp9}} \quad (3.3.1h)$$

$$d[\text{pro9}]/dt = -J_2 - J_3 + J_{\text{pro9}} \quad (3.3.1i)$$

$$d[\text{IAP}]/dt = -J_5 - J_{5b} - J_{5c} - J_7 + J_{\text{IAP}} \quad (3.3.1j)$$

$$d[\text{casp9}\cdot\text{IAP}]/dt = J_5 \quad (3.3.1k)$$

$$d[\text{apop}\cdot\text{casp9}\cdot\text{IAP}]/dt = J_{5b} \quad (3.3.1l)$$

$$d[\text{apop}\cdot(\text{casp9})_2\cdot\text{IAP}]/dt = J_{5c} \quad (3.3.1m)$$

$$d[\text{casp3}\cdot\text{IAP}]/dt = J_7 \quad (3.3.1n)$$

$$d[\text{pro3}]/dt = -J_6 - J_{6b} + J_{\text{pro3}} \quad (3.3.1o)$$

$$d[\text{casp9}\cdot\text{pro3}]/dt = J_6 - J_6^f \quad (3.3.1p)$$

$$d[\text{apop}\cdot(\text{casp9})_2\cdot\text{pro3}]/dt = J_{6b} - J_{6b}^f \quad (3.3.1q)$$



$$d[\text{casp3}]/dt = J_6^f + J_{6b}^f - J_7 - J_8 + J_8^f - J_9 + J_9^f + J_{\text{casp3}} \quad (3.3.1r)$$

$$d[\text{casp8}]/dt = -J_0 + J_0^f + J_{\text{casp8}} \quad (3.3.1s)$$

$$d[\text{Bid}]/dt = -J_0 - J_8 + J_{\text{Bid}} \quad (3.3.1t)$$

$$d[\text{casp8} \cdot \text{Bid}]/dt = J_0 - J_0^f \quad (3.3.1u)$$

$$d[\text{Bcl-2}]/dt = -J_9 - J_{13} + J_{\text{Bcl2}} \quad (3.3.1v)$$

$$d[\text{casp3} \cdot \text{Bid}]/dt = J_8 - J_8^f \quad (3.3.1w)$$

$$d[\text{casp3} \cdot \text{Bcl-2}]/dt = J_9 - J_9^f \quad (3.3.1x)$$

$$d[\text{Bax}]/dt = -J_{12a} - J_{12b} - J_{13} + J_{\text{Bax}} \quad (3.3.1y)$$

$$d[\text{tBid}]/dt = J_0^f + J_8^f - J_{11} + J_{12b} + J_{\text{tBid}} \quad (3.3.1z)$$

$$d[\text{tBid} \cdot \text{Bax}]/dt = J_{12a} - J_{12b} + J_{\text{tBidBax}} \quad (3.3.1aa)$$

$$d[\text{cyt } c_{\text{mito}}]/dt = -J_{14} + J_{\text{cytmit}} \quad (3.3.1bb)$$

$$d[\text{Bax}_2]/dt = J_{12b} + J_{\text{Bax2}} \quad (3.3.1cc)$$

$$d[\text{tBid}_{\text{mito}}]/dt = J_{11} - J_{12a} + J_{\text{tBidmit}} \quad (3.3.1dd)$$

$$d[\text{cyt } c]/dt = J_{14} - J_1 + J_{\text{cytc}} \quad (3.3.1ee)$$

The reaction rates or fluxes equations are [78]:

$$J_0^+ = k_0^+ [\text{casp8}][\text{Bid}] - k_0^- [\text{casp8} \cdot \text{Bid}] \quad (3.3.2a)$$

$$J_0^f = k_0^f [\text{casp8} \cdot \text{Bid}] \quad (3.3.2b)$$

$$J_1 = k_1^+ [\text{cyt } c][\text{Apaf-1}] - k_1^- [\text{cyt } c \cdot \text{Apaf-1}] \quad (3.3.2c)$$

$$J_{1b} = k_{1b}^+ [\text{cyt } c \cdot \text{Apaf-1}]^p - k_{1b}^- [\text{apop}] \quad (3.3.2d)$$

$$J_2 = k_2^+ [\text{apop}][\text{pro9}] - k_2^- [\text{apop} \cdot \text{pro9}] \quad (3.3.2e)$$

$$J_3 = k_3^+ [\text{apop} \cdot \text{pro9}][\text{pro9}] - k_3^- [\text{apop} \cdot (\text{pro9})_2] \quad (3.3.2f)$$

$$J_3^f = k_3^f [\text{apop} \cdot (\text{pro9})_2] \quad (3.3.2g)$$

$$J_4 = k_4^+ [\text{apop} \cdot (\text{casp9})_2] - k_4^- [\text{apop} \cdot \text{casp9}][\text{casp9}] \quad (3.3.2h)$$

$$J_{4b} = k_{4b}^+ [\text{apop} \cdot \text{casp9}] - k_{4b}^- [\text{apop}][\text{casp9}] \quad (3.3.2i)$$

$$J_5 = k_5^+ [\text{casp9}][\text{IAP}] - k_5^- [\text{casp9} \cdot \text{IAP}] \quad (3.3.2j)$$

$$J_{5b} = k_{5b}^+ [\text{apop} \cdot \text{casp9}][\text{IAP}] - k_{5b}^- [\text{apop} \cdot \text{casp9} \cdot \text{IAP}] \quad (3.3.2k)$$

$$J_{5c} = k_{5c}^+ [\text{apop} \cdot (\text{casp9})_2][\text{IAP}] - k_{5c}^- [\text{apop} \cdot (\text{casp9})_2 \cdot \text{IAP}] \quad (3.3.2l)$$

$$J_6 = k_6^+ [\text{casp9}][\text{pro3}] - k_6^- [\text{casp9} \cdot \text{pro3}] \quad (3.3.2m)$$

$$J_6^f = k_6^f [\text{casp9} \cdot \text{pro3}] \quad (3.3.2n)$$

$$J_{6b} = k_{6b}^+ [\text{apop} \cdot (\text{casp9})_2][\text{pro3}] - k_{6b}^- [\text{apop} \cdot (\text{casp9})_2 \cdot \text{pro3}] \quad (3.3.2o)$$

$$J_{6b}^f = k_{6b}^f [\text{apop} \cdot (\text{casp9})_2 \cdot \text{pro3}] \quad (3.3.2p)$$

$$J_7 = k_7^+ [\text{casp3}][\text{IAP}] - k_7^- [\text{casp3} \cdot \text{IAP}] \quad (3.3.2q)$$

$$J_8 = k_8^+ [\text{casp3}][\text{Bid}] - k_8^- [\text{casp3} \cdot \text{Bid}] \quad (3.3.2r)$$

$$J_8^f = k_8^f [\text{casp3} \cdot \text{Bid}] \quad (3.3.2s)$$

$$J_9 = k_9^+ [\text{casp3}][\text{Bcl2}] - k_9^- [\text{casp3} \cdot \text{Bcl2}] \quad (3.3.2t)$$

$$J_9^f = k_9^f [\text{casp3} \cdot \text{Bcl2}] \quad (3.3.2u)$$

$$J_{11} = k_{11}[\text{tBid}] \quad (3.3.2v)$$

$$J_{12a} = k_{12a}[\text{tBid}_{\text{mito}}][\text{Bax}] \quad (3.3.2w)$$

$$J_{12b} = k_{12b}[\text{tBid} \cdot \text{Bax}][\text{Bax}] \quad (3.3.2x)$$

$$J_{13} = k_{13}[\text{Bcl2}][\text{Bax}] \quad (3.3.2y)$$

$$J_{14} = k_{14}[\text{Bax}_2][\text{cyt } c_{\text{mito}}] \quad (3.3.2z)$$

The production-degradation rates equations are [78]:

$$J_{\text{Apaf-1}} = \Omega_{\text{Apaf-1}} - \mu[\text{Apaf-1}] \quad (3.3.3a)$$

$$J_{\text{IAP}} = \Omega_{\text{IAP}} - \mu[\text{IAP}] \quad (3.3.3b)$$

$$J_{\text{pro3}} = \Omega_{\text{pro3}} - \mu[\text{pro3}] \quad (3.3.3c)$$

$$J_{\text{pro9}} = \Omega_{\text{pro9}} - \mu[\text{pro9}] \quad (3.3.3d)$$

$$J_{\text{Bid}} = \Omega_{\text{Bid}} - \mu[\text{Bid}] \quad (3.3.3e)$$

$$J_{\text{Bcl2}} = \Omega_{\text{Bcl2}} - \mu_{\text{Bcl2}}[\text{Bcl-2}] \quad (3.3.3f)$$

$$J_{\text{Bax}} = \Omega_{\text{Bax}} - \mu_{\text{Bax}}[\text{Bax}] \quad (3.3.3g)$$

$$J_{\text{cytmit}} = \Omega_{\text{cytmit}} - \mu[\text{cyt c}_{\text{mito}}] \quad (3.3.3h)$$

$$J_{\text{casp9}} = - \mu[\text{casp9}] \quad (3.3.3i)$$

$$J_{\text{casp3}} = - \mu[\text{casp3}] \quad (3.3.3j)$$

$$J_{\text{tBid}} = - \mu[\text{tBid}] \quad (3.3.3k)$$

$$J_{\text{tBidBax}} = - \mu[\text{tBid} \cdot \text{Bax}] \quad (3.3.3l)$$

$$J_{\text{Bax2}} = - \mu[\text{Bax}_2] \quad (3.3.3m)$$

$$J_{\text{tBidmit}} = - \mu[\text{tBid}_{\text{mito}}] \quad (3.3.3n)$$

$$J_{\text{cytc}} = - \mu[\text{cyt c}] \quad (3.3.3o)$$

$$J_{\text{casp8}} = - \mu[\text{casp8}] \quad (3.3.3p)$$

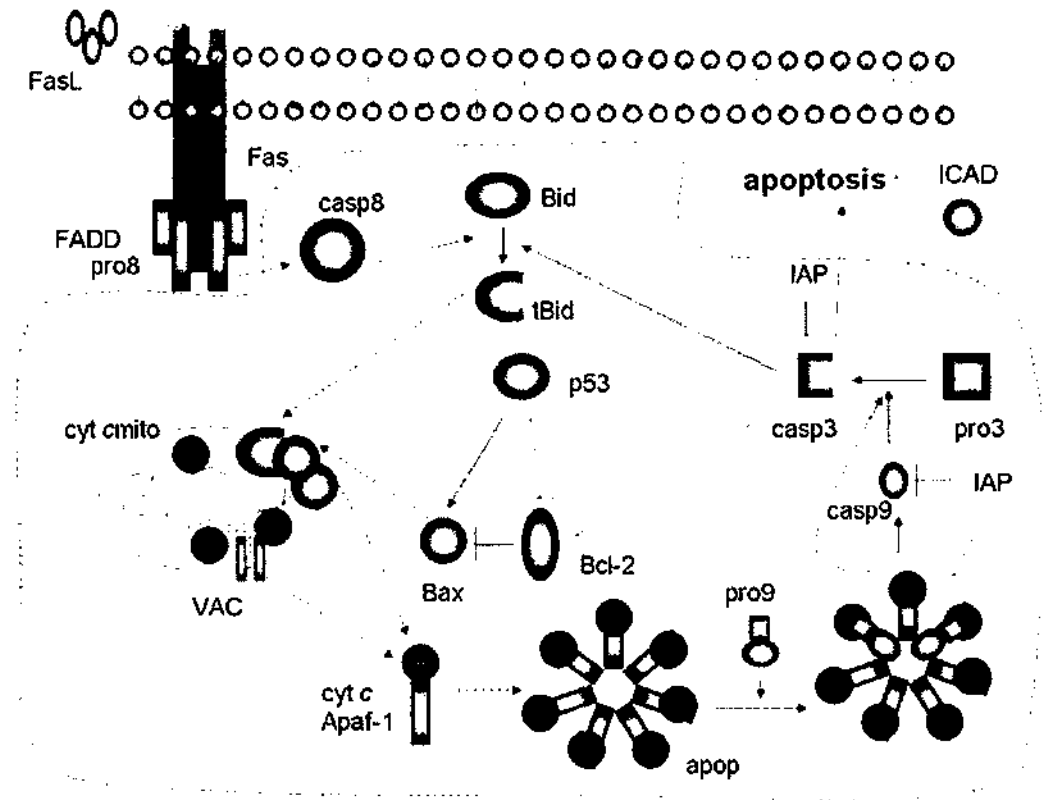


**Figure 10. Mitochondria-dependent apoptotic pathways.** The dotted region indicates the interactions included in this model. Solid arrows denote chemical reactions or upregulation; those terminated by a bar denote inhibition or downregulation; and dashed arrows describe subcellular translocation. The following abbreviations are used: pro8, procaspase-8; casp8, caspase-8; pro9, procaspase-9; casp9, caspase-9; pro3, procaspase-3; casp3, caspase-3; ICAD, inhibitor of caspase activated DNase; cyt c, cytochrome C; apop, apoptosome; VAC, the complex formed by voltage dependent anion channel (VDAC), adenine nucleotide translocase (ANT), and cyclophilin D (CyP-D) at the mitochondrial permeability transition pore [78].

The parameters and other constants for these model calculations were taken from the data and curve fits reported by the Pittsburgh group and given in Table 2. In

Table 2 Parameters used in our simulations [78]

Parameter	Value	Parameter	Value
$k_0^+$	$10 \mu\text{M}^{-1}\text{s}^{-1}$	$k_0^-$	$0.5 \text{s}^{-1}$
$k_0^{\ddagger}$	$0.1 \text{s}^{-1}$	$k_1^+$	$5 \mu\text{M}^{-1}\text{s}^{-1}$
$k_1^-$	$0.5 \text{s}^{-1}$	$k_{1b}^+$	$5 \times 10^4 \mu\text{M}^{-3}\text{s}^{-1}$
$k_{1b}^-$	$0.5 \text{s}^{-1}$	$k_2^+$	$10 \mu\text{M}^{-1}\text{s}^{-1}$
$k_2^-$	$0.5 \text{s}^{-1}$	$k_3^+$	$10 \mu\text{M}^{-1}\text{s}^{-1}$
$k_3^-$	$0.5 \text{s}^{-1}$	$k_3^{\ddagger}$	$0.1 \text{s}^{-1}$
$k_4^+$	$5 \mu\text{M}^{-1}\text{s}^{-1}$	$k_4^-$	$0.5 \text{s}^{-1}$
$k_{4b}^+$	$5 \mu\text{M}^{-1}\text{s}^{-1}$	$k_{4b}^-$	$0.5 \text{s}^{-1}$
$k_5^+$	$5 \mu\text{M}^{-1}\text{s}^{-1}$	$k_5^-$	$0.0035 \text{s}^{-1}$
$k_{5b}^+$	$5 \mu\text{M}^{-1}\text{s}^{-1}$	$k_{5b}^-$	$0.0035 \text{s}^{-1}$
$k_{5c}^+$	$5 \mu\text{M}^{-1}\text{s}^{-1}$	$k_{5c}^-$	$0.0035 \text{s}^{-1}$
$k_6^+$	$10 \mu\text{M}^{-1}\text{s}^{-1}$	$k_6^-$	$0.5 \text{s}^{-1}$
$k_6^{\ddagger}$	$0.001 \text{s}^{-1}$	$k_{6b}^+$	$10 \mu\text{M}^{-1}\text{s}^{-1}$
$k_{6b}^-$	$0.5 \text{s}^{-1}$	$k_{6b}^{\ddagger}$	$0.1 \text{s}^{-1}$
$k_7^+$	$5 \mu\text{M}^{-1}\text{s}^{-1}$	$k_7^-$	$0.0035 \text{s}^{-1}$
$k_8^+$	$10 \mu\text{M}^{-1}\text{s}^{-1}$	$k_8^-$	$0.5 \text{s}^{-1}$
$k_8^{\ddagger}$	$0.1 \text{s}^{-1}$	$k_9^+$	$10 \mu\text{M}^{-1}\text{s}^{-1}$
$k_9^-$	$0.5 \text{s}^{-1}$	$k_9^{\ddagger}$	$0.1 \text{s}^{-1}$
$k_{11}$	$10 \text{s}^{-1}$	$k_{12a}$	$10 \mu\text{M}^{-1}\text{s}^{-1}$
$k_{12b}$	$10 \mu\text{M}^{-1}\text{s}^{-1}$	$k_{13}$	$10 \mu\text{M}^{-1}\text{s}^{-1}$
$k_{14}$	$10 \mu\text{M}^{-1}\text{s}^{-1}$	$p$	4
$[p53]_{\text{thresh}}$	$0.004 \mu\text{M}$	$\mu$	$0.006 \text{s}^{-1}$
$\Omega_{\text{Apaf-1}}$	$3 \times 10^{-4} \mu\text{M/s}$	$\Omega_{\text{IAP}}$	$3 \times 10^{-5} \mu\text{M/s}$
$\Omega_{\text{pro3}}$	$3 \times 10^{-4} \mu\text{M/s}$	$\Omega_{\text{pro9}}$	$3 \times 10^{-4} \mu\text{M/s}$
$\Omega_{\text{Bid}}$	$3 \times 10^{-5} \mu\text{M/s}$	$\Omega_{\text{Bcl2}}$	$8 \times 10^{-5} \mu\text{M/s}$
$\Omega_{\text{Bax}}$	$3 \times 10^{-5} \mu\text{M/s}$	$\Omega_{\text{cytmit}}$	$3 \times 10^{-4} \mu\text{M/s}$
$[\text{cyt } c_{\text{mito}}]$	$0.0066 \mu\text{M}$		

following this apoptotic model, it is inherently assumed that equilibrium levels of the various molecular species exist prior to any electric pulse triggered C8 release. The initial equilibrium concentrations were determined by running the time-dependent rate-equation simulation until steady-state. This model includes the C3-Bid positive feedback process, wherein increases in C3 lead to enhanced cleavage of Bid, which in turn feeds into enhancing the C3 concentrations. The model also includes p53 upregulation and

downregulation of the synthesis of Bax and Bcl-2, respectively [111, 127], as well as the role of inhibitors of apoptosis (IAP). Additionally, the model included first-order degradation kinetics with a uniform rate constant for C8, C3, procaspase-9, procaspase-3, the apoptotic protease activating factor-1 (Apaf-1), IAP, Bcl-2, Bid, tBid, Bax, Bax2, *cytochrome c*, and caspase-9.

As already mentioned, the precise quantitative effect on the external electric field on C8 activation is not known. Furthermore, if C8 release from the DISC occurs at discrete sites located on the plasma membrane, then naturally for a given field, different cells would effectively exhibit varying degrees of C8 activation and release depending on their orientation. From a modeling standpoint, this could be described by assigning random C8 release concentrations to each cell through a stochastic, Monte Carlo type implementation. Hence, for our simulations, the C8 concentration released in each cell was assigned a value " $r \cdot C_{\max}$ ", with " $r$ " being a random number and  $C_{\max}$  a concentration upperbound. Clearly, a large C8 release can be expected to lead to irreversible increases in caspase-3, leading to cell death predictions as characterized by the bistable behavior of the cellular system. Conversely, those cells, randomly chosen to have a small C8 release, can be expected to survive and recover in time. Following Bagci et al. [78], the initial concentrations of all compounds in our simulation were taken to be zero, except for procaspase-3, procaspase-9, Apaf-1, Bid, Bax, Bcl-2, IAP, and *cytochrome c<sub>mito</sub>*, which were all set to 0.004 mM.

The above approach assumes instantaneous C8 release, and then evaluates the temporal evolution of the various chemical complexes based on rate kinetics. However, since a sequence of processes such as the formation of DISC, clustering of procaspase-8

followed by its cleavage etc. are involved, a finite time delay in the occurrence of active caspase-8 is to be expected. Consequently, in response to an electric field impulse, the concentration of C8 must gradually rise as a function of time and eventually saturate. Though this complex biological phenomenon is very difficult to model comprehensively, a recent treatment for CD95-induced apoptosis has been reported [81]. Bentele et al. [81] identified the most critical molecules in the pathway following CD95 activation to estimate some of the unknown parameters and refine a time-dependent model. Their simulations and experiments yield a procedure for evaluating the caspase-8 activation dynamics, and here we use their approach for the DISC-system. Specifically, the reactions and processes shown at the top-left side of Figure 11 [82] were used for the time-dependent C8 evolution. These C8 concentrations were then provided as input to the Bagci rate equation model. In this process, details of the competition between c-FLIP and procaspase-8 in their binding with CD95 automatically get included.

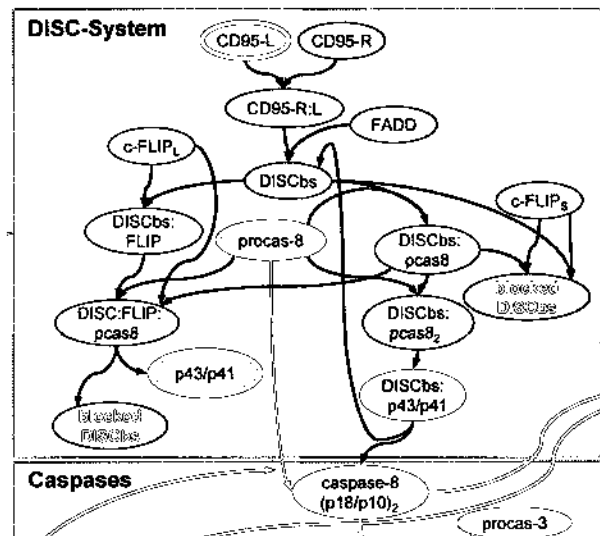


Figure 11. Structured information model of CD95-induced apoptosis [82].

### 3.4 An Asymmetric Electroporation Model

The above model for poration was based on the assumption of symmetric and/or cylindrical pores. However, it is conceivable that the pore shape is not cylindrical, or that it can dynamically change over time, or perhaps even display asymmetry. An asymmetric pore shape would be indicative of differences in current flow directionality. These aspects are explored further in this section.

#### 3.4.1 Pore Energy for Asymmetric Electroporation Model

A perfectly planar membrane containing a pore of circular shape has been analyzed. Because the unfavorable “hydrophobic” interaction of the lipid tails when exposed directly to the aqueous environment, the presence of a membrane pore is likely to imply some structural rearrangement of the lipids at the bilayer rim. Consequently, the lipids within the rim assemble into a semitoroidal cap to shield the hydrocarbon chains from contact with the aqueous environment [83].

The energy required to form a membrane pore, and hence the shape that would minimize this energy, is discussed first. Figure 12 [84] shows a system which consists of a positive electrode  $E_+$  and a negative electrode  $E_-$  separated by a dielectric/conductive fluid  $\Omega$  with permittivity  $\epsilon_w$  and conductivity  $\sigma_w$ . This fluid contains purely dielectric bodies  $M$  with permittivity  $\epsilon_m$ . In Figure 12, electrodes  $E_+$  and  $E_-$  are connected to a battery with a constant voltage difference  $V_m$ .



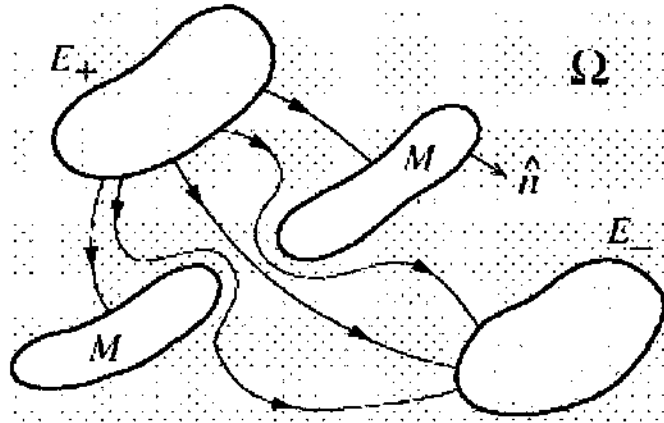


Figure 12. Dielectric body  $M$  in a dielectric/conductive fluid  $\Omega$ .  $E_+$  and  $E_-$  are metal electrodes kept at constant potentials that differ by  $V_m$  [84].

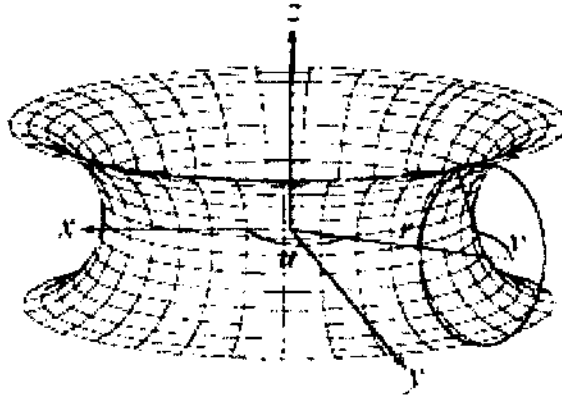


Figure 13. A symmetric toroidal pore [85].

Energy required to form pore  $U_E$  is [84]:

$$U_E = -\int_0^r F(r) dr, \quad (3.4.1)$$

where  $F(r)$  is the total electrical force expanding the pore, computed by integrating the stress  $p_E$  over the pore surface [84],

$$F(r) = \int_S p_E da. \quad (3.4.2)$$

For a toroidal pore (Figure 13 and Figure 14), the computation of the radial force  $F$  should take into account the shape of the pore [84], and hence:

$$F(r) = \int_S p_E \cos \alpha da. \quad (3.4.3)$$

In the above,  $p_E$  is given by [84]:

$$p_E = \frac{1}{2}(\epsilon_w - \epsilon_m)(E_{\parallel}^2 + \frac{\epsilon_w}{\epsilon_m} E_{\perp}^2), \quad (3.4.4)$$

where  $E_{\parallel} = -|E| \cos \alpha$ ,  $E_{\perp} = |E| \sin \alpha$ .

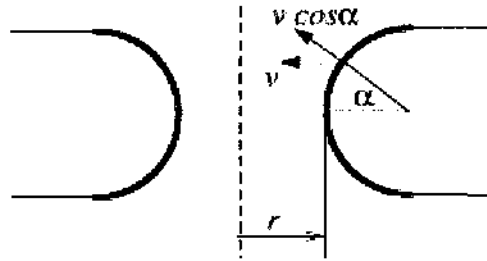


**Figure 14.** Toroidal geometry of pore model inside surface. Heavy line outlines the interior surface of the pore [84].

If the top and bottom portions of the pore are not symmetric, then the radii of the top and bottom halves would be different. This can be taken into account by assigning  $b_T$  and  $b_B$  as the radius of the bottom and top halves, respectively. Figure 15 shows a pore of asymmetric shape; the energy  $U_E$  for the bottom half turns out to be:

$$U_{EB}(r) = \frac{-(\epsilon_w - \epsilon_m)V_m^2 \pi b_B}{b_T + b_B} \left[ r^2 \left( \frac{1}{3} + \frac{\epsilon_w}{6\epsilon_m} \right) + b_B r \left( \frac{2}{3} - \frac{3\pi}{16} + \frac{\epsilon_w}{3\epsilon_m} - \frac{\pi\epsilon_w}{16\epsilon_m} \right) \right]. \quad (3.4.5a)$$

The energy  $U_E$  for the top half turns out to be:

$$U_{ET}(r) = \frac{-(\epsilon_w - \epsilon_m)V_m^2 \pi b_T}{b_T + b_B} \left[ r^2 \left( \frac{1}{3} + \frac{\epsilon_w}{6\epsilon_m} \right) + b_T r \left( \frac{2}{3} - \frac{3\pi}{16} + \frac{\epsilon_w}{3\epsilon_m} - \frac{\pi\epsilon_w}{16\epsilon_m} \right) \right]. \quad (3.4.5b)$$

Regardless of the asymmetric shape, the total surface area of an asymmetric pore is fixed. Thus, the expression:  $2\pi(b_T^2 + b_B^2)$  is fixed. The exact shape of such a pore would be given by values of  $b_T$  and  $b_B$  that minimize the energy subject to the constraint of a fixed  $2\pi(b_T^2 + b_B^2)$  value.

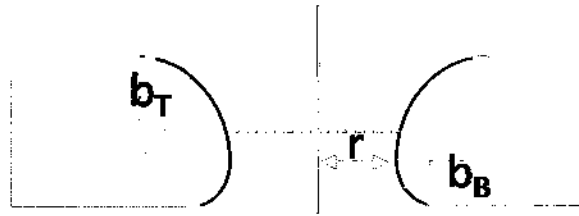


Figure 15. An asymmetric pore model geometry.

### 3.4.2 Mechanical Pore Energy for Asymmetric Electroporation Model

We locate a Cartesian coordinate system at the pore center with the axis of rotational symmetry (the  $z$ -axis) pointing normal to the bilayer midplane as shown in Figure 16 [83]. The height of the cap is also the bilayer thickness  $2b$ , implying a radius,  $b$ , of its circular cross-sectional shape. A parametrization of the semitoroidal cap is given by  $x = b \cos \varphi$  ( $r/b + 1 + \cos \theta$ ),  $y = b \sin \varphi$  ( $r/b + 1 + \cos \theta$ ), and  $z = b \sin \theta$  with  $0 \leq \varphi \leq 2\pi$  and  $\pi/2 \leq \theta \leq 3\pi/2$ . The principal curvatures of the cap are [83]:

$$C_1 = \frac{1}{b}, \quad (3.4.6a)$$

$$C_2 = \frac{\cos \theta}{r + b(1 + \cos \theta)}, \quad (3.4.6b)$$

and the area element [83]:

$$dA_p = b[r + b(1 + \cos \theta)] d\varphi d\theta. \quad (3.4.7)$$

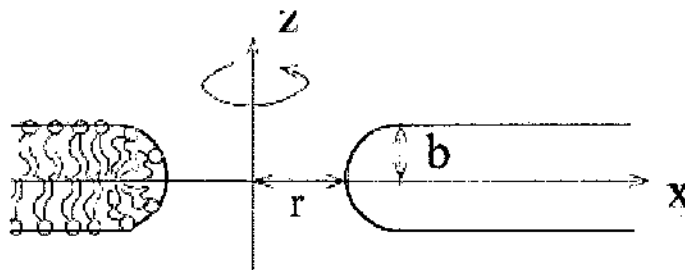


Figure 16. A planar lipid bilayer with a pore in the center. The figure shows the cross-section in the  $x$ - $z$  plane. Rotational symmetry around the  $z$ -axis is indicated. On the left side, the packing of the lipid molecules is shown schematically. The headgroups of lipid molecules are represented by filled circles [83].

Mechanical pore formation energy needs to take into account work done in bending and curving the lipid surface. The free energy turns out to be given as [85-86, 118]:

$$F_c = \iint (2k_c H^2 + k_e K) dS, \quad (3.4.8)$$

where  $H = (C_1 + C_2)$ ,  $K = C_1 C_2$ ,  $dS = 2\pi b[r + b(1 + \cos \theta)] d\theta$ , and  $k_c$  and  $k_e$  are elastic constants,  $k_c = 2 \times 10^{-20}$  J,  $k_e = -0.2 * k_c$  [118]. After some mathematics, the mechanical pore energy for the bottom half of an asymmetric pore is:

$$F_{cB}(r) = 4\pi k_e \left[ \frac{\pi(r + b_B)^2}{b_B \sqrt{r^2 + 2rb_B}} - 1 \right] - 8\pi k_c + 4\pi k_c \left[ \frac{\pi(r + b_B)^2}{b \sqrt{r^2 + 2rb_B}} \right] \left\{ \pi - \tan^{-1} \left[ \frac{\sqrt{r^2 + 2rb_B}}{r + 2b_B} \right] \right\}, \quad (3.4.9a)$$

and the mechanical pore energy for the top half of an asymmetric pore is:

$$F_{cT}(r) = 4\pi k_e \left[ \frac{\pi(r + b_T)^2}{b_T \sqrt{r^2 + 2rb_T}} - 1 \right] - 8\pi k_c + 4\pi k_c \left[ \frac{\pi(r + b_T)^2}{b \sqrt{r^2 + 2rb_T}} \right] \left\{ \pi - \tan^{-1} \left[ \frac{\sqrt{r^2 + 2rb_T}}{r + 2b_T} \right] \right\}. \quad (3.4.9b)$$

Thus, the total mechanical pore energy for the asymmetric pore becomes:

$$F_c = \frac{F_{cB} + F_{cT}}{2}. \quad (3.4.10)$$

The above derived energies due to membrane bending as well as that arising from the external electric field need to be used in any realistic analysis. The result as well as the shape of the pores due to both the bending and electric field effects will be discussed in the next section.

## CHAPTER IV

### SIMULATION RESULTS AND DISCUSSION

#### 4.1 Simulation Results and Discussion of Pore Area Dependent Energy Model

The pore-area dependent model discussed in Chapter 3 was used for predictions of pore formation and their dynamics. Most model analyses in the literature have been based on fixed parameters such as the line tension and elastic rigidity, etc. However, with the formation of pores in a membrane, it is perhaps reasonable to expect that the material characteristics would change. This aspect is probed through simulations and discussed in the next section.

##### 4.1.1 Comparisons of Static and Dynamic Membrane Tension Predictions

Membrane electroporation in response to a 560 kV/cm trapezoidal pulse with an ON time of 1ns and 0.1 ns rise- and fall-times was assumed. The pore distribution  $n(r)$  per unit area was evaluated as a function of radius  $r$  using both a pore-area dependent tension  $\Gamma_{eff}$  and the conventional constant tension  $\Gamma_0$ . For the two-pulse cases, an “idle time” of 0.6 ns was used to separate the second voltage pulse from the first one. Figure 17 shows the results and reveals a distinct shift towards larger pore radii for the fixed tension  $\Gamma_0$  ( $10^{-3}$ ). The most probable pore radius with the dynamic tension is predicted to be less than 0.55 nm; thus, essentially small nano-pores are predicted. This result indirectly agrees with several experimental observations of negligible Propidium Iodide dye uptake following nanosecond pulsing [2, 62, 128]. A possible explanation is that the pore population formed by the ultrashort pulsing has diameters smaller than the dye

dimensions, and hence, disallow for dye uptake by the cells. In Figure 17, using a dynamic membrane tension, the results support this conjecture.

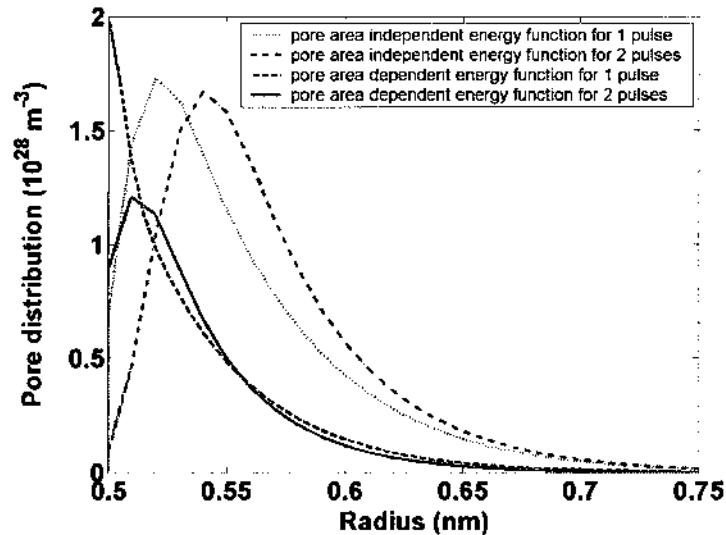


Figure 17. Simulation results of the pore distribution function  $n(r)$  for one- and two-pulses using constant and pore area-dependent tension. A 560 kV/cm fixed external field was used.

Simulation results of the fraction of total pore area to membrane surface area as a function of voltage pulse number are shown in Figure 18. The two curves represent comparisons between results obtained from predictions based on static and dynamic membrane tension. A nearly fixed fraction at about 30% is seen for the dynamic  $\Gamma_{eff}$  case in Figure 18, with a slight monotonic increase. As it turns out, some experimental data is indicative of cell survival and reversible membrane damage on the order of 25% [82]. Thus, our results can be taken to imply a trend that is in keeping with observations. However, with a fixed  $\Gamma_0$  value, a much larger pore fraction is predicted, and this value increases strongly with pulse number. Values in the 45% - 50% range do not seem physical and are unreasonably high if cell viability is to be maintained in the context of such excessive alterations to the membrane structure.

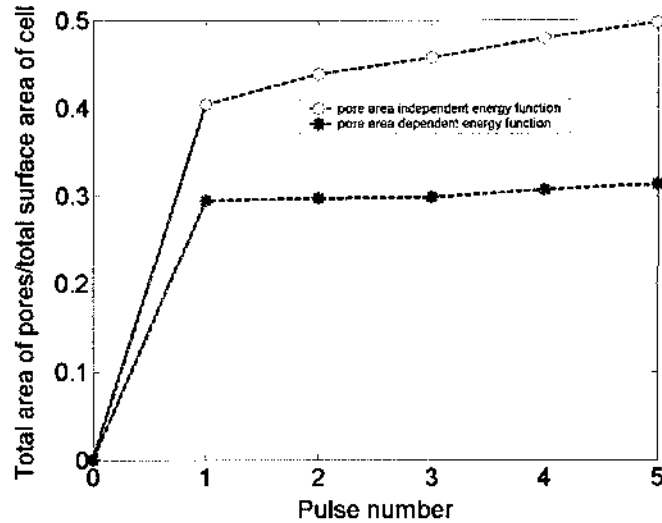


Figure 18. Simulation results of the fraction of total pore area to membrane surface as a function of voltage pulse number. Comparisons of static and dynamic membrane tension predictions are presented.

#### 4.1.2 Membrane Electroporation in Response to a 180kV/cm Trapezoidal Pulse

By using dynamic membrane tension, membrane electroporation results in response to a 180kV/cm trapezoidal pulse with a 10 ns ON time and 1.5 ns rise- and fall-times are discussed next. Figure 19(a) shows the time dependent potential across the plasma membrane at the poles due to this external electrical excitation. A transient peak of about 1.6 V is predicted during the initial rise time of the pulse. This value slightly exceeds the conventional 1.0 V threshold for membrane poration and represents a transient overshoot effect [32, 125]. The initial step rise in transmembrane voltage is driven by the large external displacement current during the 1.5 ns rise time phase [32]. Poration is predicted to occur at times beyond the peak at around 9.2 ns. Following the poration, the potential is predicted to drop due to the dynamic increase in membrane conductivity. This electrical breakdown of the cellular lipid bilayer represents electropermeabilization [32]. The sharp drop at about 11.5 ns agrees with the turn-off phase that provides a large

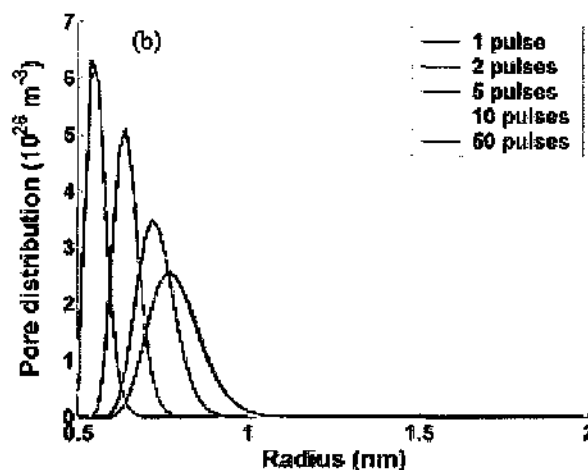
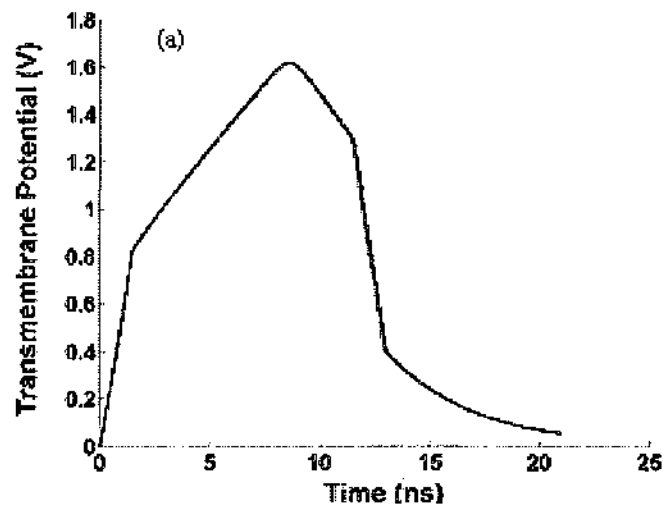
negative external displacement current across the plasma membrane. The complete recovery time of the membrane voltage is about 25 ns or so.

Modeling also yielded time dependent distributions of the membrane pore population after multiple pulsing. Figure 19(b) shows the radial distribution in response to 1, 2, 5, 10 and 50 external pulses. The pulse is still the 10 ns, 180 kV/cm with 1.5 ns rise and fall time used in Figure 19(a), and the simulations were carried out for single as well as multiple pulses. Figure 19(b) shows that the pore distribution shifts to larger values of radius with multiple pulsing [62]. For example, for the shortest 1-pulse excitation, the median value of the pore radius is predicted to be about 0.55 nm, while for a train of 50 pulses, a much bigger median value of the pore radius 0.82 nm is seen in Figure 19(b). In any event, the numerical modeling consistently predicts the pores to have a distribution of radii in the nanometer range [32]. And the pore distribution is seen to broaden due to diffusion in r-space at longer times and upon higher repetitive pulsing.

The total area of pores created dynamically by the electric pulsing can also be computed at any given membrane by the distributed circuit approach. Figure 19(c) shows the results for the outer plasma membrane of a 12  $\mu\text{m}$  cell in response to multiple pulsing. As expected, the total area of pores across the entire surface of the plasma membrane increases monotonically with the number of pulses. A saturating effect is predicted and is due to the interplay between increasing local conductivity of a porated membrane and the associated transmembrane potential that drives the growth of pores [32]. With increasing pulses, the pore density is enhanced, leading to larger increases in membrane conductivity that in turn reduces the transmembrane potential. Pore growth and creation rates are dependent on the transmembrane potential; hence, the reduction effectively



leads to progressive decreases in new pore creation. The net effect is the gradual saturation seen in Figure 19(c). Physically, any cell membrane can only support a finite amount of poration as the process of poration leads to lipid bilayer molecular shifts and creates local tension that increases dynamically with pore area. Beyond a critical area, collective inter-molecular repulsions begin to emerge and resist any further pore creation and molecular displacement [4]. In Figure 19(c), the highest area of about  $11 \times 10^{-11} \text{ m}^2$  represents a peak of 7% poration by surface area. With time, this rapidly reduces as the pores are predicted to reseal upon cessation of the external electric field [4].



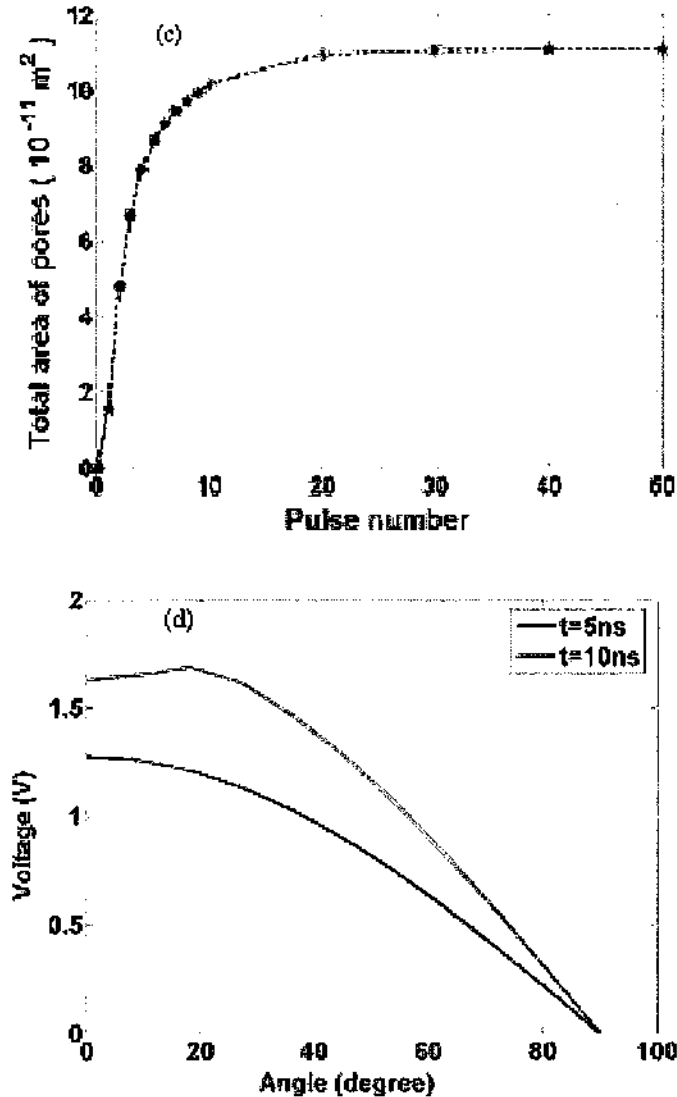


Figure 19. Simulation results in response to an external 180 KV/cm pulse of duration 10 ns and 1.5 ns rise and fall times. (a) Transmembrane potential across the cell membrane. (b) Pore distribution functions at the pole due to various 10 ns, 180 kV/cm pulse excitations. (c) Peak total pore area at the plasma membrane at various pulse numbers, and (d) Angular dependence of  $V_M$  at two different time instants.

Figure 19(d) shows the angular distribution of the transmembrane potential  $V_M$ . As expected, the  $V_M$  value would initially be the highest at the poles (i.e.,  $\theta = 0$ ) as they directly face the external electrodes [32]. However, the value at longer times depends on the interplay between the external electric field, the poration event and the resulting localized conductivity modulation at the membrane. For example, a large external electric

field value would lead to the creation of a high pore density at the poles that, in turn, would increase the conductivity and reduce the local voltage drop across the porated membrane. Simulation results of the angular dependence of  $V_M$  are shown in Figure 19(d) at two time instances. The poles are predicted to have the largest transmembrane voltage initially. Then by about 10 ns (just before pulse termination), the distribution is predicted to have a local maximum away from the poles [32]. This trend is in agreement with the reports by Krassowska and Filev that predict a time-dependent shift of the angular location for the  $V_M(t)$  maxima.

## **4.2 Molecular Dynamics Simulation Results Including Temperature Effects**

For greater accuracy, with inclusion of atomistic details, molecular dynamics (MD) simulations were also carried out during this dissertation research. While the Smoluchowski-based approach is computationally quick, it does not include some of the detailed many-body physics or the process details at the atomic scale. Thus, for completeness, MD simulations were also carried out using the Gromacs software. Some of the results obtained are discussed below.

### **4.2.1 Molecular Dynamics for Cell Membrane Modeling**

Figure 20 shows results of an MD simulation for a fixed field of 0.5 V/nm, carried out to demonstrate nano-pore formation from a microscopic point of view. For example, Figure 20(a) shows the initial configuration of the lipid bilayer with aqueous media on either side. In this figure, the blue region denotes lipid bilayer molecules, while the red-and-white points represent the hydrogen-and-oxygen atoms with a water molecule. Figure 20(b) shows the cross-sectional view of the final membrane configuration

obtained from MD simulations after 1 ns at the constant field of 0.5 V/nm. The pore is predicted to be about 0.9 nm in diameter and somewhat narrower at the central point. A very thin passage-way through the central blue region connecting the upper and lower regions represents a “water nano-wire.”

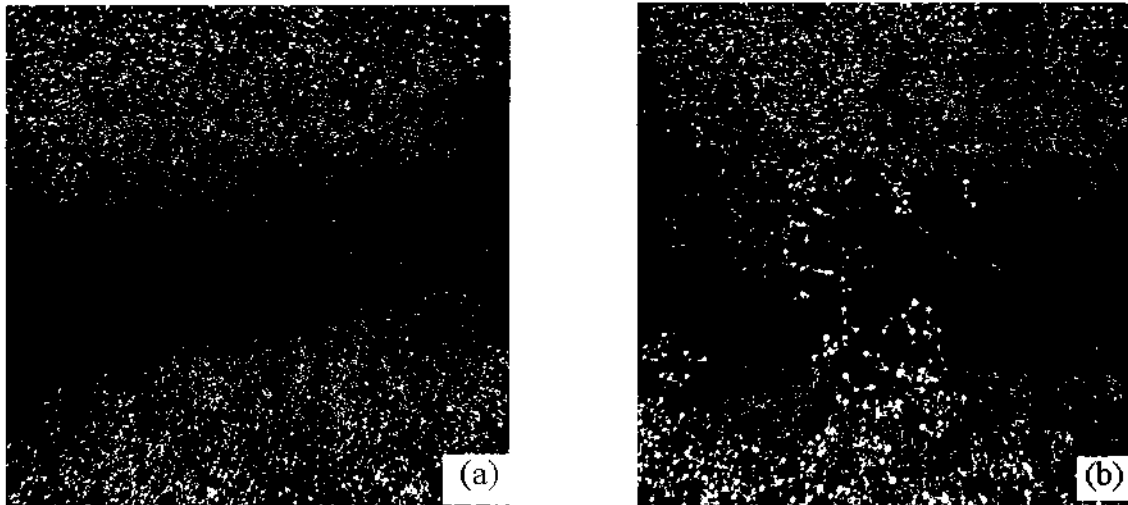


**Figure 20.** MD results showing nano-pore formation at membrane by an external 0.5 V/nm pulsed electric field. Lipids are blue, water is red and white.

#### 4.2.2 Temperature Effects

Almost all studies of electroporation and effects of nanosecond-pulsing on cells have been at room temperature. However, temperature affects the velocities of molecules and lipid chains, as well as the chemical kinetics and reaction rates. It is thus likely to expect that pore formation (as well as other electro-biochemical processes) might be affected by the temperature. Here, the role of temperature in influencing pore formation at the cell outer membrane is probed through molecular dynamics (MD) simulations. From a practical standpoint, exposure of cells to RF or microwave radiation would produce localized temperature rises. The temperature changes would depend on the intensity and

duration of the RF exposure. Hence, any required temperature could, in principle, be attained in biological cells.

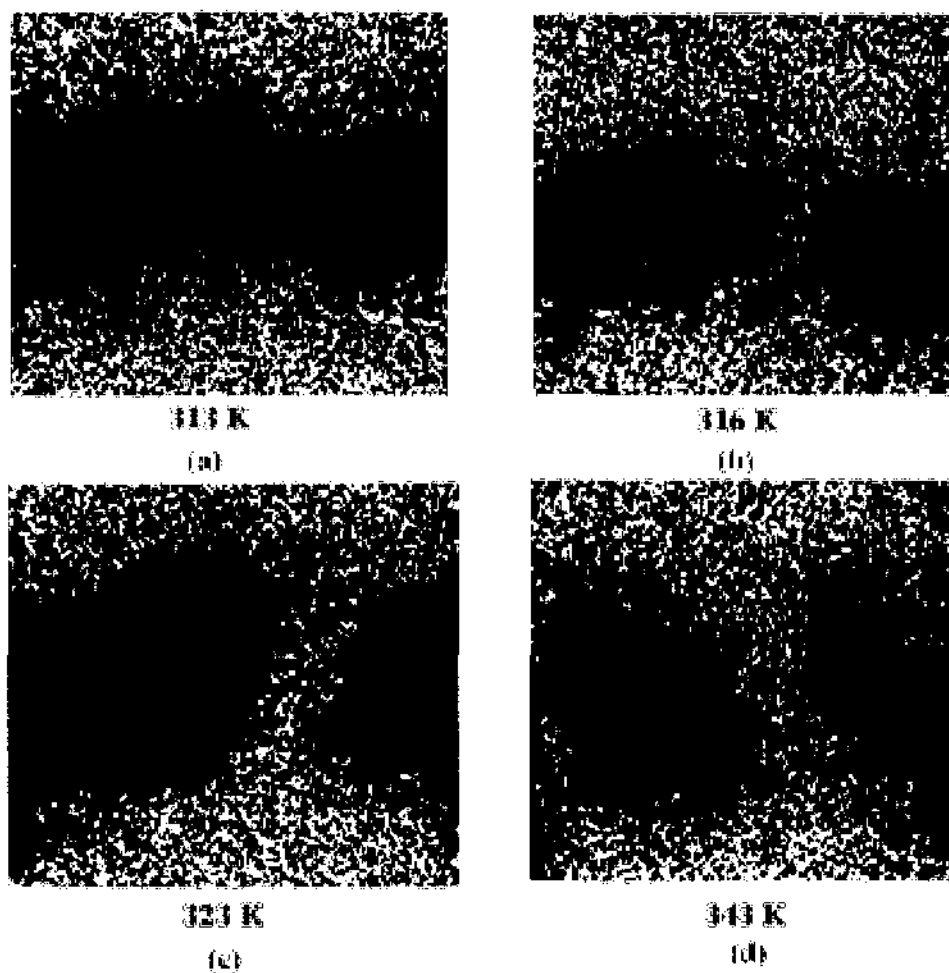


**Figure 21. MD results showing nano-pore formation at membrane by an external 1 V/nm, 1 ns pulsed electric field at different temperatures. Water is red and white.**

Figure 21(a) shows a snapshot of the water molecular arrangement after commencement of the external 1 V/nm, 1 ns pulse at 313 K. The water molecules are almost entirely on the outside (upper and lower). The snapshot at temperature 316 K shown in Figure 21(b) reveals a slight intrusion of a few water molecules. At temperature 323 K, a small nano-sized pore was seen to form as shown in Figure 21(c). Finally, Figure 21(d) shows a well-defined aqueous pore in the middle of the membrane. From

the MD results, we predict that nano-pores in biological membranes can form in response to a high external electric field within 1 ns at a higher temperature. In fact, increased temperatures facilitate pore formation. Hence, pre-heating cells or biological tissue might be advantageous from the standpoint of pore formation.

### **4.3 Simulation Results of High-Intensity Electric Pulse Induced Action Potential**

#### **Block**

The concept of cell electroporation was applied to gauge possible inhibitory effects in neuron signaling. Calculations for poration yielded pore densities and were used to compute conductivity changes at membranes. These changes in membrane conductivity were useful in predicting changes in action potential (AP) transmission, which basically is the electrical signal transmission in nerves.

The distributed electrical model incorporated an additional time-dependent membrane conductance  $G_{sh}$  to account for the poration induced by the high-intensity short-duration electric pulsing. Thus, the equivalent circuit had this additional conductance  $G_{sh}$  in parallel to the ionic channels. This modified equivalent circuit was used to simulate action potential propagation for various values of  $G_{sh}$  to assess the possibility of neural traffic blockage. For self-consistent calculations of AP blockage, the results of pore densities were used to obtain changes in  $G_{sh}$  by using equation (3.2.9). Results of Table 3 [43] give the maximum conductance  $G_{sh}$  computed at 100 mV for different field amplitudes and pulse durations of the excitation. In all cases, AP blockage was achieved.

A plot of the minimum pulse widths for several electrical pulse amplitudes, with the unmyelinated axon diameter as a parameter, obtained from self-consistent electroporation

calculations, is shown in Figure 22. Such self-consistent calculations of the shunt conductance were carried out taking account of electrical pulse initiated membrane pore generation based on a continuum Smoluchowski treatment. This effectively generates a “strength-duration (SD)” curve for AP blockage and would be a very useful design guide for benchmarking safety thresholds or setting the pulse voltage and/or durations necessary for neuro-muscular incapacitation. Electric field amplitudes monotonically increase with decreasing pulse duration. Also, for very short durations, the prediction is for inordinately large electric fields. From a practical standpoint, these values would be difficult to attain since localized breakdown and/or plasma creation might result under such circumstances. Hence, a natural and fundamental limit to ultrashort pulsing is clearly indicated. A second feature of Figure 22 is the relatively small variation with diameter. For longer pulses (400 ns and larger), the requisite electric fields for a conduction block are somewhat larger for a lower diameter nerve. This is simply because a lower diameter translates into a smaller surface area of the neural pipe. Hence, once a pore forms, there is a relatively lower fraction of surface area left for new pore formation in a smaller diameter nerve.

It is perhaps germane to discuss the effective duration of the AP conduction blockage [43]. As long as the pores do not reseal, or shrink considerably in size and density, the neural traffic can be blocked at a nerve. Since resealing times are on the order of seconds or longer, electrical pulse pulsing with a 1-2-Hz repetition rate would be sufficient to achieve blockage without any heating-related tissue damage or self-activated AP launches.

**Table III. Maximum conductance  $G_{sh}$  computed at 100 mV for different field amplitudes and pulse durations of the electroporating excitation [43].**

Maximum amplitude (kV/cm)	Pulse duration (ns)	Conductance (S)	AP Block ?
100.0	20.0	$3.0777 \times 10^{-4}$	Yes
100.0	50.0	$3.8265 \times 10^{-4}$	Yes
100.0	100.0	$4.3744 \times 10^{-4}$	Yes
150.0	20.0	$5.9528 \times 10^{-4}$	Yes
150.0	50.0	$7.0608 \times 10^{-4}$	Yes
150.0	100.0	$7.8385 \times 10^{-4}$	Yes
200.0	20.0	$7.7152 \times 10^{-4}$	Yes
200.0	50.0	$9.0424 \times 10^{-4}$	Yes

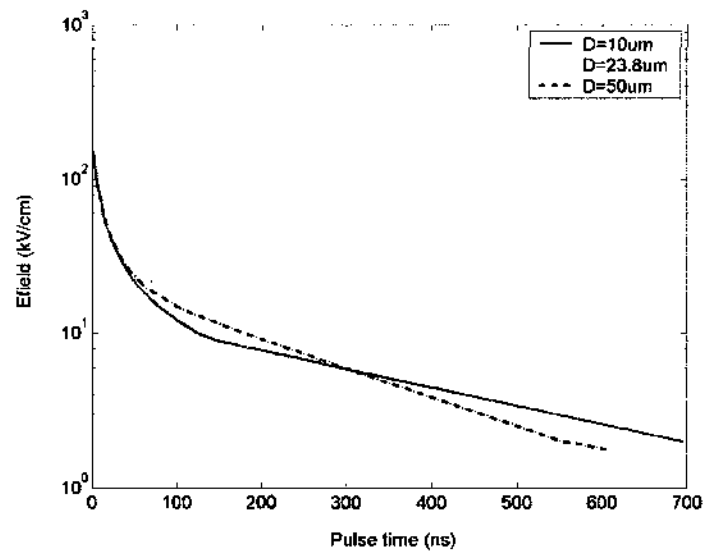


**Figure 22. Required electric field vs. pulse width to generate minimum shunt conductance required for AP block in nerve segments of different diameter.**

#### **4.4 Simulation Results of Pulse-Number Dependent Cellular Apoptosis and the Threshold Effect**

The role and extent of electric field modifications to the apoptotic pathways is unclear. Hard experimental data is lacking, in part due to the complexity of the biophysical mechanisms and the underlying competition between various processes. The model

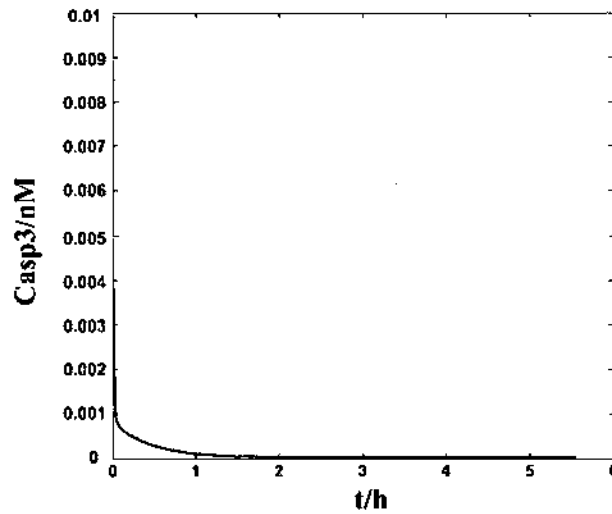


discussed in Chapter 3 was used to assess some of the processes and time-dependent dynamics of electrically induced apoptosis. The results and discussions follow.

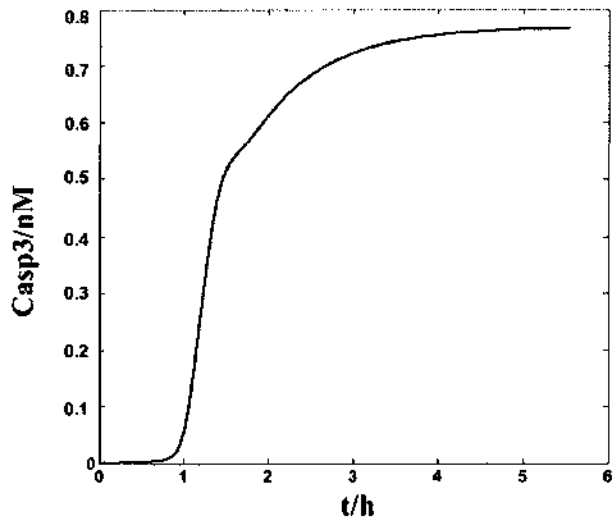
#### 4.4.1 Simulation Results

Calculation results are first presented for a single cell based on the above models. Later we provide results using an ensemble of 1000 cell-entities for more meaningful and realistic predictions of cell survival. Figures 23(a) and 23(b) show caspase-3 concentrations as a function of time starting from two different assumed levels of C8. At the lower  $10^{-5}$   $\mu\text{M}$  caspase-8 concentration, a decay in C3 over time is predicted; while increased values of C3 with time are seen in Figure 23(b) for the higher  $10^{-4}$   $\mu\text{M}$  caspase-8. These results are in keeping with the reported bi-stability of the apoptotic process and the requirement of a critical C8 level for inducing cell death. In these calculations, the C8 concentrations were assigned their initial values instantaneously at the start of the simulations. For the higher  $10^{-4}$   $\mu\text{M}$  caspase-8 concentration, appreciable C3 activation is predicted to occur roughly in the 1-2 hour time frame. This time scale is approximately in keeping with our preliminary experimental data (not shown, but is becoming available within our group) that gauges caspase activity and gathers other intracellular information using markers. For example, a cell permeable, fluorescent irreversible inhibitor of caspases is being utilized for caspase activity, while for DNA damage/repair an antibody to phosphorylated Histone 2AX is used, and data gathering for the mitochondrial membrane potential has been based on either JC-1 or tetramethylrhodamine ethyl ester (TMRE). This result suggests that if more C8 were to be activated (e.g., either a higher intensity pulse or through multiple pulsing), then the probable outcome for cell death might be enhanced. To gauge the response of C8 over time to multiple pulsing and

evaluate possible cumulative effects, simulations were next carried out with a low, but repetitive,  $4 \times 10^{-7}$   $\mu\text{M}$  caspase-8 injection. Simulation results for the time-dependent C3 concentration are shown in Figures 24(a) and 24(b) in response to 1 and 10 pulses (at 1 Hertz), respectively. The injections were taken to begin after 10,000 seconds ( $\sim 2.7$  hours) from the initial time. Clearly, the 10-pulse case points towards unstable cell behavior despite the low C8 injection as reflected through the C3 increase in Figure 24(b).



(a)



(b)

Figure 23. Single cell simulation results for the time-dependent C3 concentration. (a) Starting caspase-8 value of  $10^{-5}$   $\mu\text{M}$ , and (b) caspase-8 value of  $10^{-4}$   $\mu\text{M}$ .

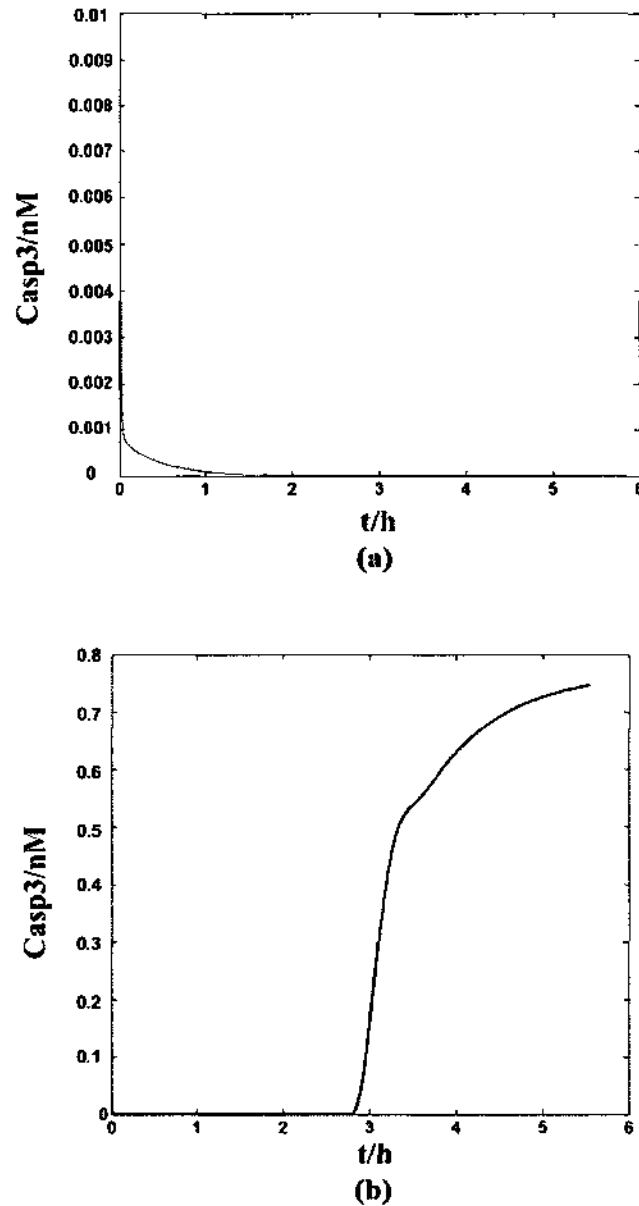


**Figure 24.** Time dependent changes in C3 concentration following a low level  $4 \times 10^{-7}$   $\mu\text{M}$  injection of C8 in a single cell. (a) A single injection assuming one electrical pulse, and (b) 10 injections at 1 Hertz.

The above calculations were based on instantaneous C8 release following a voltage pulsing event for a cell. However, as already mentioned, a sequence of processes are involved in the activation physics; hence, the C8 concentration should be taken to rise

gradually. Using the Bentele model [82], the normalized concentrations of caspase-8 and the blocked DISC states are shown in Figure 25. As expected, both increase over time. The characteristic time-delay is seen to be roughly 5 minutes. This is quite small compared to the much longer period, spanning hours, over which C3 activation and eventual cell death occurs. Hence, to a good approximation, bio-chemical triggering by an electric pulse can be taken to be very fast.

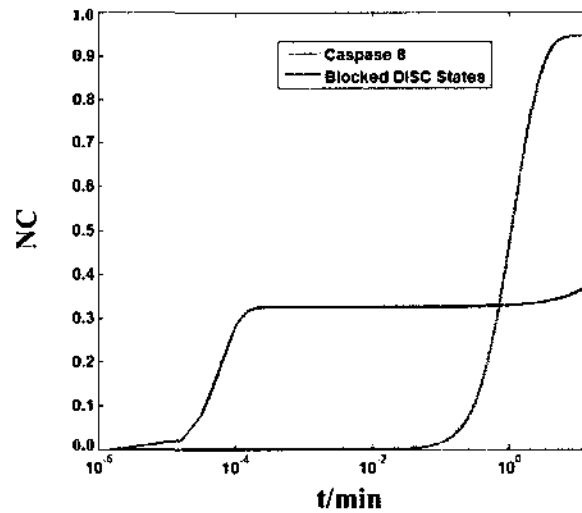


**Figure 25.** Single cell simulation results for the temporal evolution of the C8 and blocked DISC state concentrations.

Having discussed some aspects of single cell response, ensemble simulations were carried out next to include and mimic the statistical variability inherent in cell collections that are used in actual experiments. One thousand cells were used, and the C8 injection in each cell was randomly varied between zero and a maximum value  $C_{\max}$  by assigning random numbers. Predictions of cell survival versus pulse number for low level C8 injection (with  $C_{\max} = 4 \times 10^{-8} \mu\text{M}$ ) are shown in Figure 26. The injections, corresponding to the pulse numbers, were set at a frequency of 1 Hz in keeping with the experimental data of Pakhomov et al. [42]. Figure 26 clearly shows a threshold effect, and virtually all

cells are predicted to survive until about 50 pulses are incident on the cells. Beyond the threshold, a near-exponential fall off in survival is predicted, which is again in keeping with the nanosecond electric pulsing experiments. However, at the very large pulse numbers, a shift towards a slight saturating trend can be seen in Figure 26. Physically, this outcome arises from our choice of a fixed set of random numbers for each C8 injection at the 1 Hz frequency. In other words, those cells assigned a relatively high random number were always associated with higher C8 activation, leading to the most likely (and the fastest) outcome of cell death. The cumulative effort required for increasing C3 concentrations in the remaining cells increased as a result since these were always associated with much smaller random numbers. This is a likely scenario under *in vivo* conditions using an electrical setup that is fixed in location and orientation. One possibility for circumventing this effect and ensuring strong, continued cell killing might be to use multi-pronged or multi-electrode pulsing systems. Application of pulses via a multi-electrode system would offer changes in the field magnitude and local orientation, thereby ensuring greater activation from the pulsing over the entire population.

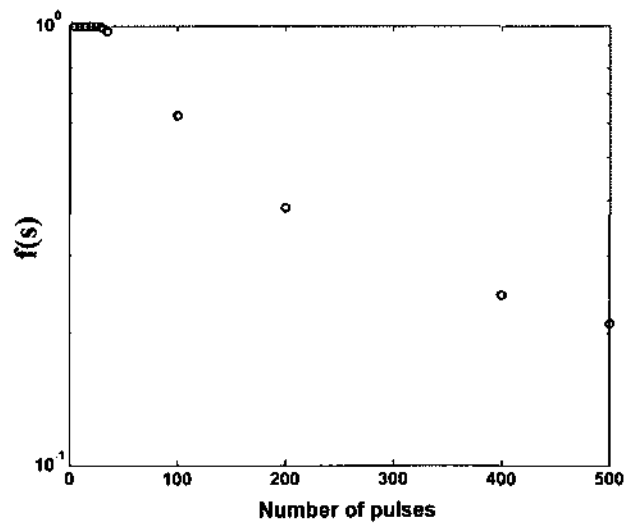
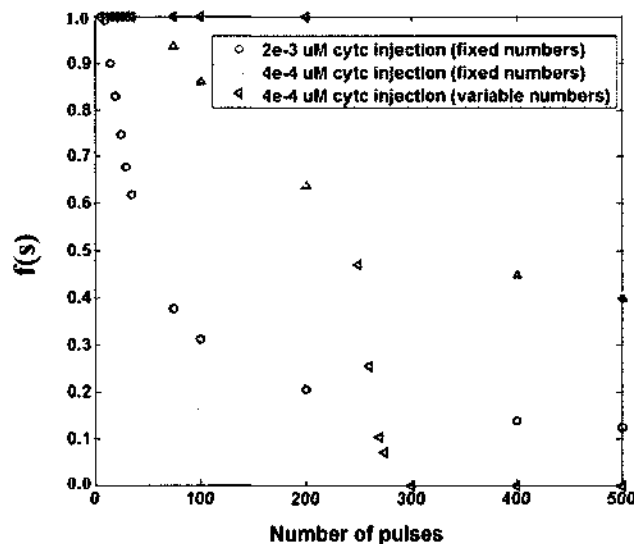


Figure 26. Predicted cell survival versus pulse number with 1000 cells.

In the above simulations, the extrinsic pathway was triggered by allowing for caspase-8 activation. Though the extrinsic pathway accommodates a role for mitochondria through the influence of truncated Bid and the p53 protein, the possibility for direct voltage-induced *cytochrome c* release is not incorporated. However, within the electric-pulsing context, it is postulated that the external voltage modulates the transmembrane potential, opening the mitochondrial permeability transition pore. Hence, an additional mechanism for apoptosis would be through voltage-induced *cytochrome c* release. It, therefore, becomes germane to evaluate the role of such *cytochrome c* release and gauge its relative importance with regards to the caspase-8 process. Towards that end, simulation runs were carried out to evaluate the pulse number dependence of cell survival starting only with the intrinsic process. Figure 27 shows simulation results for two different values ( $4 \times 10^{-4}$   $\mu\text{M}$  and  $2 \times 10^{-3}$   $\mu\text{M}$ ) of *cytochrome c* release. Furthermore, the effect of fixed-versus-random targeting of cells by the electric pulsing was probed through variations in the random number assignment in the algorithm. In two of the three cases shown, fixed random numbers were assigned to the level of *cytochrome c* release from each cell following every pulse. In the third curve of Figure 27, a variable random number assignment to cellular *cytochrome c* release was used. All the plots of Figure 27 in a general sense exhibit similar trends, with a threshold followed by an exponential fall-off that gradually reaches a saturating trend. Comparing the two curves obtained using fixed random numbers, a lower threshold is associated with the higher  $2 \times 10^{-3}$   $\mu\text{M}$  *cytochrome c* release and fall-off is faster, as might be expected. The lower  $4 \times 10^{-4}$   $\mu\text{M}$  concentration is predicted to have a significantly reduced cell killing effect. Between the fixed- and variable-random number cases, a smaller threshold is predicted with fixed

random numbers, but the survival fall-off is slower. Physically, this is to be expected since those cells that are randomly chosen to have larger *cytochrome c* release undergo a higher and faster caspase-3 elevation; while the others with low random number assignments continue to survive. The important point arising from these simulations, though, is that in comparison to caspase-8 activation, significantly higher levels of *cytochrome c* release seem to be necessary for cell killing. Thus, this intrinsic pathway is much weaker as compared to the extrinsic mechanism, at least in these simulations. This inference is qualitatively in keeping with some of the experimental data emerging from our experiments on cells with the nanosecond pulsing.



**Figure 27.** Cell survival versus pulse number predicted for two different values of *cytochrome c* release.

More direct comparisons of the relative role of *cytochrome c* and the timing under various conditions are shown in Figure 28. This single pulse simulation result for cellular caspase-3 with time used  $2 \times 10^{-2}$   $\mu\text{M}$  *cytochrome c* release and a C8 activation set at  $4 \times 10^{-6}$   $\mu\text{M}$ . In the simulations, these injections were taken to occur 10,000 seconds ( $\sim 2.7$

hours) after the initial time. A number of interesting features can be deduced from the results of Figure 28. As before, the extrinsic pathway can be seen to have a much stronger role and influence on inducing cellular apoptosis. It is also much faster and caspase-3 is predicted to be elevated in about 1 hour following an electrical pulsing event. Experimentally, caspase markers should detect such C3 elevation.

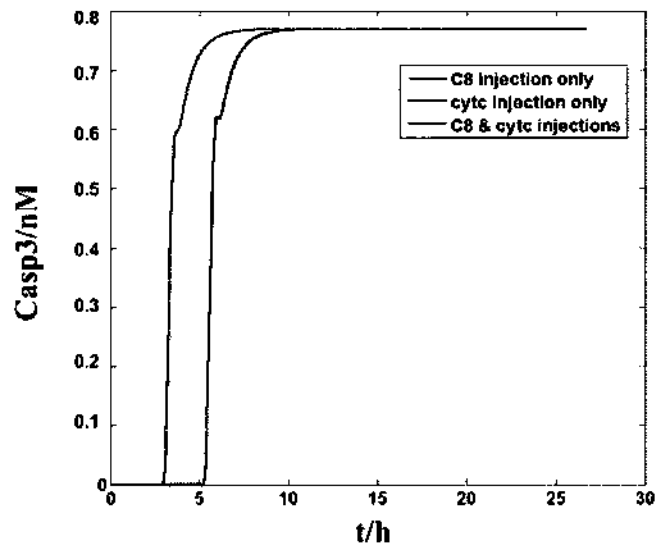


**Figure 28.** C3 versus time from single cell simulations under various conditions of C8 activation and cytochrome *c* release.

#### 4.4.2 Discussion

In the above analysis, an attempt has been made to probe and quantify the experimentally observed pulse number dependent cell survival trends on the basis of a biophysical model of apoptotic processes. Additionally, a relative assessment between extrinsic and intrinsic pathways and rough predictions of the time duration over which irreversible activation at the molecular level might be initiated have been carried out. A feature of this rate-equation modeling is the predicted delay in molecular concentration increases that could be on the order of an hour or more. This delayed bio-chemical



process in response to ultrashort electrical pulsing is similar to a recent report on cellular dye uptake upon electric pulsing [81]. The experiments by Kennedy et al. [81] identified two distinctive electroporative uptake signatures: an initial almost negligible dye absorption immediately after the pulse exposure followed by a high-level, accelerating uptake at much longer times.

It must be emphasized that the bio-physics of the overall process is quite complex and many issues remain unanswered. For example, the electric pulsing can be expected to trigger and influence a wide numbers of processes, not limited simply to caspase-8 activation, regulation of the mitochondrial trans-membrane potential, or even electroporation. These would include, for example, induced electron transfers between molecules leading to possible dissociation or conformational changes, facilitation of oxidation-reduction (redox) reactions and influence on their rate kinetics, alterations of membrane pumps [93], or calcium release from the endoplasmic reticulum [94]. Hence, the primary electrical event could lead to several downstream bio-chemical modifications, initiation of inter-dependent pathways, and interplay between multiple processes.

A number of aspects were ignored in our simple treatment. For example, it was assumed in the simulations that a chosen amount of *cytochrome c* release would result from each electrical pulsing. This assumes that the *cytochrome c* outflow is roughly similar to field-induced calcium release [94] and that its concentration within the mitochondria is large enough to discount depletion effects. Similarly, it was assumed that in the multiple pulsing scenario, the continued presence of strong external fields would not alter the rates and that the reaction kinetics would continue to follow the parameters of the Bagci model. In theory, other effects, such as electroporation, can also be expected

to change the dynamics of the apoptotic pathway. For example, upon pore creation, the lipid molecules which are in a state of constant flux could begin to diffuse through an effective “membrane sink-hole”. An example of such pore-facilitated lipid molecular diffusion is phosphatidylserine externalization that has been observed [95-96] and also modeled using Molecular Dynamics [88, 97]. Quite conceivably, the diffusion and transport of the lipid molecules in the localized vicinity of electropores would tend to increase molecular proximity, thereby enhancing mutual interactions. Hence, the dimerization and clustering processes that are found to initiate procaspase-8 cleavage and turn-on the extrinsic pathway might be augmented. The role of Reactive Oxygen Species (ROS) generation by the electric pulsing has also been ignored in the present treatment. However, reports in the literature [98] suggest that application of electric fields could elevate ROS. This, in turn, would alter apoptotic destruction through the ROS-mediated pathways involving oxidative stress [99-100]. For example, ROS is known to induce dissociation of *cytochrome c* from cardiolipin on the inner mitochondrial membrane and its release via mitochondrial permeability transition-dependent mechanisms. Last but not least, our numerical implementation of the simple multiple-pulsing scenario assumed a fixed amount of caspase-8 activation repeatedly in response to the external pulsing. Quite conceivably though, there could be a depletion effect, and the CD95 initiated process might not produce as much C8 after multiple pulses due to depletion. Physically, though, our implementation treats the activation as being triggered from discrete sites at the plasma membrane. A multitude of such sites would then alleviate the depletion issue and provide an electrically-induced effect after each electrical shot. This hypothesis of multi-targets and sites would be in keeping with the observed enhancements in cellular

apoptotic killing and gene delivery through multi-electrode systems [101]. Conceivably, the multi-electrode systems provide sufficiently high electric fields at different locations and orientations within cells for greater bio-effects.

#### **4.5 Simulation Results of the Asymmetric Electroporation Model**

An interesting recent report in the context of plasma membrane poration by nanosecond-duration electric pulsing, has been the observation of voltage-sensitive and inward-rectifying membrane nanopores [142]. These nanopores were seen to be relatively stable for many minutes and significantly impacted the balance of cell electrolytes and water. The formation of nanopores and their extended lifetime were verified by non-electrophysiological methods, namely by fluorescent detection of cell uptake of small inorganic cations. For example, the cells were loaded with a  $Tl^+$ -sensitive fluorophore, and  $Tl^+$  uptake was used as a marker for nanoporation. It was conjectured that their nonlinear current-voltage (I-V) characteristics might be the result of an asymmetrical pore cross-section. This explanation was invoked on the basis of the striking similarity to the reported I-V response of synthetic nanopores that had deliberately been fabricated to have conical shapes [50, 61]. Although plausible, no firm quantitative assessments or reasons behind the formation of such non-cylindrical nanopore shapes were presented or discussed. In the following, the possible existence of asymmetric pores that could lead to inward membrane rectification is discussed.

##### **4.5.1 Simulation Results for Electrostatic Pore Energy**

Figure 29 shows the electrostatic pore energies for a cylindrical pore, a symmetric toroidal pore and asymmetric toroidal pores. The curves correspond to the different value of the ratios of the pore diameters at the top and bottom, respectively. Thus, a perfectly

toroidal pore would have equal diameters at the top and bottom, leading to “ $f = 1$ ” as the factor. It is clear that electric pulsing favors pore formation because of the negative energy. In fact, if the electric pulse is left on, pores are predicted to grow until catastrophic cell rupture. The figure also shows that a cylindrical pore is the least favored energetically while asymmetric toroidal pores are more favored energetically. Another feature of Figure 29 is when  $f = 0$  has the lowest energy, but corresponds to either the bottom radius ( $b_B$ ) being zero or the top radius ( $b_T$ ) being zero. Physically, however, because of the presence of an inner cytoskeleton, asymmetric pores with  $b_B$  nearly zero are most likely to form.

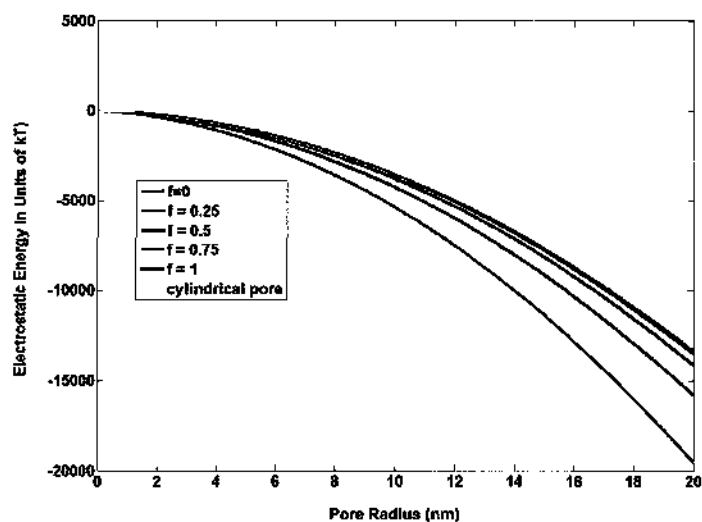
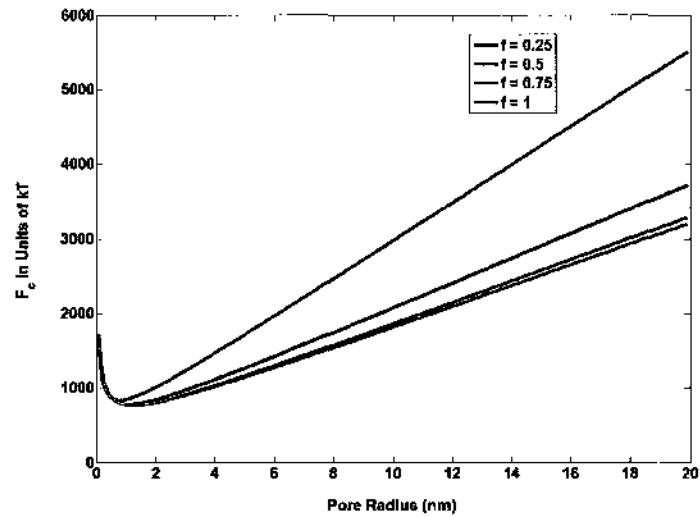
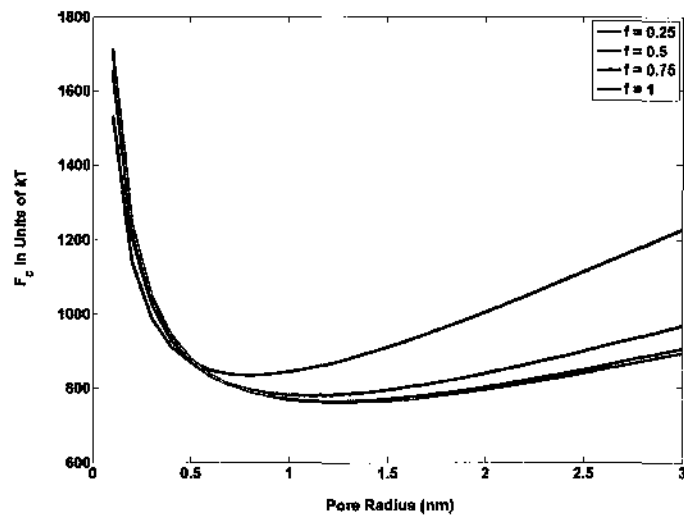


Figure 29. Electrostatic pore energy versus pore radius for different shapes of electropores.

### 4.5.2 Simulation Results for Mechanical Pore Energy



(a)



(b)

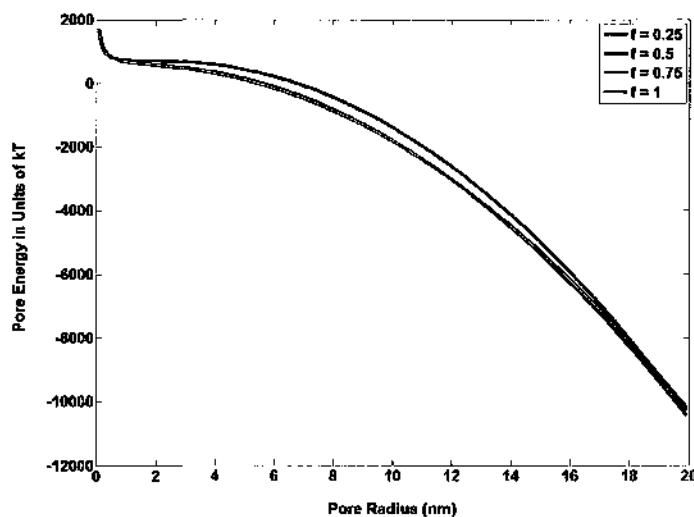
Figure 30. Mechanical pore energy versus pore radius. (b) Expanded plot.

Figure 30 shows mechanical pore energy for a symmetric toroidal pore and asymmetric toroidal pores. The results are opposite to those of electric pulsing induced

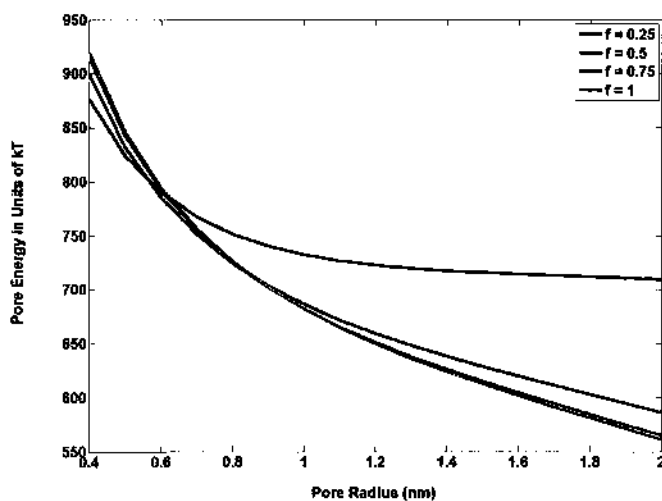
pores. Without pulsing, a symmetric pore is favored, and a minimum or stable pore radius occurs at about 0.8~1.0 nm.

#### 4.5.3 Simulation Results for Total Pore Energy

Simulation results for total pore energy are shown in Figure 31. With electric pulsing, pores are predicted to form, but asymmetric or symmetric shape depends on pore radius; smaller pores are asymmetric, while larger pores are symmetric.



(a)



(b)

Figure 31. (a) Total pore energy versus pore radius. (b) Expanded plot.

#### 4.5.4 Pore Dynamics and Closure

We already discussed pore formation energy and both electrical and mechanical contributions to the pore energy that governs poration. A pore forms with certain radius and membrane thickness within electric pulsing. Figure 32 shows the “total energy surface” as a function of pore radius and membrane thickness when pulsing is off for a symmetric pore.

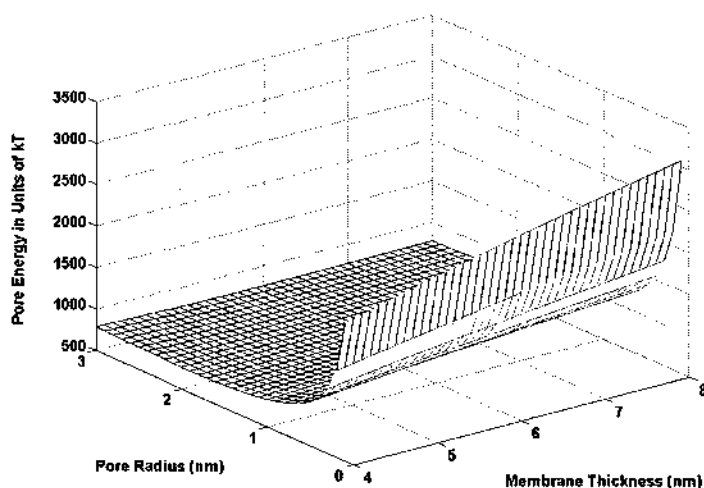


**Figure 32. Total pore energy surface**

After the electric pulsing is off, only mechanical energy contributes to the pore energy. In the following, the simulation provides some quantitative measure of the pore closing times. This is an important aspect for “drug-delivery,” since it determines the inflow and flux rates for molecules into cells.

Time dependent kinetics of the pore closure were simulated using the rate equation model proposed by Chizmadzhev et al. [108]:

$$\frac{dr}{dt} = -\frac{Dr}{kT} \frac{\partial E}{\partial r}, \quad (4.5.1)$$

$$\frac{db}{dt} = -\frac{D_b}{kT} \frac{\partial E}{\partial b}, \quad (4.5.2)$$

where  $r$  is the pore radius,  $b$  the membrane thickness, and  $D_r$  and  $D_b$  are the diffusion coefficients for the variables  $r$  and  $b$ , respectively. We assume both  $D_r$  and  $D_b$  are constants [109-110].  $E$  is the mechanical energy in equation (3.4.8).

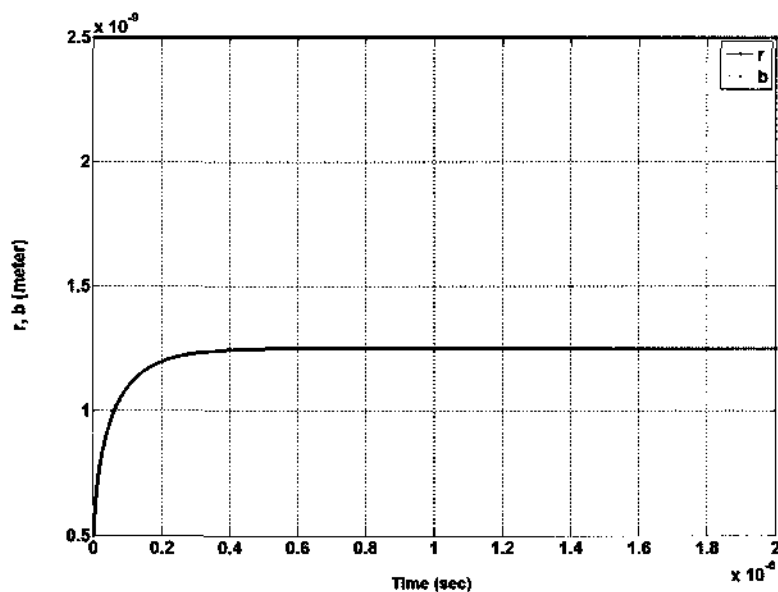


Figure 33. Simulation results for pore closure time.

Figure 33 shows the simulation results with  $b_{\text{initial}} = 2.5 \text{ nm}$ ,  $r_{\text{initial}} = 0.5 \text{ nm}$ . The pores reach steady state after  $0.6 \text{ us}$  at about  $1.25 \text{ nm}$ .



## CHAPTER V

### CONCLUSIONS AND FUTURE RESEARCH

#### 5.1 Research Summary

Traditionally, external voltage effects on biological cells have focused on probing electroporation with pulse durations in the microsecond range or higher. Here analysis for the cellular membrane response to nanosecond pulsing at electric fields as high as 500 kV/cm has been presented. It is argued that the conventional model of pore formation based on the continuum Smoluchowski equation needs to be modified by dynamic membrane tension term. Such variable tension is more physical and has been shown to correct for the high pore density predictions of the conventional model. Also, molecular dynamics results including temperature effects are discussed in this study.

This study showed that high-intensity, short-duration electrical pulses could provide for a quick-acting, localized, and reversible cessation of biological electrical signaling pathways. This would have obvious applications in neurophysiology, clinical research, neuromuscular stimulation therapies, and even nonlethal bio-weapons development. The concept of arresting action potential propagation is based on creating a large density of electro-pores on the membrane of unmyelinated nerves. A self-consistent theoretical approach based on the Smoluchowski equation has been used to assess membrane electroporation by a high-intensity external pulse. It has been shown that a high-intensity, nanosecond electric pulse can generate a high density of pores. The resulting change in membrane conductance then presents an effective “electrical short” to an incident voltage wave traveling across the nerve. Thus, the local membrane potential at the affected node

is unable to rise significantly, which prevents current injection and activation of sodium channels downstream, thereby blocking AP propagation. It is predicted that poration at a single neural segment would be sufficient to produce an observable effect. Furthermore, an effective “strength-duration (SD)” curve, detailing the pulse duration necessary for attaining the requisite membrane shunt conductance for a given field amplitude was generated.

Also, in this study, a simple model based rate equation treatment of the various cellular bio-chemical processes was used to predict the pulse number dependent cell survival trends. The bistable model incorporated the caspase-8 associated extrinsic pathway, the delay inherent in its activation, *cytochrome c* release, and the internal feedback mechanism between caspase-3 and Bid. Time-dependent evolution of the caspase concentrations and the various molecular species including caspase-3, Bid, t-Bid, Apoptosome, *cytochrome c* were simulated. Results obtained were roughly in keeping with the experimental cell-survival data. In particular, a pulse number threshold was predicted followed by a near-exponential fall-off. Also, the intrinsic pathway was shown to be much weaker as compared to the extrinsic mechanism for electric pulse induced cell apoptosis. Furthermore, since cell killing depended on the amounts of caspase-8 activation and *cytochrome c* released, differing survival thresholds are to be expected between different cell types. For instance, previous experimental reports on electric pulsing of cells showed a relative lack of PS externalization in B16 cells, whereas Jurkat cells showed strong PS effects [65]. Our PS observation postulated various factors such as a more stable plasma membrane and higher energies required for electroporation and molecular transport across the internal energy landscape. Quite conceivably, then, since

DISC formation and molecular clustering is required for the ultimate cleavage of procaspase-8, one can expect B16 cells to have a lower degree of caspase-8 activation and, hence, cell death. This has been confirmed in some experiments, and Jurkats have been shown to be more susceptible to electric pulse killing. Other factors such as electric field assisted suppression of c-FLIP binding could also play a role in the overall dynamics but is difficult to model. Finally, it must be mentioned that the predicted variability associated with random number assignments suggests that multi-electrode systems with adjustable field orientations would likely reinforce cell apoptosis.

Finally, an asymmetric electroporation model was discussed. With only electrostatic pore energy, a cylindrical pore is the least favored energetically while asymmetric toroidal pores are more favored energetically. When electric pulses are off, a symmetric pore is favored, and a minimum (or stable) pore radius occurs at about 0.8~1.0 nm. With electric pulsing, asymmetric or symmetric shape depends on pore radius: smaller pores are asymmetric, while larger pores are symmetric. This should lead to asymmetric current throughput across the cell membrane following electroporation. Such asymmetric current-voltage data has recently been obtained at the Center for Bioelectrics (Norfolk, VA.). Finally, the simulations provided some quantitative measure of the pore closing times. This is an important aspect for “drug-delivery,” since it determines the inflow and flux rates for molecules into cells.

## **5.2 Future Work**

More modeling and simulation work can be carried out to probe the inherent biophysics in cell membranes due to the application of the ultrashort, high-intensity electric pulses. For simplicity and proof of principle demonstration, single-pulsing will be

generally used, unless otherwise necessary. Besides probing the field-induced effects and their quantification, a secondary objective would be to focus on experimental data as available for direct comparisons.

Some of the other areas of future research include the following aspects:

(i) Conduct MD simulations of single pulses on proteins and ion-channels embedded in bilayer membranes. The Alamethicin channel is one candidate protein that will be tested because of its relatively simple structure and available molecular details.

(ii) Conduct MD calculations of transmembrane voltages and electric fields for a given set of molecular structure and arrangement in the absence and presence of external pulsing. The situation in the absence of external pulsing would mimic the published results of Gurtovenko and Vattulainen [133] and serve as a validity check. The results with an external voltage pulse would be an extension of that report.

(iii) Develop simple models for ion-channels that facilitate the inclusion of external electric fields effects. The model would then be included in the distributed circuit approach to predict ion transport through membrane following high intensity electric pulsing.

(iv). Attempt kinetic-based simulations of simple ions and molecules through nanopores. The ions are relatively easy and have been studied on the basis of MD simulations. The extension of the work to molecules (e.g., PI or Trypan Blue) would have practical implications to electric field induced drug delivery and introduction of chemical species into cells.

(v) Finally, extend some of the above tasks for multiple-pulsing scenarios. An important aspect in this context would be to gauge temperature changes, especially at the cell

membrane. Such temperature changes could alter the chemical kinetics and reaction rates of, for example, the release of caspase-8 at the membrane. For this an electro-thermal analysis would become necessary.

## References

- [1] S. J. Beebe, P. M. Fox, L. J. Rec, L. K. Willis, and K. H. Schoenbach, "Nanosecond, high intensity pulsed electric fields induce apoptosis in human cells," *FASEB J.*, vol. 17, pp.1493-1495, 2003.
- [2] J. Deng, K. H. Schoenbach, E. S. Buescher, P. S. Hair, P. M. Fox, and S. J. Beebe, "The effects of intense submicrosecond electrical pulses on cells," *Biophysical J.*, vol. 84, pp. 2709-2714, 2003.
- [3] S. J. Beebe, P. M. Fox, L. J. rec, K. Somers, R. H. Stark, and K. H. Schoenbach, "Nanosecond pulsed electric field (nsPEF) effects on cells and tissues: apoptosis induction and tumor growth inhibition," *IEEE Transactions on Plasma Science*, vol. 30, pp. 286-292, 2002.
- [4] G. A Hofmann, S. B. Dev , S. Dimmer, G. S. Nanda, *IEEE Transactions on Bio-Medical Engineering*, 46, 752, 1999.
- [5] W. R. Panje, and N. Sadeghi, "Endoscopic and electroporation therapy of paranasal sinus tumors," *Am. J. Rhinol.*, vol. 14, pp. 187-191, 2000.
- [6] P. H. Krammer, "CD95's deadly mission in the immune system", *Nature*, vol. 407, pp. 789-795, 2000.
- [7] H. R. Horvitz, "Genetic Control of Programmed Cell Death in the Nematode *Caenorhabditis elegans*," *Cancer Research (Suppl.)*, vol. 59, pp. 1701-1706, 1999.
- [8] M. D. Jacobson, M. Weil, and M. C. Raff, "Programmed cell death in animal development," *Cell*, vol. 88, pp. 347-354, 1997.

- [9] S. Sixou and J. Teissie, "Specific electroporabilization of leucocytes in a bold sample and application to large volume samples," *Biochem. Biophys. Acta.*, vol. 1028, pp. 154-160, 1990.
- [10] K. Hughes and N. Crawford, "Reversible electroporabilization of human and rat blood platelets: Evaluation of morphological and functional integrity in vitro and in vivo," *Biochem. Biophys. Acta.*, vol. 981, pp. 277-287, 1989.
- [11] L. F. Jaffe and R. Nuccitelli, "Electrical controls of development," *Annu. Rev. Biophys. Bioeng.*, vol. 38, pp. 445-476, 1977.
- [12] R.B. Borgens, "Electrically mediated regeneration and guidance of adult mammalian spinal axons into polymeric channels," *Neurosci.*, vol. 91, pp. 251-264, 1999.
- [13] S. Wang, J. Chen, M. T.Chen, P. T.Vernier, and M.A. Gundersen, "Cardiac myocyte excitation by ultrashort high-field pulses," *Biophys. J.*, vol. 96, pp. 1640-1648, 2009.
- [14] A. M. Rajnicek, L. E. Foubister, and C. D. McCaig, "Alignment of corneal and lens epithelial cells by co-operative effects of substratum topograph and DC electric fields," *Biomaterials*, vol. 29, pp. 2082-2095, 2008.
- [15] R. Bischoff, "Human hybridoma cells produced by electro-fusion," *FEBS Lett.*, vol. 147, pp. 64-68, 1982.
- [16] E. Neumann, M. Schaefer-Ridder, Y. Wang, and P. H. Hofschneider, "Gene transfer into mouse lyoma cells by electroporation in high electric fields," *EMBO J.*, vol. 1, pp. 841-845, 1982.

- [17] A. Daud, R. C. DeConti, S. Andrews, P. Urbas, A. Riker, V. K. Sondak, P. N. Munster, D. M. Sullivan, K. E. Ugen, J. L. Messina, and R. Heller, "Phase I trial of Interlukin-12 plasmid electroporation in patients with metastatic melanoma," *J. Clin. Oncol.*, vol. 26, pp. 5896-5903, 2008.
- [18] L. Mir, "Nucleic acids electrotransfer-based gene therapy: Past, present and future," vol.43, pp. 167-176, 2009.
- [19] R. Nuccitelli, X. Chen, A. G. Pakhomov, W. H. Baldwin, S. Sheikh, J. L. Pomicter, W. Ren, C. Osgood, J. F. Kolb, S. J. Beebe, and K. H. Schoenbach, "A new pulsed electric field therapy for melanoma disrupts the tumor's blood supply and causes remission without recurrence," *Int. Journ. Cancer*, vol. 125, pp. 438-445, 2009.
- [20] E. B. Garon, D. Sawcer, P. T. Vernier, T. Tng, Y. Sun, L. Marcu, M. A. Gundersen, and H. P. Koeffler, "*In vitro* and *in vivo* evaluation and a case report of intense nanosecond pulsed electric field as a local therapy for human malignancies," *Int. J. Cancer*, vol. 121, pp. 675-682, 2007.
- [21] L. M. Mir, S. Orłowski, J. Belehradec, M. P. Rols, G. Sersa, D. Miklavcic, R. Gilbert, and R. Heller, "Biomedical applications of electric pulses with special emphasis on antitumor electrochemotherapy," *Bioelectrochem. Bioenerg.*, vol. 38, pp. 203-207, 1995.
- [22] J. Teissie, N. Eynard, B. Gabriel, and M. P. Rols, "Electroporation of cell membranes," *Adv. Drug Delivery Rev.*, vol. 35, pp. 3-19, 1999.
- [23] E. Neumann, S. Kakorin, and K. Toensig, "Fundamentals of electroporative delivery of drugs and genes," *Bioelectrochem. Bioenerg.*, vol. 48, pp. 3-16, 1999.



- [24] K. H. Schoenbach, S. J. Beebe, and E. S. Buescher, "Intracellular Effect of Ultrashort Electrical Pulses," *Bioelectromagnetics*, vol. 22, pp. 440-448, 2001.
- [25] R. P. Joshi, Q. Hu, R. Aly, K. H. Schoenbach, and H. P. Hjalmarson, "Self-consistent simulations of electroporation dynamics in biological cells subjected to ultrafast electrical pulses," *Phys. Rev. E*, vol. 64, pp. 1191301-1191313, 2001.
- [26] K. H. Schoenbach, R. P. Joshi, J. Kolb, N. Chen, M. Stacey, P. Blackmore, E. S. Buescher, and S. J. Beebe, "Ultrashort electrical pulses open a new gateway into biological cells," *Proc. IEEE*, vol. 92, pp. 1122-1137, 2004.
- [27] K. H. Schoenbach, R. P. Joshi, R. H. Stark, F. C. Dobbs, and S. J. Beebe, "Bacterial decontamination of liquids with pulsed electric fields," *IEEE Trans. Dielectrics & Electrical Insulation*, vol. 7, pp. 637-645, 2000.
- [28] A. J. H. Sale and W. A. Hamilton, "Effects of high electric fields on microorganisms: I. Killing of bacteria and yeasts," *Biochimica et Biophysica Acta.*, vol. 148, pp. 781-788, 1967.
- [29] R. Nuccitelli, U. Pliquett, X. Chen, W. Ford, R. J. Swanson, S. J. Beebe, J. F. Kolb, and K. H. Schoenbach, "Nanosecond pulsed electric fields cause melanomas to self-destruct," *Biochem. Biophys. Res. Comm.*, vol. 343, pp. 351-360, 2006.
- [30] A. G. Pakhomov, J. F. Kolb, J. A. White, R. P. Joshi, S. Xiao, and K. H. Schoenbach, "Long-lasting plasma membrane permeabilization in mammalian cells by nanosecond pulsed electric field (nsPEF)," *Bio-Electromagnetics Journal*, vol. 28, pp. 655-663, 2007.

- [31] U. Broggemann, E. C. Roux, J. Hannig, and C. Nicolau, "Low-oxygen-affinity red cells produced in a large-volume, continuous-flow electroporation system," *Transfusion*, vol. 35, pp. 478-486, 1995.
- [32] M. Zeira, M. P.-F., M. Tosi, Y. Mouneimne, J. Lazarte, L. Sneed, D. J. Volsky, and C. Nicolau, "Full-length CD4 electro-inserted in the erythrocyte membrane as a long-lived inhibitor of infection by human immunodeficiency virus," *Proc. Nat. Acad. Sci.*, vol. 88, pp. 4409-4413, 1991.
- [33] M. Okino and H. Mohri, "Effects of a high-voltage electrical impulse and an anticancer drug on in vivo growing tumors," *Jpn. J. Cancer Res.*, vol. 78, pp 1319-1321, 1987.
- [34] L. M. Mir, S. Orłowski Jr., J. Belehradec, and C. Paoletti, "In vivo potentiation of the bleomycin cytotoxicity by local electric pulses," *Eur. J. Cancer*, vol. 27, pp. 68-72, 1991.
- [35] M. Belehradec, C. Domenge, B. Luboinski, S. Orłowski, J. Belehradec Jr., and L. M. Mir, "Electrochemotherapy, a new antitumor treatment. First clinical phase I-II trial," *Cancer*, vol. 72, pp. 3694-3700, 1993.
- [36] R. Heller, M. Jaroszeski, L. F. Glass, J. L. Messina, D. P. Rapport, R. C. Deconti, N. A. Fenske, R. A. Gilbert, L. M Mir, and D. S. Reintgen, "Phase I/II trial for the treatment of cutaneous and subcutaneous tumors using electrochemotherapy," *Cancer*, vol. 77, pp. 964-971, 1996.
- [37] J. C. Weaver, "Electroporation of cells and tissues", *IEEE Trans. On Plasma Science*, vol. 28, No. 1, 2000.

- [38] R. P. Joshi, Q. Hu, K. H. Schoenbach, and S. J. Beebe, "Energy-landscape-model analysis for irreversibility and its pulse-width dependence in cells subjected to a high-intensity ultrashort electric pulse", *Physical review E* 69, 051901-7, 2004.
- [39] A. G. Pakhomov, A. Phinney, J. Ashmore, K. Walker, III, J. F. Kolb, S. Kono, K. H. Schoenbach, and M. R. Murphy, "Characterization of the cytotoxic effect of high- intensity, 10-ns duration electrical pulses," *IEEE Trans. Plasma Sci.*, vol. 32, pp. 1579-1586, 2004.
- [40] A. L. Garner, N. Chen, J. Yang, J. Kolb, R. J. Swanson, K. C. Loftin, S. J. Beebe, R. P. Joshi, and K. H. Schoenbach, "Time domain dielectric spectroscopy measurements of HL-60 cell suspensions after microsecond and nanosecond electrical pulses," *IEEE Trans. Plasma Sci.*, vol. 32, pp. 2073-2084, 2004.
- [41] K. H. Schoenbach, S. Xiao, R. P. Joshi, J. T. Camp, T. Heeren, J. F. Kolb, and S. J. Beebe, "The Effect of Intense Subnanosecond Electrical Pulses on Biological Cells," *IEEE Trans. Plasma Sci.*, vol. 36, pp. 414-422, 2008.
- [42] A. G. Pakhomov, K. Walker, J. F. Kolb, K. H. Schoenbach, B. Stuck, and M. R. Murphy, "The rules of cell survival after exposure to high-intensity, ultrashort electrical pulses", Abstracts of the 26th Annual Meeting of the Bioelectromagnetics Society, (June 21-24, 2004, Washington, DC), 2004, pp. 7-8.
- [43] R. P. Joshi, A. Mishra, Q. Hu, K. H. Schoenbach, and A. Pakhomov, "Self-consistent analyses for potential conduction block in nerves by an ultrashort high-intensity electric pulse," *Phys. Rev. E*, vol. 75, 061906, 2007.

- [44] R. P. Joshi, Q. Hu and K.H. Schoenbach, "Dynamical Modeling of Cellular Response to Short-Duration, High-Intensity Electric Fields," *IEEE Transactions on Dielectrics and Electrical Insulation*, Vol. 10, No. 5, pp. 778-787, Oct 2003.
- [45] R. P. Joshi, Q. Hu, and K. H. Schoenbach, "Modeling studies of cell response to ultrashort, high-intensity electric fields – implications for intracellular manipulation," *IEEE Transactions on Plasma Science*, Vol. 32, No. 4, pp. 1677-1686, Aug 2004.
- [46] J. G. Whitwam and C. Kidd, "The use of direct current to cause selective block of large fibers in peripheral nerves," *Br. J. Anaesth.*, vol. 47, pp. 1123 -1133, 1975.
- [47] M. Ishigooka, T. AHashimoto, I. Sassagawa, K. Izumiya, and T. Nakada, "Modulation of the urethral pressure by high-frequency block stimulus in dogs," *Eur. Urol.*, vol. 25, pp. 334-337, 1994.
- [48] S. J. Tsai, H. L. Lew, E. Date, and L. I. Bih, "Treatment of detrusorsphincter dyssynergia by pudendal nerve block in patients with spinal ccord injury," *Arch. Phys. Med. Rehabil.*, vol. 83, pp. 714-717, 2002.
- [49] A. L. Hodgkin and A. F. Huxley, "A quantitative description of the membrane current and its application to conduction and excitation in nerve," *J. Physiol. (London)*, vol. 117, pp. 500-544, 1952.
- [50] R. P. Joshi, A. Mishra, J. Song, A. Pakhomov, and K. H. Schoenbach, "Simulation studies of ultra-short, high-intensity electric pulse induced action potential block in whole-animal nerves," *IEEE Trans. Biomedical Engineering*, vol. 55, pp. 1391-1398, 2008.

- [51] K. C. Melikov, V. A. Frolov, A. Shcherbakov, A. V. Samsonov, Y. A. Chizmadzhev, and L. V. Chernomordik, "Voltage-induced nonconductive pre-pores and metastable single pores in unmodified planar lipid bilayer," *Biophys. J.*, vol. 80, pp. 1829-1836, 2001.
- [52] Q. Long and W. Xing, "Detection of the apoptosis of Jurkat cell using an electrorotation chip," *Front. Biol. China*, vol. 2, pp. 208-212, 2006.
- [53] Q. Long and W. Xing, "Detection of the apoptosis of Jurkat cell using an electrorotation chip," *Front. Biol. China*, vol. 2, pp. 208-212, 2006.
- [54] U. Zimmermann and G. A. Neil, *Electromanipulation of Cells*, CRC, Boca Raton, FL, 1996.
- [55] P. Bernardi and V. Petronilli, "The permeability transition pore as a mitochondrial calcium release channel: a critical appraisal," *J. Bioenerg. Biomembr.*, vol. 28, pp. 131-138, 1996.
- [56] F. Ichas and J. P. Mazat, "From calcium signaling to cell death: two conformations for the mitochondrial permeability transition pore. Switching from low- to high-conductance state," *Biochim. Biophys. Acta*, vol. 1366, pp. 33-50, 1998.
- [57] Y. X. Li and J. Rinzel, "Equations for  $\text{InsP}_3$  receptor-mediated  $[\text{Ca}]_i$  oscillations derived from a detailed kinetic model: Hodgkin-Huxley-like formalism," *J. Theor. Biol.*, vol. 166, pp. 461-473, 1994.
- [58] C. McBride, M. R. Wilson, and J. A. K. Howard, "Molecular dynamics simulations of liquid crystal phases using atomistic potentials" *Mol. Phys.*, vol. 93, pp. 955-964, 1998.

- [59] A. J. McDonald and S. Hanna, "Atomistic simulation of a model liquid crystal" *J. Chem. Phys.*, vol. 124, pp. 164906/1-11, 2006.
- [60] M. R. Wilson, "Molecular simulation of liquid crystals: progress towards a better understanding of bulk structure and the prediction of material properties," *Chem. Soc. Rev.*, vol. 36, pp. 1881-1888, 2007.
- [61] S. J. Beebe, P. F. Blackmore, J. White, R. P. Joshi, and K. H. Schoenbach, "Nanosecond pulsed electric fields modulate cell function through intracellular signal transduction mechanisms," *Physiol. Meas.*, vol. 25, pp. 1077-1093, 2004.
- [62] N. Chen, K. H. Schoenbach, J. F. Kolb, R. J. Swanson, A. L. Garner, J. Yang, R. P. Joshi, and S. J. Beebe, "Leukemic cell intracellular responses to nanosecond electric fields", *Biochem. Biophys. Res. Comm. (BBRC)*, vol. 317, pp. 421-427, 2004.
- [63] K. H. Schoenbach, B. Hargrave, R. P. Joshi, J. F. Kolb, R. Nuccitelli, C. Osgood, A. Pakhomov, M. Stacey, R. J. Swanson, J. White, S. Xiao, J. Zhang, S.J. Beebe, P. F. Blackmore, and E. S. Buescher, "Bioelectric effects of intense nanosecond pulses," *IEEE Trans. Dielectr. Electr. Insul.*, vol. 14, pp. 1088-1107, October 2007.
- [64] R. P. Joshi, Q. Hu, K. H. Schoenbach and H. P. Hjalmarson, "Improved energy model for membrane electroporation in biological cells subjected to electrical pulses," *Phys. Rev. E*, vol. 65, pp.041920/1-8, 2002.
- [65] H. Isambert, "Understanding the electroporation of cells and artificial bilayer membrane," *Phys. Rev. Lett.*, vol. 80, pp.3404-3407, 1998.
- [66] S. E. Feller and R. W. Pastor, "On simulating lipid bilayers with an applied surface tension: periodic boundary conditions and undulations," *Biophys. J.*, vol. 71, pp. 1350-1355, 1996.

- [67] Q. Hu, R. P. Joshi, and K. H. Schoenbach, "Simulations of nanopore formation and phosphatidylserine externalization in lipid membranes subjected to a high-intensity, ultrashort electric pulse," *Phys. Rev. E* 72, 031902, 2005.
- [68] J. W. Cooley and F. A. Dodge, Jr., "Digital computer solutions for excitation and propagation of the nerve impulse," *Biophys. J.*, vol. 6, pp.583-599, 1966.
- [69] D. R. McNeal, "Analysis of a model for excitation of myelinated nerve," *IEEE Trans. Biomed. Eng.*, vol. BME- 23, no. 4, pp. 329-337, Jul. 1976.
- [70] F. Rattay, "Analysis of models for external stimulation of axons," *IEEE Trans. Biomed. Eng.*, vol. BME-33, no. 10, pp. 974-977, Oct. 1986.
- [71] B. Frankenhaeuser and A. F. Huxley, "The action potential in the myelinated nerve fiber of *Xenopus Laevis* as computed on the basis of voltage clamp data," *J. Physiol. (London)*, vol. 171, pp. 302-315, 1964.
- [72] Douglas R. Green, "Apoptotic pathways: Paper wraps stone blunts scissors," *Cell*, vol. 102, pp. 1-4, 2000.
- [73] M. E. Peter and P. H.Krammer, "The CD95 death-inducing signaling complex and beyond," *Cell Death Differ.*, vol. 10, pp. 26-35, 2003.
- [74] K. C. Smith, T. R. Gowrishankar, A. T. Esser, D. A. Stewart, and J. C. Weaver, "The spatially distributed dynamic transmembrane voltage of cells and organelles due to 10 ns pulses: meshed transport networks," *IEEE Trans. Plasma Sci.*, vol. 34, pp. 1394-1404, 2006.
- [75] B. Brune, "Nitric oxide and apoptosis in mesangial cells," *Kidney Int.*, vol. 61, pp. 786-789, 2002.

- [76] I. Marzo, C. Brenner, N. Zamzami, J. M. Jürgensmeier, S. A. Susin, H. L. A. Vieira, M. C. Prévost, Z. Xie, S. Matsuyama, J. C. Reed, G. Kroemer, "Bax and adenine nucleotide translocator cooperate in the mitochondrial control of apoptosis," *Science*, vol. 281, pp. 2027–2031, 1998.
- [77] B. Antonsson, F. Conti, A. Ciavatta, S. Montessuit, S. Lewis, I. Martinou, L. Bernasconi, A. Bernard, J. J. Mermod, G. Mazzei, K. Maundrell, F. Gambale, R. Sadoul, and J. C. Martinou, "Inhibition of Bax channel-forming activity by Bcl-2," *Science*, vol. 277, pp.370-372, 1997.
- [78] E. Z. Bagci, Y. Vodovotz, T. R. Billiar, G. B. Ermentrout, and I. Bahar, "Bistability in apoptosis: Roles of Bax, Bcl-2, and mitochondrial permeability transition pores," *Biophys. J.*, vol. 90, pp. 1546-1559, 2006.
- [79] M. Zoratti and I. Szabo, "The mitochondrial permeability transition," *Biochim. Biophys. Acta*, vol. 1241, pp. 139–176, 1995.
- [80] M. Enari, H. Sakahira, H. Yokoyama, K. Okawa, A. Iwamatsu, and S. Nagata, "A caspase-activated dNase that degrades DNA during apoptosis, and its inhibitor ICAD," *Nature*, vol. 391, pp. 43-50, 1998.
- [81] S. M. Kennedy, Z. Ji, J. C. Hedstrom, J. H. Booske, and S. C. Hagness, "Quantification of electroporative uptake kinetics and electric field heterogeneity effects in cells," *Biophys. J.*, vol. 94, pp. 5018-5027, 2008.
- [82] M. Bentele, I. Lavrik, M. Ulrich, S. Stofier, D. W. Heennann, H. Kalthoff, P. H. Krammer, and R. Eils, "Mathematical modeling reveals threshold mechanism in CD95-induced apoptosis," *J. Cell Biol.*, vol. 166, pp. 839-851, 2004.



- [83] S. B. Debord and L. A. Lyon, "Influence of particle volume fraction on packing in responsive hydrogel colloidal crystals," *J. Phys. Chem. B*, vol. 107, No. 13, pp. 2927-2932, 2003.
- [84] J. C. Neu, K. C. Smith, w. Krassowska, "Electrical energy required to from large conducting pores," *Bioelectrochemistry* vol. 60, pp. 1-10, 2003.
- [85] M. W. Matsen, "Converting the nanodomains of a diblock-copolymer thin film from spheres to cylinders with an external electric field," *J. chem.. Phys.*, vol. 124, 074906/1-9, 2006.
- [86] S. A. Safran, *Statistical Thermodynamics of surface interfaces and membranes*, Addison-Wesley, Reading, MA, 1994.
- [87] H. Leontiadou, A. E. Mark, and S. -J. Marrink, "Molecular dynamics simulations of hydrophilic pores in lipid bilayers," *Biophys. J.*, vol. 86, pp. 2156-2164, 2004.
- [88] S. J. Marrink, E. Lindahl, O. Edholm, and A. E. Mark, "Simulation of the spontaneous aggregation of phospholipids into bilayers," *J. Am. Chem. Soc.*, vol. 123, pp. 8638-8639, 2001.
- [89] S. J. Marrink, and A. E. Mark, "Effect of undulations on surface tension in simulated bilayers," *J. Phys. Chem. B*, vol.105, pp. 6122-6127, 2001.
- [90] A. V. Titomirov, S. sukharev, and E. Kistoanova, "In vivo electroporation and stable transformation of skin cells of newborn mice by plasmid DNA," *Biochem. Biophys. Acta*, vol. 1088, pp. 131-134, 1991.
- [91] R. Heller, M. Jaroszeski, a. Atkin, D. Moradpour, R. gilbert, and J. W. C. Nicolau, "In vivo gene electroinjection and expression in rat liver," *FEBS Lett.*, vol. 389, pp. 225-228, 1996.

- [92] E. Tekle, R. D. Astumian, W. A. Friauf, and P. B. Chock, "Asymmetric pore distribution and loss of membrane lipid in electroporated DOPC vesicles," *Biophysical J.*, vol. 81, no.2, pp. 960-968, 2001.
- [93] D. Nawarathna, J. H. Miller, Jr., J. R. Claycomb, G. Cardenas, and D. Warmflash, "Harmonic Response of Cellular Membrane Pumps to Low Frequency Electric Fields," *Phys. Rev. Lett.*, vol. 95, pp. 158103/104, 2005.
- [94] R. P. Joshi, A. Nguyen, V. Sridhara, Q. Hu, R. Nuccitelli, and K. H. Schoenbach, "Simulations of Intra-Cellular Calcium Release Dynamics in Response to a High-Intensity, Ultra-Short Electric Pulse," *Phys. Rev. E*, vol. 75, pp. 041920/1-10, 2007.
- [95] P. T. Vernier, Y. Sun, L. Marcu, S. Salemi, C. M. Craft, and M. A. Gundersen, "Calcium bursts induced by nanosecond electric pulses," *Biochem. Biophys. Res. Commun.*, vol. 310, pp. 286-295, 2003.
- [96] J. A. White, P. F. Blackmore, K. H. Schoenbach, and S. J. Beebe, "Stimulation of capacitative calcium entry in HL-60 cells by nanosecond pulsed electric fields," *J. Biol. Chem.*, vol. 279, pp. 22964-22972, 2004.
- [97] P. T. Vernier, M. J. Ziegler, Y. Sun, W. V. Chang, M. A. Gundersen, and D. P. Tieleman, "Nanopore formation and phosphatidylserine externalization in a phospholipid bilayer at high transmembrane potential," *J. Am. Chem. Soc.*, Vol. 128, pp. 6288-6289, 2006.
- [98] M. Wartenberg, N. Wirtz, A. Grob, W. Niedermeier, J. Hescheler, S. C. Peters, H. Sauer, "Direct current electrical fields induce apoptosis in oral mucosa cancer cells by NADPH oxidase-derived reactive oxygen species," *Bioelectromagnetics*, vol. 29, pp. 47-54, 2008.

- [99] K. Kannan and S. K. Jain, "Oxidative stress and apoptosis," *Pathophysiology*, vol. 7, pp. 153–163, 2000.
- [100] N. Zamzami, T. Hirsch, B. Dallaporta, P. X. Petit, and G. Kroemer, "Mitochondrial implication in accidental and programmed cell death: apoptosis and necrosis," *J. Bioenerg. Biomembr.*, vol. 29, pp. 185–193, 1997.
- [101] M. J. Jaroszeskia, R. Gilbert, C. Nicolau, and R. Heller, "In vivo gene delivery by electroporation," *Advanced Drug Delivery Reviews*, vol. 35, pp. 131-137, 1999.
- [102] L. Zhang, L. Li, G. Hofmann, and R. M. Hoffman, "Depth-targeted efficient gene delivery and expression in the skin by pulsed electric fields: An approach to gene therapy of skin aging and other diseases," *Biochem. Biophys. Res. Commun.*, vol. 220, pp. 633-636, 1996.
- [103] T. Nishi, S. B. Dev, K. Yoshizato, J. Kuratsu, and Y. Ushio, "Treatment of cancer using pulsed electric field in combination with chemotherapeutic agents or genes," *Human Cell*, vol. 1, pp. 81-86, 1997.
- [104] M. P. Rols, C. Delteil, M. Golzio, P. Dumond, s. Cors, and J. teissie, "In vivo electrically mediated protein and gene transfer in murine melanoma," *Nature Biotechnol.*, vol. 16, pp. 168-171, 1998.
- [105] S. A. Freeman, M. A. Wang, and J. C. Weaver, "Theory of electroporation of planar bilayer membranes: predictions of the aqueous area, change in capacitance, and pore-pore separation," *Biophys. J.*, vol. 67, pp. 42-56, 1994.
- [106] R. W. Glaser, S. L. Leikin, L. V. Chernomordik, V. F. Pastushenko, and A. I. Sokirko, "Reversible electrical breakdown of lipid bilayers: formation and evolution of pores," *Biochim, Biophys, Acta*, vol. 940, pp. 275-287, 1988.

- [107] J. C. Weaver and R. A. Mintzer, "Decreased bilayer stability due to transmembrane potentials," *Phys. Lett*, vol. 86A, pp. 57-59, 1981.
- [108] Y. A. Chizmadzhev, F. S. Cohen, A. Shcherbakov, and J. Zimmerberg, "Membrane mechanics can account for fusion pore dilation in stages," *Biophys. J.*, vol 69, pp. 2489-2500, 1995.
- [109] B. V. Deryaguin, and Yu. V. Gutop, "The theory of the rupture of free films," *Kolloidniy J.*, vol 24, pp. 431-437, 1962.
- [110] R. Kubo, M. Toda, and N. Hashitsume, *Statistical Physics II*, 2<sup>nd</sup> ed. Springer-Verlag, Berlin, 1991.
- [111] M. Weller, "Predicting response to cancer chemotherapy: the role of p53," *Cell Tissue Res.*, vol. 292, pp. 435-445, 1998.
- [112] J. D. Litster, "Stability of lipid bilayers and red blood cell membranes," *Phys. Lett.*, vol. A53, pp. 193-194, 1975.
- [113] R. L. Harrison, B. J. Byrne, and L. Tung, "Electroporation-mediated gene transfer in cardiac tissue," *FEBS Lett.*, vol. 435, pp. 1-5, 1998.
- [114] R. Langer, "Drug delivery and targeting," *Nature*, vol. 392, pp. S5-S10, 1998.
- [115] J. C. Weaver, and Y. A. Chizmadzhev, "Theory of electroporation: A review," *Bioelectrochem. Bioenerg.*, vol. 41, pp. 135-160, 1996.
- [116] D. Kashchiev, "On the stability of membrane, foam and emulsion bilayers with respect to rupture by hole nucleation," *Colloid Polymer Sci.*, vol. 265, pp. 436-441, 1987.
- [117] M. Winterhalter, and W. Helfrich, "Effect of voltage on pores in membranes," *Phys. Rev.*, vol. A36, pp. 5874-5876, 1987.

- [118] J. Wohler, W. K. den Otter, O. Edholm, W. J. Briels, "Free energy of a transmembrane pore calculated from atomistic molecular dynamics simulations," *J. chem. Phys.*, vol. 124, pp. 154905-154912, 2006.
- [119] I. G. Abidor, V. B. arakelyan, L. V. Chernomordik, Y. A. Chizmadzhev, V. F. Pastushenko, M. R. Tarasevich, "Electric breakdown of bilayer lipid membranes: I. Main experimental facts and their qualitative discussion," *Bioelectrochem. Bioenerg.*, vol. 6, pp 37-52, 1979.
- [120] Y. Vodovotz, P. K. M. Kim, E. Z. Bagci, G. B. Ermentrout, C. C. Chow, I. Bahar, and T. R. Billiar, "Inflammatory modulation of hepatocyte apoptosis by nitric oxide: in vivo, invitro and in silico studies," *Curr. Mol. Med.*, vol. 4, pp. 753-762, 2004.
- [121] J. P. Reilly, V. T. Freeman, and W. D. Larkin, "Sensory effects of transient electrical stimulation – evaluation with a neuroelectric model," *IEEE Trans. Biomed. Eng.*, vol. 32, pp. 1001-1011, 1985.
- [122] P. H. Veltink, J. A. V. Alste, and H. B. K. Boom, "Influences of stimulation conditions on recruitment of myelinated nerve fibers: a model study," *IEEE Trans. Biomed. Eng.*, vol. 35, pp. 917-924, 1988.
- [123] K. W. Altman, and R. Plonsey, "Point source nerve bundle stimulation: effects of fiber diameter and depth on simulated excitation," *IEEE Trans. Biomed. Eng.* Vol. 37, pp. 688-698, 1990.
- [124] C. Tai, W. C. de Groat, and J. R. Roppolo, "Simulation analysis of conduction block in unmyelinated axons induced by high-frequency biphasic electrical currents," *IEEE Trans. Biomed. Eng.*, vol. 52, no. 7, pp. 1323-1332, 2005.

- [125] W. Meier, A. Graff, A. Diederich, and M. Winterhalter, "Stabilization of planar lipid membranes: a stratified layer approach," *Phys. Chem Phys.*, vol. 2, pp. 4559-4562, 2000.
- [126] J. C. Neu and W. Krassowska, "Asymptotic model of electroporation," *Phys. Rev. E*, vol. 59, pp. 3471-3482, 1999.
- [127] N. O. Karpnich, M. Tafani, R. J. Rothman, M. A. Russo, and J. L. Farber, "The course of etoposide-induced apoptosis from damage to DNA and p53 activation to mitochondrial release of *cytochrome c*," *J. Biol. Chem.*, vol. 277, pp. 16547-16552, 2002.
- [128] A. P. Halestrap, G. P. McStay, and S. J. Clarke, "The permeability transition pore complex: another view," *Biochimie*, vol. 84, pp. 153-166, 2002.
- [129] S. A. Susin, N. Zamzami, and G. Kroemer, "Mitochondria as regulators of apoptosis: doubt no more," *Biochem Biophys. Acta*, vol. 1366, pp. 151-165, 1998.
- [130] A. P. Halestrap, and C. Brenner, "The adenine nucleotide translocase: a central component of the mitochondrial permeability transition pore and key player in cell death," *Curr. Med. Chem.*, vol. 10, pp. 1507-1525, 2003.
- [131] M. Crompton, "The mitochondrial permeability transition pore and its role in cell death," *Biochem. J.*, vol. 341, pp. 233-239, 1999.
- [132] G. Kroemer, and J. C. Reed, "Mitochondrial control of cell death," *Nat. Med.*, vol. 6, pp. 513-519, 2000.
- [133] A. A. Gurtovenko and Ilpo Vattulainen, "Lipid transmembrane asymmetry and intrinsic membrane potential: two sides of the same coin," *J. Am. Chem. Soc.*, vol. 129, pp. 5358-5359, 2007.

- [134] R. V. Davalos, "Tissue ablation with irreversible electroporation," *Ann. Biomed. Eng.*, vol. 33, pp. 223-231, 2005; G. Onik, P. Mikus, and B. Rubinsky "Irreversible electroporation: implications for prostate ablation," *Technol. Cancer Res. Treat.*, vol. 6, pp. 295-300, 2007.
- [135] C. M. Care and D. J. Cleaver, "Computer Simulation of Liquid Crystals," *Rep. Prog. Phys.*, vol. 68, pp. 2665-2700, 2005.
- [136] S. Chandrasekhar, "Stochastic problems in physics and astronomy," *Rev. Mod. Phys.*, vol. 15, pp. 1-89, 1943.
- [137] S. Bose and P. Ortoleva, "A hard sphere model of chemical reaction in condensed media," *Phys. Lett. A*, vol. 69, pp. 367-369, 1979.
- [138] J. M. Deutch and I. Oppenheim, "The Concept of Brownian Motion in Modern Statistical Mechanics," *Faraday Discuss. Chem. Soc.*, vol. 83, pp. 1-20, 1987.
- [139] J. E. Shea and I. Oppenheim, "Fokker–Planck equation and Langevin equation for one Brownian particle in a nonequilibrium bath," *J. Phys. Chem.*, vol. 100, pp. 19035-19042, 1996.
- [140] J. E. Shea and I. Oppenheim, "Fokker–Planck equation and non-linear hydrodynamic equations of a system of several Brownian particles in a non-equilibrium bath," *Physica A*, vol. 247, pp. 417-443, 1997.
- [141] M. H. Peters, "Fokker-planck equation and the grand molecular friction tensor for coupled rotational and translational motions of structured Brownian particles near structured surfaces," *J. Chem. Phys.*, vol. 110, pp. 528-538, 1999.
- [142] A. G. Pakhomov, A. M. Bowman, B. L. Ibey, F. M. Andre, O. N. Pakhomova, and K. H. Schoenbach, "Lipid nanopores can form a stable, ion channel-like conduction

pathway in cell membrane," *Biochem. Biophys. Res. Comm.*, Vol. 385, pp. 181-186, 2009.



## VITA

for

Jiahui Song

**EDUCATION**

Ph. D. Electrical Engineering, Old Dominion University, Norfolk, VA  
M. S. Pattern Recognition & Intelligent Systems, Southeast University, Nanjing, China  
B. S. Automation, Southeast University, Nanjing, China

**SELECTED PUBLICATIONS**

R. P. Joshi, and J. Song, "Model Analysis of Electric Fields Induced by High-Voltage Pulsing in Cylindrical Nerves," accepted for publication, to appear *IEEE Transactions on Plasma Science*.

J. Song, R. P. Joshi, and S. J. Beebe, "Cellular Apoptosis by Nanosecond, High-Intensity Electric Pulses: Model Evaluation of the Pulsing Threshold and Extrinsic Pathway," *Bioelectrochemistry*, vol. 79, pp. 179-186, 2010.

R. P. Joshi, J. Song, K. H. Schoenbach and V. Sridhara, "Aspects of Lipid Membrane Bio-Responses to Subnanosecond, Ultrahigh Voltage Pulsing," *IEEE Transactions on Dielectrics and Electrical Insulation*, vol. 16, pp. 1243-1250, 2009.

R. P. Joshi, A. Mishra, J. Song, A. Pakhomov, and K. H. Schoenbach, "Simulation Studies of Ultra-Short, High-Intensity Electric Pulse Induced Action Potential Block in Whole-Animal Nerves," *IEEE Transactions Biomedical Engineering*, vol. 55, pp. 1391-1398, 2008.

R. P. Joshi, J. Song, A. Mishra, A. Pakhomov, and K.H. Schoenbach, "Simulation studies of high intensity, ultrashort electrical pulse effects on excitable cells," *30th International Meeting of the Bioelectromagnetics Society*, San Diego, CA, June 8-12, 2008.

R. P. Joshi, A. Mishra, J. Song, and K. H. Schoenbach, and A. Pakhomov, "Self-Consistent Analyses for Potential Conduction Block in Nerves by an Ultra-Short, High-Intensity Electric Pulse," *IEEE Int'l. Pulsed Power and Plasma Science Conf.*, Albuquerque, NM, June 17-22, 2007.

R. P. Joshi, J. Song, J. Kolb, K. H. Schoenbach, J. Gaudet, and C. Baum, "Evaluation of Optimal Sub-Nanosecond Excitation Waveforms in Generating Transmembrane Voltages in Cells for Bio-Effects," *IEEE Int'l. Pulsed Power and Plasma Science Conf.*, Albuquerque, NM, June 17-22, 2007.